Frontiers of Particle Beam and High Energy Density Plasma Science using Pulse Power Technology

Edited by Katsumi Masugata

November 20-21, 2009
National Institute for Fusion Science
Toki, Gifu, Japan

Abstract

The papers pr esented at the symposium on "F rontiers of Particle Beam and High Energy Density Plasma Scien ce using Pulse Pow er T echnology" held in November 20-21, 2009at National Institu te for Fusion Science ar e collect ed. The papers r eflect the pr esent status and resent progress in the experiment and theoretical works on high power particle beams and high energy density plasmas produced by pulsed power technology.

Keyword: high pow er particle beam, high energy density plasma, pulse d power technology, z-pinch, so ft x-ray , EUV , x-ray laser , pulse d discharge, high po wer micr owave, material processing, medial application

Preface

The symposium entitled "Frontiers of Particle Beam and High Energy Density Plasma Science using Pulse Power Technology" was organized as a collaborative research program of National Institute for Fusion Sciences (NIFS), and held November 20-21, 2009 at NIFS, Toki. During the 2 days of symposium, 22 papers were presented and totally 45 scientists attended. The proceedings retain most of the presentations and well reflecting the present status of the research field in high energy density plasma based on pulsed power technology in Japan.

As the field of high energy density plasma has a multidisciplinary nature, the extensive discussion of related subjects is difficult in conventional scientific meetings. The purpose of the symposium has been to provide a forum to discuss important technical developments, some important applications, increased understandings, new trends and also the future prospects in the field of high energy density plasmas and pulsed power technologies. The series of the symposium have been continued for 30 years successively, and contributed to the development of high energy density plasma research in Japan.

We would like to express our sincere thanks to all of the authors, participants, and the staffs of NIFS.

Katsumi Masugata
Department of Electrical and Electronic Engineering
University of Toyama

List of Participants

R. Ando	Kanazawa University
Y. Arai	Gunma University
k. Fujikawa	University of Toyama
K. Hayashi	Tokyo Institute of Technology
K. Horioka	Tokyo Institute of Technology
T. Hoshiba	Kanazawa University
T. Hosoi	Tokyo Institute of Technology
H. Hotta	Tokyo Institute of Technology
T. Ihara	Saga University
T. Imada	Niigata Institute of Technology
Y. Ishizuka	Tokyo Institute of Technology
H. Ito	University of Toyama
k. Iwasaki	Tokyo Institute of Technology
K. Kamada	Kanazawa University
M. Kanemaru	Tokyo Institute of Technology
A. Kikuchi	Tokyo Institute of Technology
F. Kondo	Kanazawa University
H. Kondou	Niigata Institute of Technology
A. Maeda	Nihon University
K. Masugata	University of Toyama
K. Misawa	Kanazawa University
Y. Nishino	University of Toyama
M. Nishio	Nihon University
K. Nose	Kanazawa University
D. Nunoya	Tokyo Institute of Technology
Y. Ochiai	University of Toyama
M. Onda	Niigata Institute of Technology
T. Ooshima	Nihon University
T. Ozaki	National Institute for Fusion Science
T. Saito	Tokyo Institute of Technology
H. Sakuma	Nihon University
T. Sasaki	Nagaoka University of Technology
K. Sato	Niigata Institute of Technology
Y. Soga	Kanazawa University

T. Tazima	National Institute for Fusion Science
K. Takaki	Iwate University
K. Takasygi	Nihon University
Y. Takimoto	Tokyo Institute of Technology
A. Tokuchi	Pulsed Power Japan Laboratory Ltd.
Z.P. Wang	University of Toyama
T. Yamabe	Saga University
S. Yanagi	Kanazawa University
T. Yoshinaga	Nihon University
H.R.Yousefi	University of Toyama
N. Yugami	Utsunomiya University

Contents

Study on a Gas Jet Type Z-pinch EUV Light Source

Yasuhiro Takimoto*, Huang Bin, Osamu Sakuchi, Masato Watanabe, and Eiki Hotta

Department of Energy Sciences, Tokyo Institute of Technology
4259, Nagatsuta, Midori-ku, Yokohama 226-8502, Japan
*takimoto.y.aa@m.titech.ac.jp

ABSTRACT

A compact and low-debris xenon (Xe) Z-Pinch discharge system was designed and assembled as an EUV (Extreme Ultraviolet) light source, in which a gas jet-type electrode was employed. The discharge head has a coaxial double nozzle. Pinched plasma column that emits EUV light is produced between the electrodes. The especially designed double nozzle electrode ejects helium (He) gas curtain through the outer nozzle to mitigate debris and confine the inner gas. In order to get higher EUV output, a pulsed power supply system has been developed in which a radio-frequency pre-ionization system was used. In the present study, the influence of high RF pre-ionization on EUV emission will be discussed. EUV pinhole images taken by an x-ray CCD camera indicate that EUV is emitted from pinched plasma near the cathode. The time-resolved EUV emission was acquired by using an EUV photodiode, and we observed that the time of EUV signal peak is temporally delayed with increasing Xe plenum pressure.

1. Introduction

EUV lithography is the most promising lithography technology for technical node of 32 nm or below. There are many issues for realizing its commercial application for EUV lithography, such as development of optical components and radiation sources [1]. One of the most important challenges is to develop an EUV light source. Two main types of EUV light sources, namely laser produced plasmas (LPP) and discharge produced plasmas (DPP), are under investigation all over the world. Compared with LPP, DPP methods generally have advantages of low costs, compactness, and high electrical conversion efficiency. However, it also has some problems such as low collection angle and superfluous debris generated from the electrode materials. Since the DPP source generally emits the light in a cone restricted by the electrode shape, the collection angle is typically smaller than 2π sr. In contrast, in the case of LPP EUV sources, the

collection angle is equal to 4π sr [2]. The larger collection angle means that higher EUV power can be obtained at the intermediate focus. Thus, further enlarging the collection angle of the DPP source is needed to satisfy the demands of high EUV power. Besides, considering the etendue requirement (< 3.3 mm^2sr), the light source of a smaller size is recommended. Another problem of the DPP light source is abundance of debris generated from electrodes and target. To realize the aim of large collection angle and debris mitigation for EUV simultaneously, we developed a gas jet type Z-pinch EUV light source.

2. Gas jet-type Z-pinch DPP

The gas jet Z-pinch source emits EUV light in the radial direction normal to the pinch axis, and thus it has a larger collection angle than the conventional DPP sources. The structure of the gas jet type Z-pinch electrode for generating EUV radiation is illustrated in Figure 1. It is composed of a coaxial double cathode nozzles and an anode plate which are both made of stainless steel. The inner nozzle with a 2 mm orifice is used to eject the Xe gas jet. An annular inward opening, which is 0.2 mm in width, is used as an outer nozzle for forming a He gas curtain. The debris of DPP sources generally emerges out in a cone along axial direction and, therefore, the radial extraction of EUV emission would lead to less debris and in addition a He gas curtain also sweeps the debris forward, in result of further debris reduction.

Figure 2 shows the power supply system which contains an LC inversion generator and two magnetic pulse compression stages to achieve higher discharge current. This system delivers a current with amplitude of up to 22 kA, rise time of 110 ns and the full width at half maximum (FWHM) of 260 ns to a short-circuit load. Xe preionized plasma is generated by using an RF inductively coupled plasma system. The preionized plasma is fed into the discharge head. The power of RF pre-ionization power supply is variable from 0 to 80 W independently of main discharge. When a pulsed high current is delivered from a pulsed power supply to the RF preionized plasma jet, the Lorentz force stemming from the cross product of high current and its corresponding magnetic field compresses the cold Xe plasma to a hot high-density pinched plasma. This high temperature plasma radiates EUV light around 13.5 nm [3].

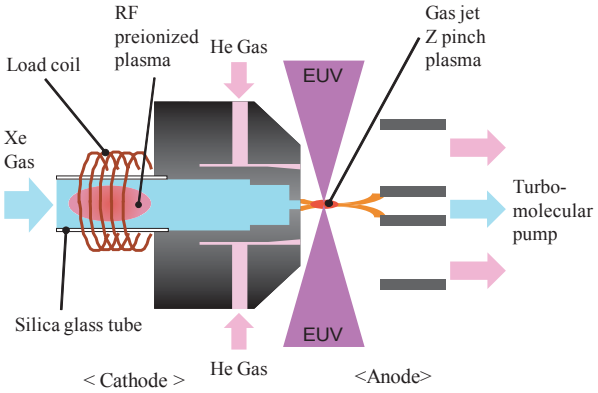

Fig.1. Schematic of the gas jet type Z-pinch source.

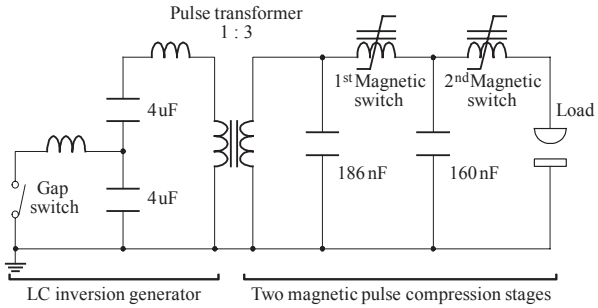

Fig.2. Pulsed power supply system.

3. Results and Discussion

3-1. Temporal distribution of EUV emission

To observe the temporal distribution of EUV emission, the EUV plasma images were recorded by

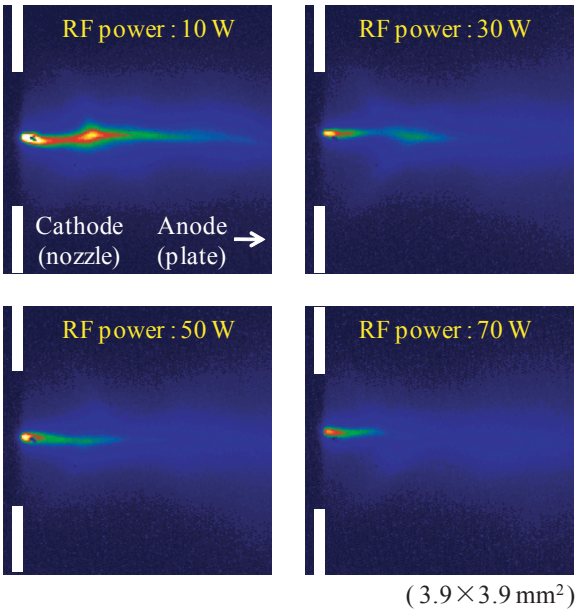

Fig.3. EUV pinhole images at each RF power.

using a pinhole camera for various RF input power (10-70 W). The EUV pinhole camera consists of a 50 μm pinhole, a Zr filter and an X-ray CCD camera (Andor Technology Ltd. DO434). EUV pinhole images were recorded perpendicularly with respect to the electrode axis. These measurements were conducted without a He gas curtain. Figure 3 shows the EUV plasma images recorded at different RF input power for 10 mm electrode separation and Xe gas pressures 24 torr.

It is found that the position of EUV emitting zone was quite close to the cathode and its area decreased with increasing RF input power. In addition, on the image taken at RF power of 10 W, two EUV emission areas were observed on the axis with low pre-ionization degree. In general, pre-ionization is helpful to make an axisymmetric stable Z-pinch. Therefore, we speculate that EUV emission area far from the cathode is caused by a hot spot generated by sausage instability for low pre-ionization degree. We need further experiments to understand the process of plasma formation by observing time-resolved plasma images in detail.

Figure 4 shows the EUV intensity versus RF input powers (0-80 W) with and without a gas curtain. It is shown that the output signal taken with a He gas curtain is slightly stronger than that without a He gas curtain. However, we have to consider a higher EUV absorption with increasing whole gas pressure in the chamber. As indicated in ref.3, the EUV output signal measured with a He gas curtain is larger than that without a He gas curtain. The He gas curtain has an additional function of suppressing the expansion of Xe gas [4,5], and EUV intensity generated from Xe-He mixtures is higher than that from pure Xe [6].

From this figure, it is shown that EUV intensity slightly decreases or remains when RF input power is increased. The same relationship holds for the condition with a He gas curtain. In term of EUV output, it indicates that RF preionized plasma has few effect on main discharge plasma. One of the possible reasons is that the leakage current (~1 kA) which is generated from the 2nd magnetic switch before main discharge current pulse rises has stronger influence on pre-ionizaion than the RF plasma jet. In conventional system [7,8], we had to make pre-ionization plasma to make a breakdown. However, this pulsed power supply system does not need pre-ionization process to make EUV light source. If we have a different view, whole equipment can be more simplified.

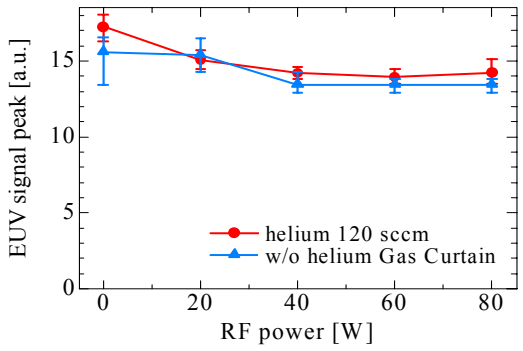

Fig.4. Dependence of EUV signal peak on RF power.

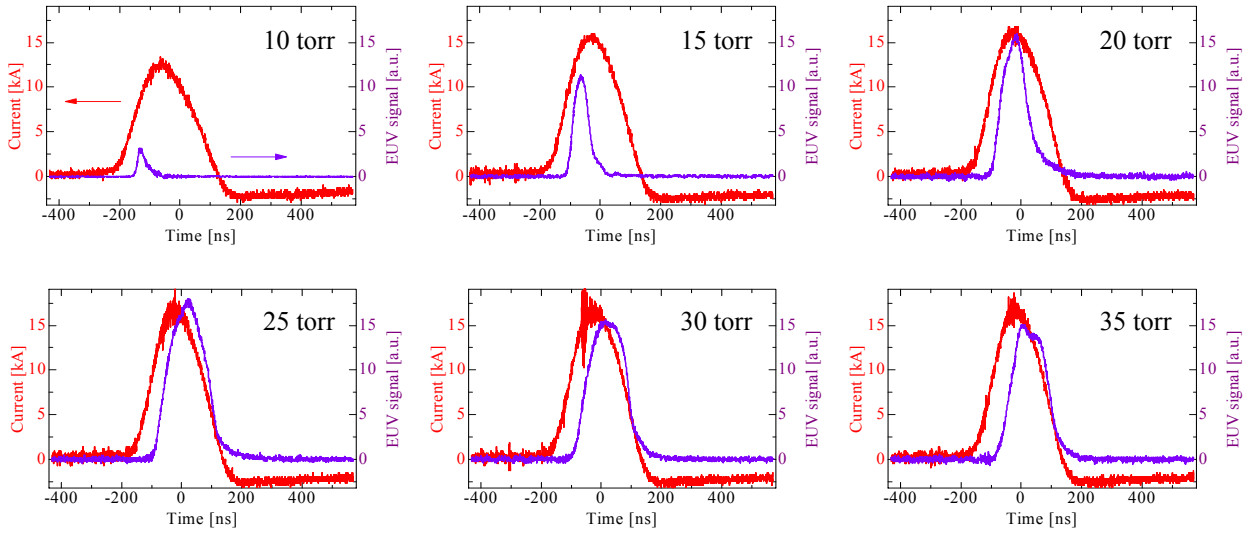

Fig.5. EUV photodiode signals at each Xe plenum pressure without RF pre-ionization

3-2. Time-resolved EUV emission at each Xe plenum pressure

In order to measure the time evolution of EUV output, an EUV photodiode (IRD,AXUV20HS1-Si/Zr, 11-18 nm) with a 200 μm pinhole was employed. Figure 5 shows the time evolution of photodiode signals together with the discharge current pulse at 20 mm of gap length, 10-35 torr of Xe pressure without RF pre-ionization. In these figures, it is confirmed that the time of the EUV signal peak shifts with increasing Xe pressure. At 25 torr, the EUV signal reaches a maximum value just after the peak of the current pulse and FWHM of EUV signal is found to be ~150 ns. Figure 6 shows time integrated values and FWHM of EUV signals. It is found that the time integrated value of EUV signal and FWHM of EUV emission increase with increasing Xe pressure below 25 torr. It is also found that the time-integrated and FWHM of EUV emission are almost constant over 25 torr of Xe pressure. In general, Xe initial gas density plays an important role in determining conducting path for the implosion trajectory. Differences in the pinch dynamics may influence these variations concerning EUV emissions.

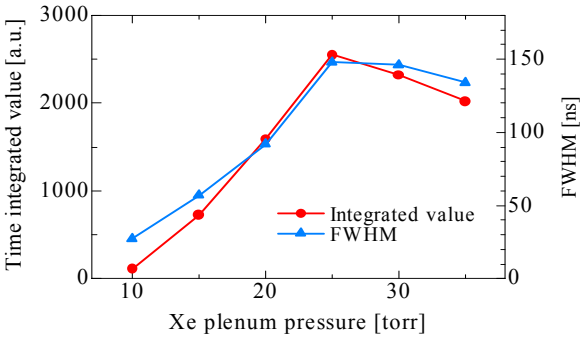

Fig.6. Time integrated values and FWHM of EUV signals.

4. Conclusion

In this paper, we describe the characteristics of gas jet type EUV source.

EUV emission region was observed near the cathode nozzle from photographs taken by an x-ray CCD camera. By increasing RF input power, EUV light source becomes small in size, and RF preionized plasma does not contribute to enhancement of EUV output. The RF pre-ionization system was expected to help enhancement of the yield of the soft x-ray emission, however it contributes not at all here. As a possible cause, the leakage current from the magnetic switch influences more strongly on pre-ionization of plasma jet than RF pre-ionizaiton.

On the time-resolved EUV emission waveform, the time of EUV signal peak delays with increasing Xe plenum pressure. These results suggest that initial distribution of Xe gas density changes the generation process of Z-pinch plasma.

To investigate the pinch process in detail, Nomarski interferometer will be used to measure the electron density profile. We also intend to measure current density distribution to check whether there is localized irregular discharge by using a magnetic probe.

References

[1] V. Banine and R. Moors, Extreme ultraviolet sources for lithography applications, Proc. of SPIE, Vol. 4343 (2001) 203.

[2] R. Lebert, K. Bergmann, L. Juschkin, O. Rosier, W. Neff, Comparison of Different Source Concepts for EUVL, Proc. of SPIE, Vol. 4343 (2001) 215.

[3] M. A. Klosner and W. T. Silfvast, Intense xenon capillary discharge extreme-ultraviolet source in the 10–16-nm-wavelength region, Optics Letters, Vol. 23, No. 20 (1998) 1609.

[4] M. Watanabe, N. Kishi, N. Iizuka, T. Orishimo, J. Fei, A. Okino and E. Hotta, Optical observation of gas jet Z-pinch discharge produced extreme ultra violet light source, 16th IEEE International Pulsed Power Conference, Vol. 2 (2007) 1679.

[5] R. Bruijn and K. Koshelev, Absorption of EUV in laser plasmas generated on xenon gas jets, Journal of Quantitative Spectroscopy and Radiative Transfer, Vol. 81 (2003) 97.

[6] M. McGeoch, Radio-frequency-preionized xenon z-pinch source for extreme ultraviolet lithography, Applied Optics, Vol. 37 (1998) 1651.

[7] I.H. Song, K. Iwata, Y. Honma, S.R. Mohanty, M. Watanabe, T. Kawamura, A. Okino, K. Horioka and E. Hotta, Characteristics of Xenon Capillary Z-pinch Extreme Ultraviolet Lithography Source Driven by Different *dI*/*dt* Discharge Current Pulses, Jpn. J. Appl. Phys., Vol. 44, No. 12 (2005), 8640.

[8] I.H. Song, Y. Honma, K. Iwata, S.R. Mohanty, M. Watanabe, T. Kawamura, A. Okino, K. Yasuoka, K. Horioka and E. Hotta, Development of gas jet type Z-pinch extreme ultraviolet light source for next generation lithograph, NIFS-Proc, 61 (2005) 23.

HIGH AVERAGE-POWER LIGHT SOURCES FOR ADVANCED LITHOGRAPHY

T. Saito and K. Horioka

Department of Energy Sciences, Tokyo Institute of Technology, Nagatsuta 4259, Yokohama 226-8502, Japan

ABSTRACT

This paper describes expected high average-power light sources for the next generation lithography. The light sources need high repetition capability, narrow spectrum out-put and long life. We discuss the possibility of operation of ArF excimer lasers at repetition of more than 6 kHz, based on experimental results and numerical simulations.

1. Introduction

Technology based on ArF excimer laser (λ = 193 nm) lithography, has been introduced to the volume production from HP (Half-Pitch)-90nm node in semi-conductor manufacturing[1]. Currently, its node is moving to HP-45nm with ArF immersion technology, as shown in Table 1. Performance specifications of current ArF excimer laser for lithography are average power of 60 W, repetition rate of 6 kHz and spectral bandwidth (E95) of 0.35 pm[2]. And 90W-6kHz ArF excimer laser is now releasing to the volume production for higher throughput. On the other hand, the important candidate for the next generation technology is EUV lithography, which uses 13.5 nm spectrum output from a plasma light source. Its development is progressing actively for the introduction to volume production at around 2013[3]. However, technical barriers such as the throughput, cost and lifetime of the EUV source and its optics are still high. So, the double patterning technology is developing for the life extension of ArF lithography[4].

The most important issue of double patterning technology is overlay accuracy. The double patterning technology produces one pattern by double exposure. So, the overlay accuracy becomes more important factor, compared with normal exposure method. Moreover, higher power (>90W) and higher repetition rate (>6kHz) are needed for compensating the throughput decrease due to the process number increase.

In this paper, we describe the technologies of high average-power light source for the advanced lithography. Technological issues are highly repetitive operation, narrow band output and long life of the light source. Also, we describe the effects of discharge induced gas density disturbance on the highly repetitive operation over 6 kHz, based on a comparison between experimental results and numerical simulations. We discuss the possibility of highly repetitive operation of ArF laser over 6 kHz.

Table 1 Lithography Roadmap

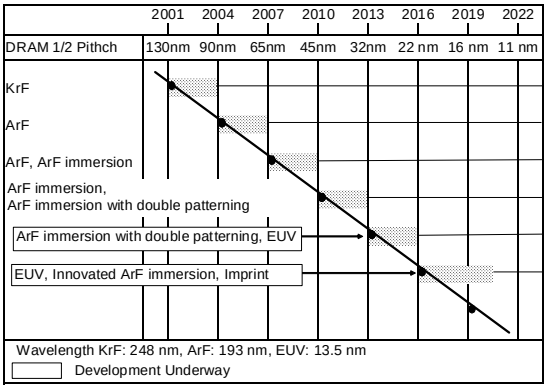

2. Light source for lithography

Figure 1 shows a schematic of the ArF excimer laser. It consists of several main modules; a discharge chamber, a pulse power module, a line narrowing module and a monitor module. The discharge chamber is a key module for the high-average power excimer light. The pulse power module supplies the electrical power of a few J with a few 10ns to electrodes inside the discharge chamber. The line narrowing module is for narrowing the spectrum. Although, excimer laser spectrum bandwidth is basically a few 100 pm, the line narrowing module narrows the spectrum to sub pm. The monitor module is for measuring the energy and wavelength. These data were fed back to controller for controlling the energy and wavelength by pulse to pulse. Table 2 shows the summary of current source requirements for the latest ArF lithography.

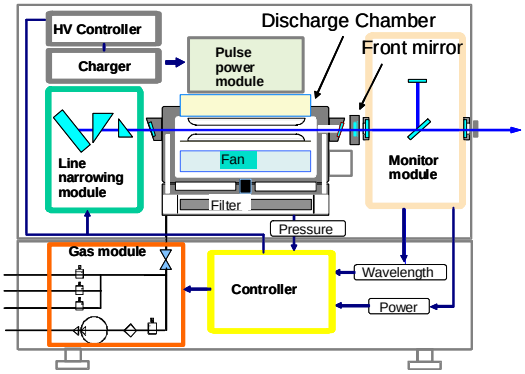

Fig. 1 ArF excimer laser for lithography

Table 2 Light source requirements

Lithograpy requirement	Light source requirement	
High throughput	High power	>= 60W - 90W
	High repetition rate	>= 6 kHz
High resolusion	High energy stability	<= +/- 0.3 %
	Narrow spectrum (E95)	<= 0.35 pm
	High wavelength stability	<= +/- 0.012 pm
Low operation cost	Long lifetime (Chamber)	>= 20 Bpls
	High reliability (Availability)	>=99.5%

2. 1 High repetition technology

Highly repetitive operation is important for high throughput and high resolution in lithography. The key module for high repetition capability is the discharge chamber. One of main issues in high repetitive operation is to suppress the gas density fluctuation induced by acoustic waves[1)]. Acoustic waves generated by the discharge spread to various directions. Then they are reflected back from various structures inside the laser chamber. They induce the fluctuation of gas density and discharge instability at a specific frequency range of over 2 kHz. This degrades the laser performance, such as spectrum, wavelength and energy stability. We developed and applied the acoustic wave damper to reduce the reflection of acoustic waves. Figure 2 shows images of the wave pattern in laser chamber without and with acoustic damper. In the chamber with acoustic wave damper, the acoustic waves were weakened by the damper and gas density fluctuation in discharge area could be reduced. Figure 3 shows the discharge area inside laser chamber without and with acoustic wave damper measured by Schlieren method. As shown, the density fluctuation in discharge region was clearly improved by the acoustic wave damper.

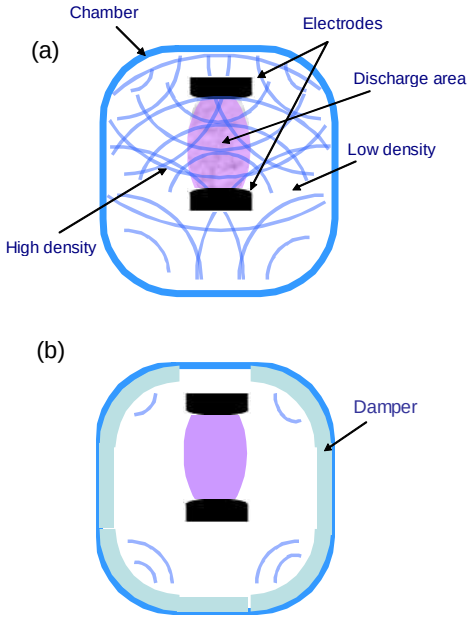

Fig. 2 Images of laser chamber without (a) and with (b) acoustic wave damper

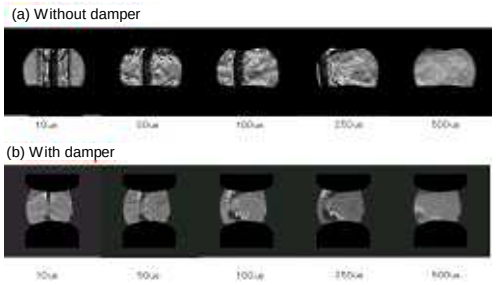

Fig. 3 Gas density fluctuation in discharge area without (a) and with (b) acoustic wave damper

2. 2 Narrow band technology

Spectral performance is a key performance for achieving high resolution under highly repetitive operation. It is well known that spectral performance is defined by the following two indices in lithography: 1) the full width at half maximum (FWHM), 2) the full width in which 95 % of the laser energy is contained (E95) in laser spectra. Currently, spectral E95 is used as a representative index of the spectral performance because of its sensitivity to lithography[5)]. The spectrum performance is maintained by the line narrowing module. The optics of line narrowing module consists of a diffraction grating and prisms and its performance is basically determined by the wavelength dispersion.

Figure 4 shows the typical spectral profile in ArF excimer laser for lithography[1)]. It showed the good spectral performance is maintained by using the high dispersion optics.

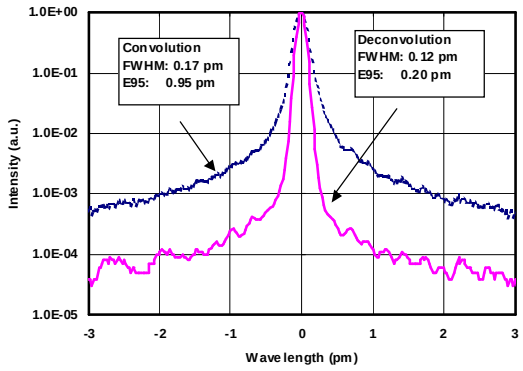

Fig. 4 Typical spectral profile in ArF excimer laser for lithography

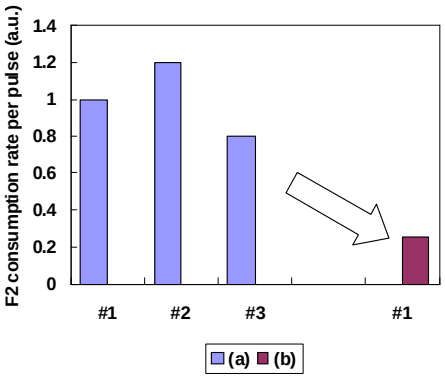

Fig. 5 F2 consumption rate: (a) electrode without film, (b) electrode with film

2. 3 Long life technology

Long life technology is very important for lowering the operation cost in the volume production. For the cost lowering, key modules are the discharge chamber and the line narrowing module because they are costly components in all modules.

The lifetime of discharge chamber is mainly limited by the electrode erosion. So, we developed new electrode structure protected by surface covering films. Figure 5 shows the F2 (Fluorine molecule) consumption rate for electrodes without and with the protected films. As the F2 consumption rate is almost proportional to electrode erosion, we could improve the F2 consumption rate to one fifth by using the newly developed electrodes.

The lifetime of line narrowing module is limited by the optics performance, such as degradation of transmittance and diffraction efficiency. Figure 6 shows the deterioration of optics performance. As shown, we improved the optics deterioration to one fifth by using newly developed optics.

Table 3 shows the lifetime specifications of main modules in laser types developed by Gigaphoton Inc., for the ArF lithography[1)2)]. Current model has two chambers, which is an injection locked type for narrow spectrum and high average power output. Module lifetime is now improving by the new technologies, year by year. At the moment, lifetimes of the modules in all of current models are over 20 billion pulse [2)]. For higher average power device and also for the next generation lithography, possibility of operation more than 6kHz level is eagerly considered.

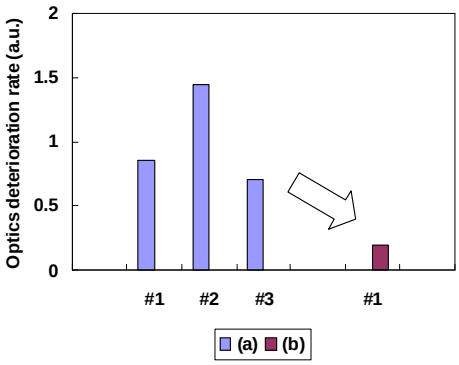

Fig. 6 Optics deterioration rate: (a) conventional optics, (b) new optics

Table 3 Lifetime and specifications of ArF excimer laser for lithography

Type	G41A	G42A	GT40A	GT60A	GT61A	GT62A
Release (year)	2001	2003	2005	2006	2008	2010
Power (W)	20	20	40	60	60	90
Repetition rate (kHz)	4	4	4	6	6	6
Spectral E95 (pm)	1	0.75	0.5	0.5	0.35	0.35
Chamber (Oscillator, Bpls)	5	8	20	20	20	20
Chamber (Amplifier, Bpls)	-	-	30	30	30	30
Line narrowing module (Bpls	6	8	40	40	40	40
Monitor module (Bpls)	7	10	30	30	30	30

Bpls: billion pulse

3. Next generation light sources

Highly repetitive operation is a key performance for the next-generation ArF excimer laser for lithography. For achieving highly repetitive operation, it is very important to suppress the discharge induced disturbance by acoustic waves. As previously described, acoustic wave damper inside the laser

chamber is a general countermeasure to suppress the disturbance. Recently, an effective countermeasure becomes possible based on acoustic wave simulations[6)-8)]. However, an overlay effect of acoustic waves reflecting from various components inside the laser chamber is considered to increase with increasing repetition rate. So, we need to investigate the overlay effects of acoustic waves. In this section, we describe the possibilities of highly repetitive operation of over 6 kHz, based on the experimental and numerical simulations.

3.1 Experimental setup

Figure 7 shows a schematic view of a proto-type discharge chamber, which is used in the experiment of over 6 kHz operations. This chamber was manufactured, based on the chamber used in 6 kHz ArF excimer laser for lithography[2)]. Its scale is 400 mm (Length) x 220 mm (Height). Gas velocity between electrodes is one of main issues to achieve highly repetitive operation. In this chamber, electrodes gap was reduced to 50% of 6kHz ArF excimer laser chamber for increasing the effective gas velocity between electrodes.

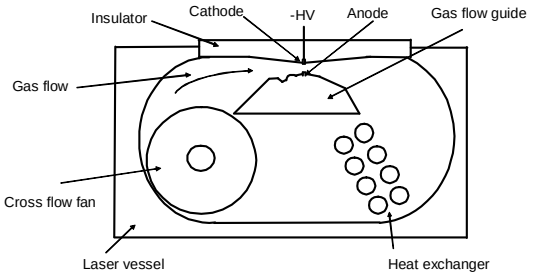

Fig. 7 Cross sectional view of discharge chamber

3.2 Acoustic wave simulation.

Equation (1) is the basic equation for analyzing the acoustic wave propagation in Cartesian coordinate (x,y,z), which is derived from the continuity eq. (2) and the Euler's eq. (3), as follows;

$$\frac{\partial^2 P}{\partial x^2}+\frac{\partial^2 P}{\partial y^2}+\frac{\partial^2 P}{\partial z^2}-\frac{1}{c^2}\ddot{P}=0 \qquad (1)$$

$$-\frac{1}{k}\frac{dP}{dt}=div\left(\frac{d\vec{U}}{dt}\right) \qquad (2)$$

$$\nabla P=-\rho\ddot{\vec{U}} \qquad (3)$$

where P and c are the pressure and the wave velocity in medium. Here, c is approximated to be the sound velocity. U is the particle displacement, ρ is the gas density, and k is the bulk modules (=ρc^2).

The gas composition for the experiment is Ar/F2/Ne=3.5/0.1/96.4 % with total gas pressure of 300 kPa. The average gas temperature is assumed to be 320 K and the value of c is calculated to be 464 m/s.

The temporal and spatial resolutions in this simulation are 125 ns and 0.6 mm, respectively. The simulation region contains all of the chamber components inside the chamber as shown in Fig. 6, for taking account of the effects of acoustic waves reflecting from the various portion of chamber. Also, we executed the simulation during 10 ms for investigating the overlap effect of acoustic waves.

It is well known that the pattern of acoustic wave can be classified into two types. One is the wave propagating perpendicular to the electrodes gap. Another is a propagating wave between the electrodes.

Figure 8 shows the arrangement of sound sources used in this simulation. The sound sources are arranged near the electrode surface (Fig. 7, Sound source 2) in addition to the sources arranged in the center of discharge area. This is for generation of the propagating wave between the electrodes. The initial condition of sound source was taken to be one period (1 μs) of a triangular wave. Figure 9 shows the evolution of acoustic waves in the discharge area. After 5 μs, propagating waves between electrodes are generated, and waves perpendicular to the electrodes gap propagate. Small pressure waves overlapped each other and the gas density fluctuation is reflected by the pressures under the acoustic wave approximation.

We defined the gas pressure (density) fluctuation (ΔP) with the following equation.

$$\Delta P=\left(\sum_{i=1}^{N}\left(P(p_i)-P_0\right)^2/N\right)^{1/2} \qquad (4)$$

Here, $P(p_i)$ is the pressure at p_i, p_i is a sampling point, and N is the total sampling point; 39.

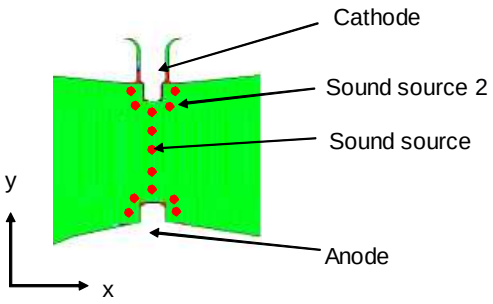

Fig. 8 Arrangement of acoustic sources for numerical simulation

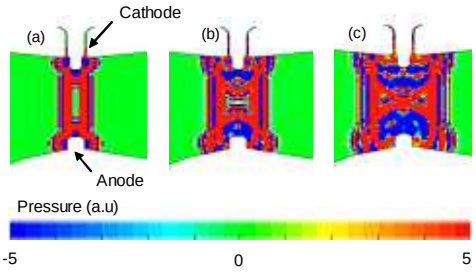

Fig. 9 Typical evolution of acoustic waves in discharge region

3.3 Spectrum performance and simulation results

Figure 10 shows the spectral performance (E95) obtained by using proto-type chamber. As shown in the figure, stable performance is obtained up to 10 kHz. However, spectral E95 degradation (E95 increase) at repetition rate around 7400 Hz and 8100 Hz appeared. This would be due to the acoustic wave effects.

Figure 11 shows the gas pressure fluctuation between electrodes by using the acoustic wave simulation. Figure 11 (a) is the simulation result by using 1 pulse sound source and (b) is the result by iterative sound source up to 10 ms. Clearly, the result in figure 11 (b) shows the good agreement with the experimental results shown in Fig. 10. The gas density fluctuation around 7400 Hz is the same in Fig 11 (a) and (b). This means that there is no overlay effect of acoustic waves in this frequency region. On the other hand, the gas density fluctuation around 8100 Hz indicates the overlay effect because the gas density fluctuation in Fig. 11 (b) is larger than that in Fig. 11 (a). However, the overlay effect is very limited and appears only in around 8100 Hz region. The following simulation was executed by using 1 pulse sound source, based on these results.

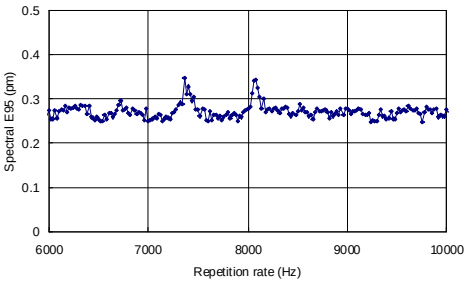

Fig. 10 Effect of repetition rate on spectrum performance E95

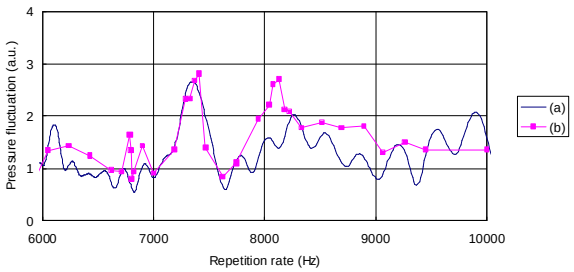

Fig. 11 Gas pressure fluctuation between electrodes by acoustic wave simulation: (a) single pulse, (b) iterative pulse up to 10 ms

3.4 Investigation of highly repetitive operation

Figure 12 shows the time dependency of gas pressure fluctuation from 8 kHz to 16 kHz in proto-type chamber (a) and the chamber without acoustic wave damper (b). In repetition rate lower than 10 kHz, the effect of acoustic wave damper is clear. On the other hand, this effect is decreasing relatively with increasing the repetition rate. This is because that the effects of acoustic wave propagating between the electrodes become dominant with increasing repetition rates.

Figure 13 shows the pressure distribution between electrodes versus repetition rate from 8 kHz to 16 kHz in current discharge chamber. Pressure peak movement between electrodes become clear with increasing the repetition rate.

The performance can be improved by adding the acoustic wave damper near the electrodes. However, adding the damper near the electrode is not realistic solution due to insulation issues. This indicates that we need redesign of structure around the electrodes for the suppression of acoustic waves traveling between them. Also, it would be effective to reduce the input energy between electrodes for suppression of acoustic waves.

In the discharge pumped excimer laser, a few J of energy is input in the discharge area between electrodes during a few 10 ns. This induces a rapid pressure increase between electrodes, and the mechanical vibration of electrodes. This would be a cause of acoustic wave traveling between the electrodes. This indicates that the suppression of this vibration would be an important point in highly repetitive operation of ArF laser over 10 kHz level.

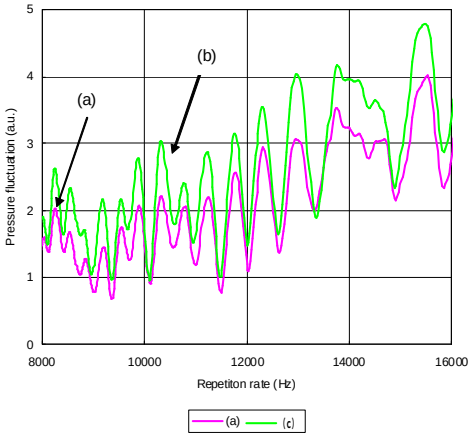

Fig. 12 Time dependency of gas pressure fluctuation in : (a) Current chamber, (b) Chamber without all acoustic wave damper

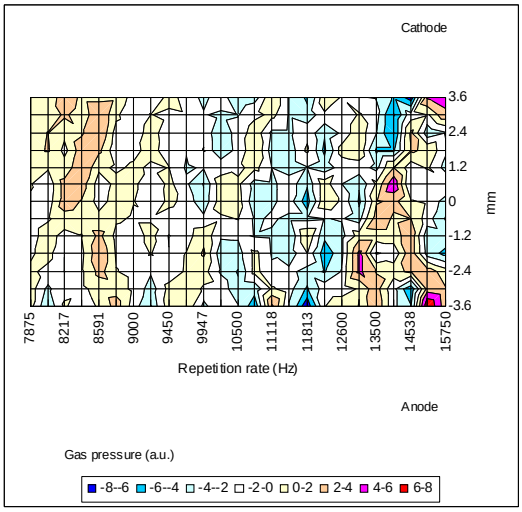

Fig. 13 Pressure distribution between electrodes versus repetition rate from 8 kHz to 16 kHz

4. Summary

We discussed technological issues for high average-power ArF laser light source for lithography. The issues are classified as follows;

- High repetition technology over 6kHz
- Narrow band technology
- Long life technology.

We also described the investigation results of highly repetitive operation of ArF laser over 6 kHz based on experimental results and numerical simulations. The results showed mitigation of gas density fluctuation induced by acoustic waves is critical issue for the highly repetitive operation. Results also indicated that redesign of structure around electrodes would extend the operation region of ArF laser more than 10kHz level.

References

1) T. Saito, T. Suzuki, M. Yoshino, O. Wakabaysshi, T. Matsunaga, J. Fujimoto, K. Kakizaki, T. Yamazaki, T. Inoue, K. Terashima, T. Enami, A. Sumitani, H. Tomaru and H. Mizuguchi: "Ultra line-narrowed ArF excimer laser G42A for sub-90-nm lithography", Proc. SPIE Vol. 5040, pp.1704-1711 (2003)
2) H. Tsushima, M. Yoshino, T. Ohta, T. Kumazaki, H. Watanabe, S. Matsumoto, H. Nakarai, H. Umeda, Y. Kawasuji, T. Suzuki, S. Tanaka, A. Kurosu, T. Matsunaga, J. Fujimoto and H. Mizoguchi: "Reliability report of high power injection lock laser light source for double exposure and double patterning ArF immersion lithography", Proc. SPIE Vol. 7274, pp.72743L-1-10 (2009)
3) H. Meiling, N. Buzing, K. Cummings, N. Harned, B. Hultermans, R. Jonge, B. Kessels, P. Kurz, S. Lok, M. Lowisch, J. Mallman, B. Pierson, C. Wagner, A. Dijk, E. Setten and J. Zimmerman: " EUVL System – Moving Towards Production ", Proc. SPIE Vol. 7271, pp. 727102-1-15 (2009)
4) M. Burkhardt, J. Arnord, Z. Baum, S. Burns, J. Chang, J. Chen, J. Cho, V. Dai, Y. Deng, S. Han. S. Holmes, D. Horak, S. Kanakasabapathy, R. Kim, A. Klatchko, C. Koay, A. Kransnoperova, Y. Ma. E. McLellan, K. Petrillo, S. Schmitz, C. Tabery, Y. Yin, L. Zhuang, Y. Zou, J. Kye, V. Parruchuri, S. Mansfold, S. Sperience and M. Colbum: " Overcoming the challenges of 22-nm node patterning through litho-design co-optimization", Proc. SPIE Vol. 7274, pp. 727404-1-8 (2009)
5) A. Ershor, T. Hofman, W. Partlo, I. Fomenkov, G. Everage, P. Das and D.Myers: " Feasibility Studies of Operating KrF lasers at Ultra-Narrow Spectral Bandwidth for 0.18 um Line Width, ", Proc. SPIE Vol. 3334, pp.1021-1029 (1998)
6) T. Hori, T. Yabu, T. Ishihara, T. Watanabe, O. Wakabayashi, A. Sumitani, K. Kakizaki and H. Mizoguchi: " Feasibility study of 6 kHz ArF excimer laser for 193 nm immersion lithograph", Proc. SPIE Vol. 5754, pp.1285-1292 (2005)
7) K. Kakizaki, Y. Sasaki and T. Inoue: "High-repetition-rate (6kHz) and long-pulse duration (50 ns) ArF excimer laser for sub-65 nm lithograpy", Rev. Sci. Instrument. Vol.77, pp1-6(2006)
8) K. Kakizaki, T. Yabe, T. Hori, H. Mizuguchi and Y. Sasaki: " Reduction of Acoustic Wave Induced by Discharge in High Repetition Rate ArF Excimer Laser Cavity to Obtain Narrow-Bandwidth Laser Light ", Jpn. J. Appl. Phys. Vol. 45, No. 10A, PP.7719-7723 (2006)

Plasma Dynamics Study on Counter-facing Plasma Focus System for Repetitive and Efficient EUV source

Daisuke Nunotani, Mitsuo Nakajima, and Kazuhiko Horioka*
Department of Energy Sciences, Interdisciplinary Graduate School of Science and Engineering, Tokyo Institute of Technology, 4259 Nagatsuta, Midori-ku, Yokohama 226-8502, Japan

A counter-facing plasma focus system, in which the source plasma is supplied by a surface discharge through thin metal layer, has been developed, for repetitive and efficient extreme-ultraviolet light source. The plasma source was formed along thin Sn layers on insulator surfaces of positive and negative electrodes. The Sn layer was prepared by evaporation in vacuum and behavior of the plasma gun was investigated as a function of the layer thickness and polarity of the electrodes.

Keywords: Plasma confinement, EUV light source, Plasma focus, High energy density plasma

I. INTRODUCTION

Despite recent efforts in developing a discharge produced EUV plasma source, an efficient and repetitive light source remains to be realized. Both high average power and high conversion efficiency together with repetition capability, are needed for the light source of EUV (Extreme Ultra-Violet) lithography.

Mo/Si multi-layered mirror has been developed to the lithography which has sensitivity in 13.5 nm± 1 %(in-band range). High energy density plasmas have been investigated for the bright and cost-effective in-band EUV source. However, conventional Z-pinch discharge scheme used for EUV source is basically one-dimensional. The plasma conversion efficiency of a conventional EUV source is dominated by by the transient nature of the one-dimensional scheme with a very short life time of radiating plasma.

Plasma conversion efficiency (P.C.E) can be represented as follows,

$$P.C.E = \frac{P_{out} \times S.E. \times \tau}{P_{in} \times T} \tag{1}$$

where, P_{in} is power input to the light source plasma, T is the time duration of input power, P_{out} is total radiation power, $S.E$ is spectral efficiency represented by $S.E = P_{inband}/P_{out}$, and τ is EUV emission duration. Input energy mostly runs away for heating and ionizing the plasma in early stage and the over-compressed high energy density plasma should expand or collapse immediately due to huge internal pressure and/or instability of fast pinching plasma.

Then the P.C.E of conventional EUV source is dominated by a very short lifetime τ. It was estimated that P.C.E approaches to S.E when τ come to several μsec [1, 2]. Therefore, prolonging the life time of radiating plasma with high S,E , i.e., increasing τ of Li or Sn plasma is considered to be the most feasible way to improve the P.C.E. As a long pulse high energy density plasma source, a counter-facing plasma focus system was proposed [3].

Spectral efficiency essentially depends on the plasma element and condition. Until recently, Xe, and Sn have been investigated because they have relatively a lot of spectrum lines in the in-band region. Hydrogen-like Li plasma has the highest S.E due to its spectral structure. The optimum electron density is estimated to be $n_e \sim 10^{18} cm^{-3}$ and electron temprature $T_e \sim 30$[eV] for Xe and Sn, $n_e \sim 10^{18} cm^{-3}$ and $T_e \sim 18$[eV] for Li. These parameters should be kept for the emission time. Therefore, light source plasma should have high energy density, high controllability and stability.

II. COUTER-FACING PLASMA GUNS

Z-pinch plasma has been used for Discharge Produced Plasma (DPP) light source, which is, as has been discussed, driven basically by an 1-dimensional compression scheme and can't confine the plasma for $\sim \mu$sec. Average velocity of EUV plasma particle is estimated to be order of $\sim$ 1 cm/μsec for axial direction. Therefore 2-

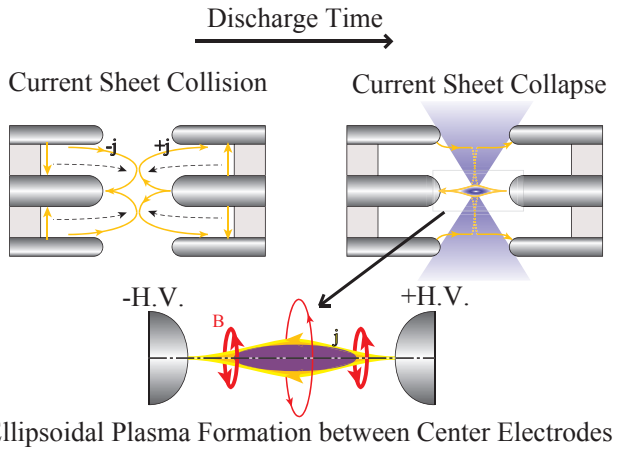

FIG. 1: A schematic diagram of high-energy-density plasma formation process in counter-facing focus electrode

*Electronic address: khorioka@es.titech.ac.jp

demensional (axial and radial) compression is required to prolong the life time of EUV plasma. We proposed a DPP source composed of counter-facing plasma guns for the plasma confinement and investigated the plasma dynamics in it. The outer electrodes are grounded and the center bar electrodes are applied high voltages with reversed polarity.

The concept of 2-dimensional plasma compression and confinement is shown in Fig.1. Current sheets are formed, initially, at the insulator surfaces and electromagnetically driven to the center of the electrodes. When we make a proper discharge condition, the current sheets are expected to collapse and shrink to the center of the electrodes. The ellipsoidal configuration is expected to be able to make a 2-demensionally confined plasma, i.e., radial component of the magnetic pressure compresses the plasma. The axial component confines and suppresses the particle loss to axial direction. The ellipsoidal plasma is considered to be intrinsically stable and robust against MHD(Magneto Hydro-Dynamics) instability.

III. EXPERIMENTAL SETUP

The experimental arrangement is shown in Fig.2. The circuit capacitance is 2 $\times$ 0.4 μF, charged voltages are nominally $\pm$ 15 kV, circuit inductance is estimated to be 0.4 μH. We have shown that high energy density plasma can be made and confined for several μsec by the 2-dimensional compression. The plasma gun consists of a pair of coaxial electrode, one of which is faced to the counter electrodes with 4mm gap. Then the focus system has a pair of ground electrodes with 10 mm inside diameter, and a pair of center-bar electrode 5mm in diameter. In the previous experiments, as a trigger assist, the insulator surfaces were coated with quasi-conductor layer consisted of carbon nano clusters and an insulating oil.

The current sheets are expected to connect after the collapse because the center electrodes have opposite polarities. After the connection, the current path forms a stable shape to compress and confine the plasma both in radial and axial directions. In order to realize this scheme, there are 4 important points; "Current sheet uniformity", "Discharge jitter", "Plasma dynamics in sheet collapse and connection", and "Current waveform formation appropriate to long time plasma confinement".

The proof-of-principle experiment was performed using Xe gas filled condition[3]. For highly repetitive operation and higher S.E, we have to manege the system with more practical operating condition, in which the source plasma should be continuously supplied from thin layer of Sn or Li metal.

Fig.3 shows the experimental set-up for the plasma formation experiment using thin metal plasma source. Current was monitored with Rogowski coils (model 110, PEASON ELECTRONICS) placed near the capacitance ground sides and voltage was measured with a High Voltage prove. A high speed framing camera (IMACON468, DRS HADLAND) was used to observe the plasma formation process. The framing camera was set on the right angle of electrode axis, through the observation window.

IV. RESULTS AND DISCUSSION

We formed thin Sn layer for the plasma source on the insulator surface between the focus electrodes. In order to make a well-defined condition, the Sn layer was formed by a vacuum evaporation method and the plasma formation process was investigated as a function of the layer thickness.

Fig.4 shows typical waveforms of voltage and current across the Sn layer. We investigated the behavior of the voltage and current as a function of polarity and thickness.

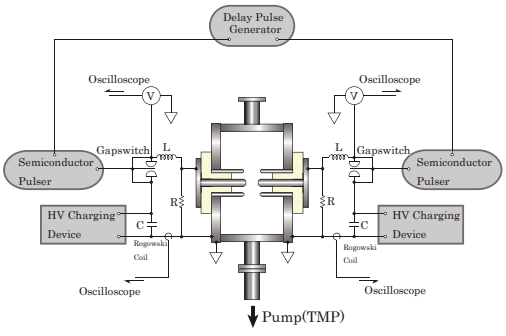

FIG. 2: Experimental arrangement of counter-facing plasma focus system

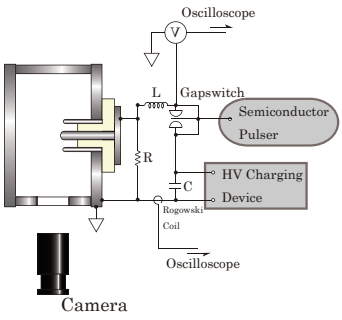

FIG. 3: Set-up for plasma formation experiment with thin metal plasma source

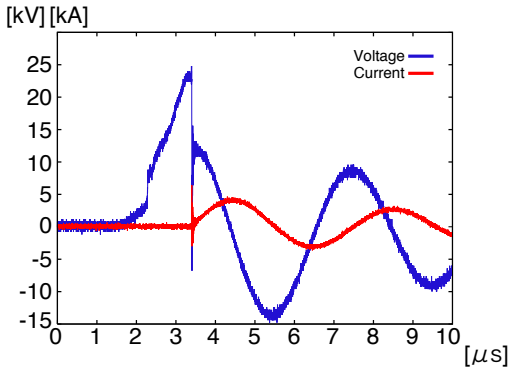

(a): Charge Voltage +15kV-10nmSn

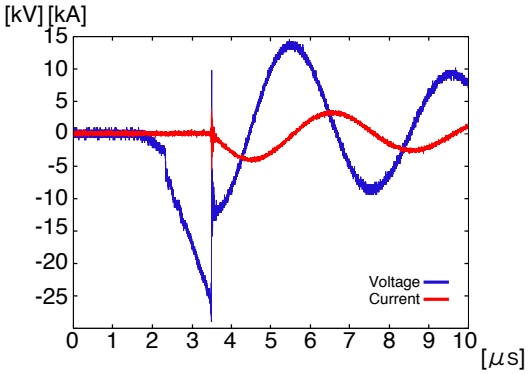

(b): Charge Voltage -15kV-10nmSn

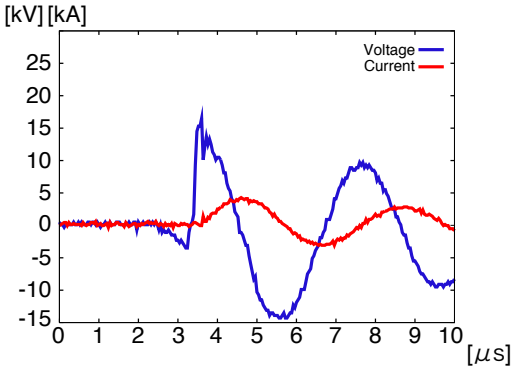

(c): Charge Voltage +15k-50nmSn

FIG. 4: Typical Waveforms of Voltage and Current, (a) +15kV-10nm-Sn, (b) -15kV-10nm-Sn, (c) +15kV-50nm-Sn

A. Current sheet uniformity and Discharge jitter

Framing images were taken from the axial and side direction of coaxial electrode. The results showed that the plasma formation process strongly depends on thin film condition.

In the previous configuration, we need a trigger assist to decrease jitter of the negative and positive discharges. In case of surface discharge mode, the breakdown time has jitters of several hundreds nsec range without trigger assist.

On the other-hand, with pre-conductor coating, the operation jitter of electrodes reduced less than 10 percent (∼25nsec) of no trigger assist. When we consider the sheet drift speed and electrodes gap-width, the jitter should be less than 50 nsec. This means that the Sn-layer works not only the plasma source but as the trigger assist for the plasma formation. As shown in Fig.4, when we form a thin metal layer along the insulator surface, we can avoid the jitter problem. By providing liquid Li/Sn through a porous ceramics, we can make a Li/Sn plasma, which is expected to fulfill both high spectral efficiency and low trigger jitter.

B. Plasma dynamics in the plasma gun

Plasma dynamics had 2 patterns; collapse mode and connection mode. The collapse phase emits EUV strongly because the drifting plasma is thermalized by the stagnation in the gap center. On the other hand, the plasma is compressed by connecting current in the connection mode. We could make clear that the formation processes of the connection and collapse modes are effected by electrical conductivity of the current path between facing electrodes.

This result indicates ellipsoidal current distribution compress the plasma to EUV condition and confine it stably for several μsec. The compressed plasma condition varies with initial condition, sometimes, the EUV emission repetitively occurs every confinement processes.

The plasma lifetime is expected to be prolonged by driving it with longer current waveform.

This result confirms the formation of plasma with stably confinement mode. This result shows that, in the connection mode, counter-facing plasma guns are able to compress and confine the EUV plasma stably for several μsec duration.

The plasma kinetic energy is thermalized by the collision of current sheets. If the plasma stagnate completely, the plasma speed is corresponding to several 10 eV. After the first pulse, EUV emission was detected for several half of wavelength because plasma was preheated by the previous current sheet, which improve conductivity between electrodes and current path is connected at the electrodes[4].

V. CONCLUDING REMARKS

We have investigated plasma dynamics in a counter-facing plasma focus system, in which the source plasma was supplied from thin metal layer on the insulator surface. Results indicated the behavior of current sheet was qualitatively similar to the gas filled plasma focus system. Namely, current sheets driven by magnetic pressure, accumulate and focus the plasma to the center of counter-facing electrodes, which enables us to form ellipsoidal plasma in the counter-facing system. The ellip-

soidal plasma is considered to be robust against hydrodynamic instability of magnetically confined high energy density plasma. Results also showed that the plasma formation process depended on the thickness of metal layer, which indicates the plasma formation process can be optimized by the control of the surface condition.

These results mean that with proper current waveform and conditioning of the metal layer, this configuration of plasma gun is expected to prolong the EUV plasma lifetime to more than μsec and have a potential for high power, high efficiency, and repetitive EUV source.

Acknowledgments

The authors would like to express their thanks to H.Kuwabara for useful discussion and comments on the plasma dynamics. This work was partly supported by Ministry of Education, Culture, Sports, Science and Technology.

[1] Majid Masnavi, Mitsuo Nakajima, Eiki Hotta, and Kazuhiko Horioka, "Estimation of optimum density and temperature for maximum efficiency of tin ions in Z discharge extreme ultraviolet sources" J. Appl. Phys. 101, 033306 (2007)

[2] Majid Masnavi, Mitsuo Nakajima, Eiki Hotta, and Kazuhiko Horioka, "Estimation of the Lyman-α line intensity in a lithium-based discharged plasma source" J. Appl. Phys. 103, 013303 (2008)

[3] Y.Aoyama, M.Nakajima, K.Horioka, "Counter-facing focus system as a repetitive and/or long-pulse high energy density plasma source", Physics of Plasmas, Vol. 16, 110701 (2009)

[4] Y.Aoyama, M.Nakajima, K.Horioka, "Counter-facing focus system as a repetitive and/or long-pulse high energy density plasma source", NIFS-PROC, Vol.82, 67 (2010)

PRODUCTION AND DISPERSAL OF TIN FINE PARTICLES IN A GAS-PUFF Z-PINCH EXPERIMENT

Akiko Maeda, Mineyuki Nishio and Keiichi Takasugi[+]

College of Science and Technology, Nihon University, Tokyo 101-8308, Japan

[+]*Institute of Quantum Science, Nihon University, Tokyo 101-8308, Japan*

He and Ar discharges have been done in the gas-puff z-pinch with tin (Sn) electrode. The difference of the formation of the dispersion material between two kinds of gases was examined. In both cases, fine particles of Sn were formed. The dispersing particles have melted in the He discharge, and they have solidified in the Ar discharge.

1 Introduction

Because of the good efficiency of energy transfer to the z pinch[1], it can easily generate high density and high temperature plasma. It is used as a strong pulsed light source in wide wavelength regions including extreme ultraviolet (EUV) light. As z pinch is an electrical discharge with electrodes, the plasma may touch the solid on the discharge, then a part of the electrode and the device material disperses and adheres to the window of the optical system or the diagnostic instrument. Such a dispersion material is called a debris.

In the EUV lithography, an efficient light source at the wavelength 13.5 nm is required. Although Sn is one candidate of the light source, it is easy to disperse and adhere to surroundings because the melting point is low, while it is solid at the normal temperature. Especially, there is a possibility of a large amount of Sn dispersion when the discharge is done with a Sn electrode. The control and suppression of the dispersion material is one of the big problems in the development of EUV light source, however, the mechanism of formation and the dispersion process of the material are not well understood. Then, we paid attention to the dispersion material originated from the electrode, and the material was observed by using the Sn electrode used for the development of EUV light source.

It is understood from the former researches that the material is not dispersed from the surface of the electrode directory but from the entire interelectrode, and that the dispersion is not homogeneous azimuthally[2]. The material is in the form of melting fine particles. So it is thought that they are charged by the contact with the plasma, move with the plasma due to the electromagnetic force, and then disperse to surroundings at the collapse of the plasma.

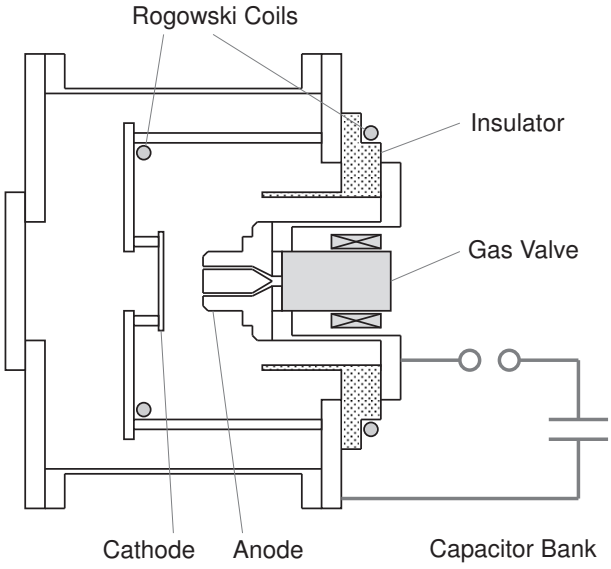

Fig. 1: Schematic diagram of the SHOTGUN z-pinch device.

In this paper the difference of the shape and the dispersion process of the material on the kind of gas is reported.

2 Experimental Device

The experiment was conducted on the SHOTGUN z-pinch device at Nihon University (Fig. 1). The energy storage section of the device consists of 30 kV 24 μF capacitor bank, and the maximum discharge current is 300 kA. The charg-

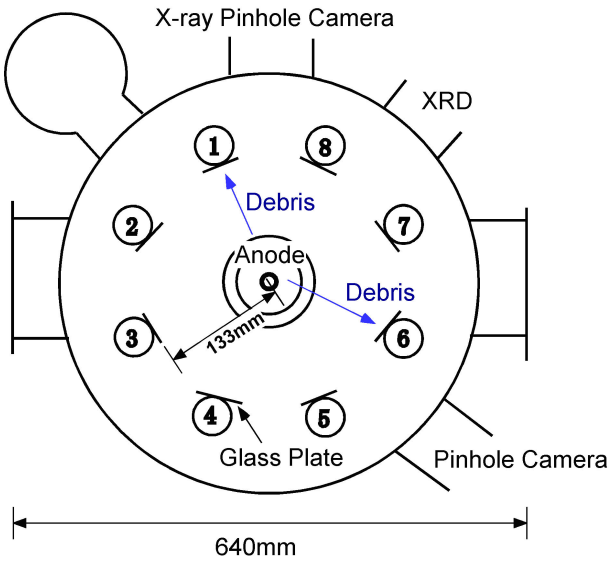

Fig. 2: Arrangement of the eight glass plates in the discharge chamber.

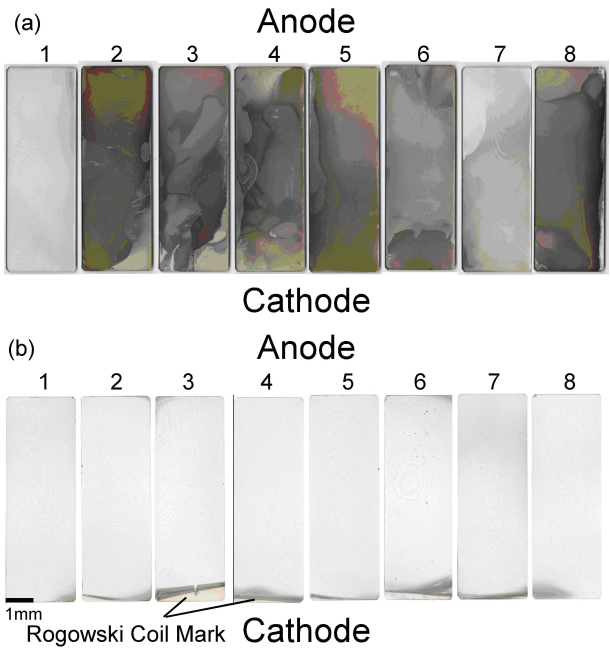

Fig. 3: Collected materials on the glass plates in (a) He and (b) Ar discharges.

ing voltage of the bank was 25 kV (7.5 kJ) in this experiment.

The center conductor is anode. The isolated gas distribution can be formed between the electrodes by a hollow Laval nozzle mounted on the anode. The nozzle diameter and the electrode separation are both 30 mm. The gases used here were He and Ar, and the prenum pressure was 5 atm.

Sn sheets were placed on the surface of cathode made of stainless steel. The anode was made of graphite in order to reduce vapolization or dispersal of the electrode material.

3 Dispersion Materials

As the dispersion materials mainly come from between the electrodes[2], eight glass plates were put on each inner face of the return rods to collect the material (Fig. 2). The distance between the device center and the glass plates was 133 mm. The size of the glass plate was 26 mm $\times$ 76 mm. The materials collected by the glass plates after discharges are shown in Fig. 3.

The glass plates after 36 shots of He discharge are shown in Fig. 3(a). Most of the glass plates were darkened by the dispersion materials. The glass plates 1 and 7 are little compared to the other plates. The dispersion material was not isotropic to the azimuthal direction, and this reproduced the result before [2].

The glass plates after 65 shots of Ar discharge are shown in Fig. 3(b). In contrast to the He discharge, the dispersion material seemed not to be collected by the glass plates. However, there were detailed wounds in all of the eight glass plates like the frosted glass. In addition, the adhesion of the particles was confirmed from the glass plates 2 and 6. Here, changing color on the cathode side seen in the entire eight glass plates is a mark of the Rogowski coil to measure the cathode current, and it is understood that the material adheres slightly in the part of this shadow. It is understood from the results that the state of the dispersion material is greatly different between the operating gases.

The glass plates were observed by a microscope. Figure 4 shows the microscopic view of the glass plate in (a) He discharge and (b) Ar discharge. It is understood from the He discharge that the fine particles of diameter 150$\sim$250 μm pile up on the filmy dispersion material. A lot of stripes were observed on the glass plates in the Ar discharge, which was found to be a detailed crack. And the particles with diameter of few μm were observed on the plates. It is found that the state of the dispersion material was quite different with the operating gas. The shape and the elements of the dispersion material were examined by using the scanning electron microscope (SEM) and the energy dispersive x-ray spectroscopy (EDX).

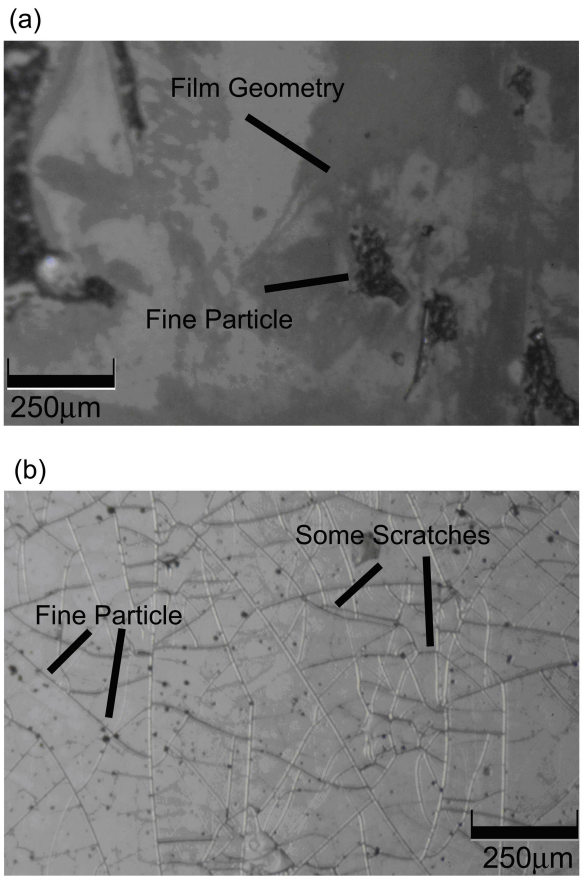

Fig. 4: Observation of the glass plates with a microscope. (a) He and (b) Ar discharges.

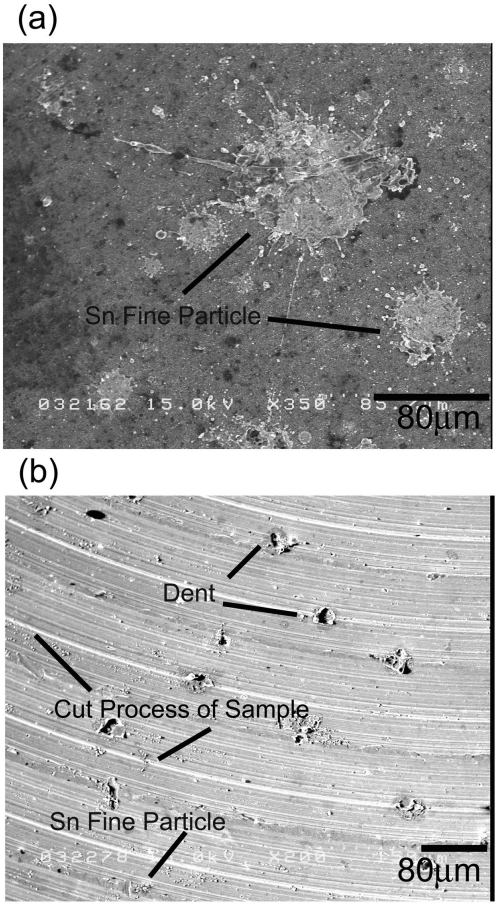

Fig. 5: Dispersion materials observed using the SEM in (a) He and (b) Ar discharges.

4 Observation by SEM

In order to observe the dispersion material using SEM, a metal stage (Al, ϕ15 mm × 6 mm) was placed in the device. The scanning electron microscope (FE-SEM) HITACHI S-4500 was used for the observation. And the elemental analysis of the observed material was done with the EDX device attached on the microscope. The SEM images of the surfaces of the metal stages after some discharges are shown in Fig. 5.

Figure 5 (a) shows the SEM image of the surface of the metal stage exposed over 150 shots in He discharge. It was confirmed that dripping particles adhered to the whole face of the metal stage. It is thought from the shape of the particles that they get cold and hardened at the collision with the stage, while they are melting in the dispersion. It is understood that the dispersion material is rapidly cooled on the surface of the stage unlike Fig. 4 (a). The size of the particles on the stage is about 1∼100 μm.

Figure 5 (b) shows the SEM image of the surface of the metal stage exposed over 83 shots in Ar discharge. A series of curved lines are the marks of cut process of the stage. A lot of small dips (20∼40 μm in diameter) were observed on the surface of the stage. It is thought that these dips were formed by the collisions of the dispersion materials with the surface of the stage. Although the dispersion material that had piled up on the metal stage was not remarkably observed, some round particles of about several μm were observed to adhere to the surface. It is thought that most of the dispersion materials rebound by the collision with the stage and are not piled up. And it is also thought that the dispersion material collided with the stage after getting cold and having hardened.

The above-mentioned results indicate the possibility of the kind of operating gas to influence on the temperature of the dispersion material.

The componential analysis was done using EDX by taking out a part of the area shown

in Fig. 5. The component of the particle in the He discharge was was Sn. The component of the particle in the Ar discharge was also Sn. However, the amount of piling up was a little in the latter case.

Besides, C, Cu and Fe were detected as the major components. It is thought that C has come from the graphite anode. And, it is thought that Cu and Fe have come from the chamber wall or the metallic materials sputtered by the contact with the plasma.

5 Summary and Discussion

He and Ar discharges have been done in the gas-puff z-pinch with Sn electrode, and the difference of the formation of the dispersion material between the two kinds of gases was examined.

In the He discharge, the dispersed material collected by the glass plates were not isotropic to the azimuthal direction. This reproduced the result before[2]. When the glass plates were observed by the microscope, the fine particles of diameter 150∼250 μm were observed to adhere on the filmy dispersion material. When the Al stage was observed by the SEM, a liquid drop of Sn fine particles were observed to adhere on the stage. A particle size was 1∼100 μm in diameter. It is understood that the particles observed on the Al stage were rapidly cooled by contact with the stage, though the particles observed on the glass plates were not like the drippings. That is, the fine particles generated by the He discharge were melted while having been dispersed.

On the otherhand the entire glass plates become like frosted glasses in the Ar discharge, and the dispersion material has not piled up remarkably. When the glass plates were observed by the microscope, a lot of stripes were observed to the glass plates, and they were detailed cracks. And some fine particles adhered to the crack were observed. When the Al stage was observed by the SEM, a lot of dips were observed to the surface of the stage. The adhesion of the fine particles was not remarkably seen on the surface of the Al stage. It is thought that the cracks on the glass and the dips on the stage were formed by the collisions of the dispersion material, and most of the materials were rebounded after their collisions. And it is also thought that the fine particles generated in the Ar discharge were solidified.

It was clarified that there was a difference in the form of the dispersion materials depending on the kind of the operating gas. This difference is thought to be generated in the generation or the dispersion process of the dispersion materials. The plasma temperature is thought to be high in the He discharge from the first stage of the discharge, and the melt of the Sn electrode is advanced in the generation process. And the cooling of Sn particles is thought to be advanced in the Ar discharge, because the mass of Ar atom is larger than that of He, and the collisions with the heavier atoms will remove more thermal energy from the Sn particles. We cannot conclude which the cause is only by this experiment.

In both discharges the fine particles are generated from the electrode material, and it is thought that these particles are charged by the contact with the plasma. And the charged fine particles disperse to surroundings by the electromagnetic field, when the plasma collapses.

References

[1] K. Takasugi et.al., Jpn. J. Appl. Phys. **35**, 4051 (1996).

[2] K. Takasugi and A. Maeda, NIFS-PROC-79, 35 (2009).

Demonstration of Compact Magneto-hydrodynamic Acceleration using Fast Pulsed-power Discharges

Toru Sasaki,[1,*] Atsushi Kubo,[1] Tatsuya Suzuki,[1] Takamitsu Watahiki,[1] Yuuki Naganuma,[1] Takashi Kikuchi,[1] and Nob. Harada[1]

[1] *Department of Electrical Engineering, Nagaoka University of Technology Kamitomioka-cho 1603-1, Nagaoka, Niigata, 940-2188, Japan*

A compact magneto-hydrodynamic (MHD) acceleration due to pulsed-power discharges using a model rocket engine was demonstrated. To observe the exhaust gas velocity, we were developed an optical detecting system based on time of flight method. The combustion gas temperature was estimated by a time-splitting spectrometer. Results indicated that the velocity of combustion gas/plasma using pulsed-power discharges could be accelerated about two times faster than that of conventional ones. Compared to the performance of the model rocket engine, the pulsed-MHD thruster has overwhelming thrust force and specific impulse.

Keywords: Magneto-hydrodynamic Acceleration, Pulsed-power discharges, Model Rocket Engine

I. INTRODUCTION

Cosmic-space propulsion systems are necessary to understand the origin of universe, the principle of physics, and so on [1–4]. To explore the universe, a compatible propulsion system as a thrust force and a specific impulse is required. Electric propulsion systems can reduce a propellant mass compared to the chemical rocket engine, that is, the propulsion systems have highly specific impulse. A next generation of cosmic-space propulsion systems are needed to approve lifetime, lower thrust force, and complex structure.

Performances of electric propulsion is decided by not only thrust force and specific impulse but also thrust efficiency. The thrust efficiency η as a relation between the thrust power $P_{\rm kin}$ and the electric input power $P_{\rm e}$ is expressed as,

$$\eta = \frac{P_{\rm kin}}{P_{\rm e}} = \frac{\frac{1}{2}\dot{m}v_{\rm out}^2}{P_{\rm e}}, \tag{1}$$

where $\dot{m}$ is the mass flow rate of the propellant, and $v_{\rm out}$ is the exhaust velocity. The thrust force F of the electric propulsion is strongly depends on the exhaust velocity as $F = \dot{m}v_{out}$ and the specific impulse $I_{\rm sp}$ is written by $I_{\rm sp} = v_{\rm out}/g$. From above these relations, the thrust power ratio is expressed as,

$$\frac{F}{P_{\rm e}} = \frac{2\eta}{gI_{sp}}. \tag{2}$$

Figure 1 is the typical thrust force and specific impulse for each thruster. Equation (2) indicated that the thrust force and the specific impulse is trade-off. The thrust efficiency η is critical factor to make an efficient thruster.

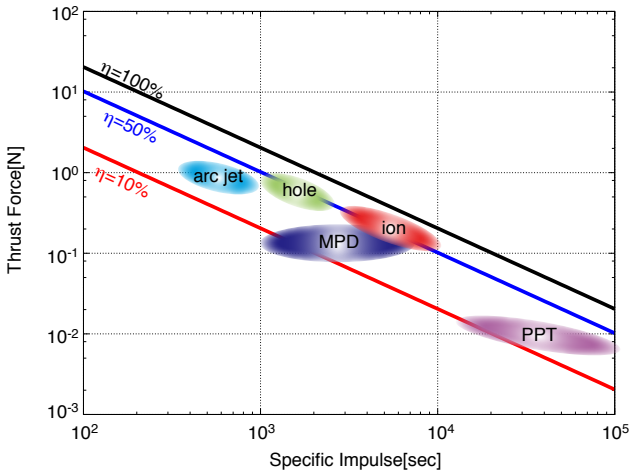

FIG. 1: Typcial parameters of thrusters. The lines are indicated the thrust efficiency of each percentage

Therefore, the electric propulsion system should be translated from the electric input power to the thrust power.

A magnethydrodyanmic (MHD) thruster is one of the electric propulsion system generating Lorentz force into the plasma. Characteristics of MHD thruster are (1) unused neutralizer because of plasma ejection, (2) highly thrust force compared to the ion thrusters, and (3) highly specific impulse compared to the chemical engines. However, the MHD thruster has problems as the lower ionization degree and the required strongly external magnetic field. To solve these problems, the MHD thruster is considered the preionization using the fast pulsed-discharge acceleration [4].

Improving thrust efficiency for MHD thruster, we focus on the fast pulse discharge. The fast pulse discharge can generate not only the ionized exhaust gas but also the

*Electronic address: sasakit@vos.nagaokaut.ac.jp

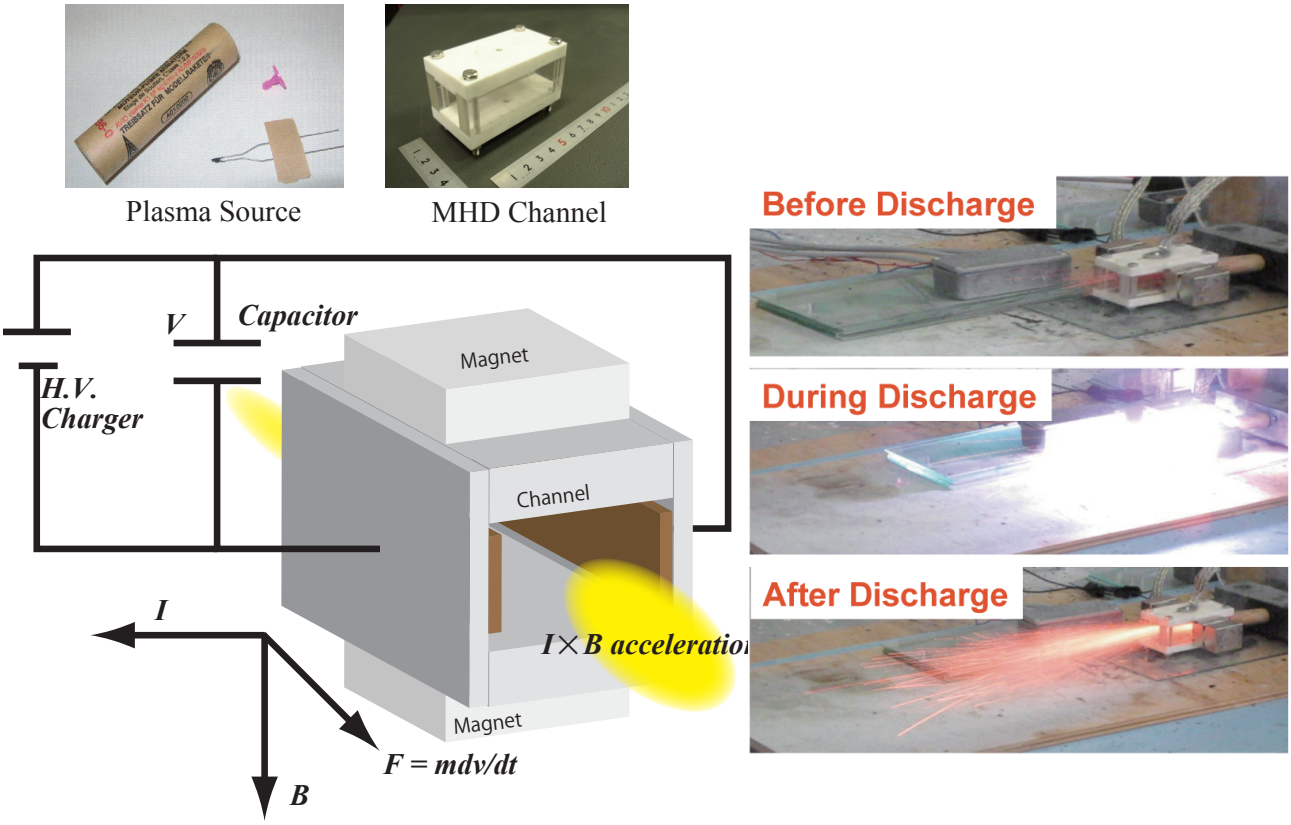

FIG. 2: Images of pulsed-MHD acceleration.

generating self-magnetic field caused by the large current density. Demonstrating pulsed-MHD thruster, we evaluated the exhaust gas velocity and temperature.

II. EXPERIMENTAL SETUP

A schematic diagram of a experimental apparatus is shown in Fig. 2. A plasma source is a model rocket engine, in which is a black powder including Potassium. The plasma source is easily generated the ionized gas compared to the ordinary gases. Therefore, the electrical conductivity and the ionization degree of the plasma source are increased by the other energy sources. The time duration of the model rocket engine is about 2 sec with 5 N of the average thrust force [3, 4].

A plasma channel is made of machinable ceramics and sapphire because of well performance of insulation and heating resistance. To observe the interior of plasma, we select the sapphire wall. In order to estimate the thrust performance, we developed linear-shape accelerator of MHD. The size of the plasma channel is 20×20 mm in height and width, and 75 mm in length.

An applied magnetic field is used to a Neodymium magnet ($Nd_2Fe_{14}B$), of which the magnetic flux density is 0.46 T on the surface. The size of magnet is $30 \times 30 \times 15$ mm. Figure 3 shows the distribution of magnetic flux density generated by the magnet. The magnetic flux density is obtained by the magnetic probe. The results shows that the magnetic flux density in the plasma channel is 0.2 T around the magnet.

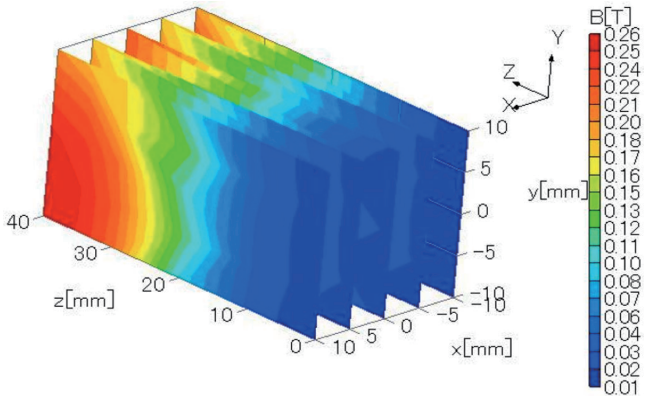

FIG. 3: Distribution of magnetic flux density in the channel.

We also estimated the combusted gas/plasma temper-

ature by using a spectroscopic method assuming black-body radiation. The black-body intensity of combustion gas/plasma $I(\lambda, T)$ is

$$I(\lambda, T)\, d\lambda = \frac{2hc^2}{\lambda^5} \frac{1}{e^{hc/k_B T\lambda} - 1} d\lambda, \tag{3}$$

where h is the Planck constant, k_B is the Boltzmann constant, T is the gas/plasma temperature, c is the speed of light, λ is the wavelength. The spectrum intensity was observed by the time-resolved spectrometer (PMA-12: HAMAMATSU). The exposure time of time-resolved spectrometer is 20 ms.

The velocity of combustion gas/plasma is estimated by the Time-of-Flight (TOF) method, in which is evaluated by a time-difference of gas/plasma emission. The time-difference of gas/plasma emission is detected by the high speed photo-diodes (S5971: HAMAMATSU) which is arranged at intervals of 2.5 cm. Therefore, the velocity of combustion gas/plasma v is

$$v = \frac{dl}{dt} = \frac{0.025}{t_{p1} - t_{p2}}, \tag{4}$$

where dl is the interval of photo-diodes, t_{p1} and t_{p2} are the peak-time of detection signal from the gas/plasma emission.

To obtain the efficient acceleration, we applied a pulse discharge using low-inductance capacitors, which is consist of $0.2 \times 2\mu$F. The timing of dish charge depends on the ignition of model rocket engine. The circuit inductance is estimated about 800 nH from the shunt circuit.

III. RESULTS AND DISCUSSIONS

Figure 4 shows the typical waveforms of the photo-diode signals and the discharge voltage. The results show that the photo-diode signals correspond to the discharge voltage. The noise of photo-diode signals occurred due to exposed by the combustion gas/plasma. However, the photo-diode signals were enough to detect for the evaluating velocity of combustion gas/plasma without the beginning of discharge at 0 sec.

Figure 5 shows the comparison of combustion gas/plasma velocity with and without pulsed-discharges. In case of without pulsed-discharge, the average velocity of combustion gas/plasma is estimated to be from 700 m/s to 800 m/s. On the other hand, the average velocity of combustion gas/plasma with pulsed-discharge is estimated to be from 1000 m/s to 1200 m/s. These of average velocity depend on the individual difference of model rocket engine. Meanwhile, the increasing velocity with pulsed-discharge is corresponded to the timing

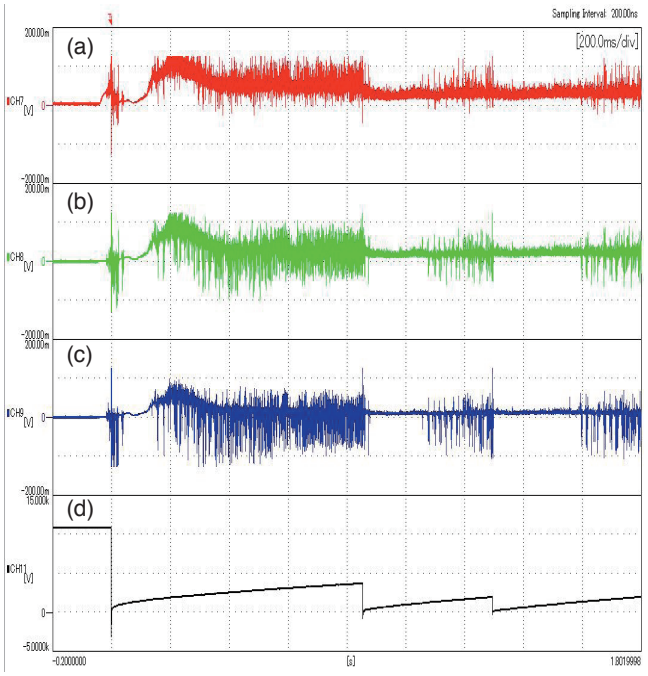

FIG. 4: Typical time evolution of (a)-(c) the photo-diode signals, and (d) the discharge voltage.

of applied voltage. The maximum velocity of combustion gas/plasma is 2.2×10^3m/s at the timing of second discharge.

In order to evaluate the increasing velocity, we observed the temperature of combustion gas/plasma as shown in Fig. 6. It indicates that the both temperatures of combustion gas/plasma are estimated to be about 1900 K. Therefore, the pulse-discharge is not thermally affected to the combustion gas/plasma. The temperature of combustion gas/plasma with pulsed-discharge was also estimated by the resistivity of combustion gas/plasma. The temperature is estimated to be 3000 K at the timing of discharges.

From these experimental results, we evaluate the dynamics of MHD acceleration for the model rocket engine. The velocity without the pulsed-discharge, in which can be assumed driven by the pressure gradient between the exit of model rocket engine and the end of channel, is estimated to be about 700 m/s. Therefore, we assumed the isentropic expansion, as follow;

$$u_e = \sqrt{2C_p T_0 \left\{ 1 - \left(\frac{p_e}{p_0} \right)^{\frac{\gamma-1}{\gamma}} \right\}}, \tag{5}$$

where u_e is the exit velocity of isentropic condition at the end of channel, C_p is the specific heat of constant pressure, γ is the adiabatic constants, and p is the pressure of which subscripts of e and 0 respectively denotes the po-

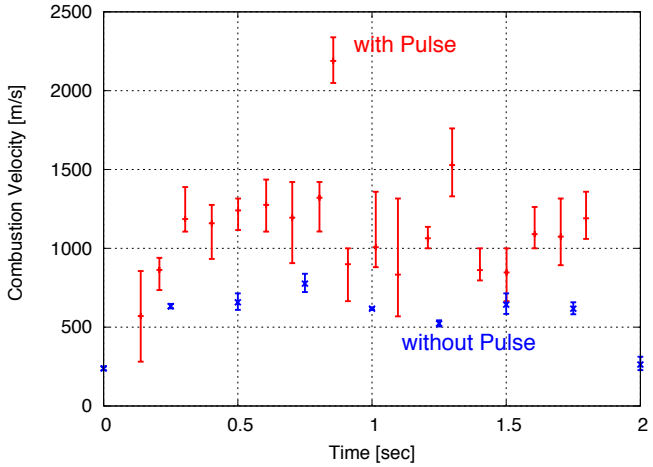

FIG. 5: Comparison of the time evolution of the combustion velocity with and without pulsed-discharges

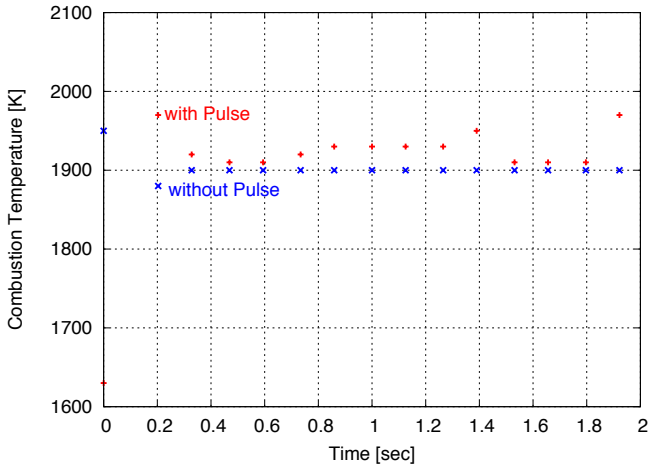

FIG. 6: Comparison of the time evolution of the combustion temperature with and without pulsed-discharges

sition at the end of channel and the exit of model rocket engine. The adiabatic constant γ and the specific heat are estimated to be 1.12 and 757 J/kg by using the ETL code [5]. In the isentropic condition, we can evaluate the maximum velocity u_{max} of isentropic condition assuming the infinite pressure at the exit of model rocket engine, as follows,

$$u_{max} = \sqrt{2C_pT_0}. \tag{6}$$

From eq. (6), the maximum velocity u_{mas} is estimated to be 1.5×10^3m/s. The maximum velocity from observations is faster than that of isentropic conditions.

The pressure at the end of channel is also assumed the atmospheric pressure about 0.1 MPa. From these assumption, we can derive the average number density of atom which is about $4 \times 10^{19}\mathrm{cm}^{-3}$. The interior pressure of model rocket engine is estimated to be 1.6 MPa by using the assuming atomic number density. The theoretical velocity u_{th} of isentropic condition is derived to be 1.1×10^3 m/s by using those pressures. Based on the theoretical velocity, the relation between the pressure and the combustion velocity u_{eth} driven by the MHD effect is estimated by the conservation low, as follow,

$$u_{eth} - u_{th} = \frac{P_{MHD}}{\rho l}\Delta t, \tag{7}$$

where P_{MHD} is the magnetic pressure, ρ is the average density, l is the characteristic length of MHD effect, and Δt is the typical time duration driven by the magnetic pressure as $\Delta t \sim l/u_{eth}$. We estimate the MHD force based on the parameters which are 40 mm in the characteristic length, and the average density derived by the mass of black powder (70 amu) crossed the number density. The estimated MHD force is 10 MPa in the channel. The thrust force of MHD is also estimated to be 4×10^3 N and is higher than that force of model rocket engine. The highly magnetic flux is generated not only by the applied magnetic field but also by the large current. The theoretical MHD force from the predicting applied current is evaluated to be 3 MPa. The theoretical force is smaller than the estimated force as 10 MPa. The difference of the theoretical and estimated forces is due to the self magnetic field.

IV. CONCLUSIONS

A compact magnetohydrodynamic (MHD) acceleration due to pulsed-power discharges using a model rocket engine was demonstrated. To observe the exhaust gas velocity, we were developed an optical detecting system based on time of flight method. The exhaust gas temperature was estimated by a time-splitting spectrometer. Results indicated that the exhaust gas velocity using pulsed-power discharges could be accelerated about two times faster than the conventional combustion gas/plasma velocity. Compared to the performance of the model rocket engine, the pulsed-MHD thruster have overwhelming thrust force and specific impulse. Understanding efficient acceleration, we will develop not only the well-defined pulse generator but also the numerical simulation.

[1] T. Moeller, R. Rhodes, J. T. Lineberry, L. L. Begg, and R. J. Litchford: 'HVEPS Combustion Driven MHD Power Demonstration Tests', AIAA Paper, p.4097 (2008).

[2] N. Harada and S. Takahashi: 'Numerical Simulation of Performance of MHD accelerator', AIAA paper, p. 4288, (2003).

[3] Toshio Sasaki and Nob. Harada: 'Temperature Measurement of Combustion Gas Plasma with the Use of Optic Device', Proc. 18th IEEJ, Niigata, p.137 (2008).

[4] A. Kubo, T. Suzuki, K. Suwa, T. Sasaki, T. Sasaki, T. Kikuchi, and N. Harada: 'Recent Progress of Compact MHD Experiment in Nagaoka University of Technology', Proc. 17th International Conference on Energy Conversion, 4-6, (2009).

[5] K. Takano and K. Kato: 'Chemical equilibrium calculation program of MHD flue gases', Proc. 17th Symp. Efficient Use of Energy and Direct Electrical Power Generation ECRI-SYM-11, pp173-181 (1989).

RESULTS OF THE ELECTRON SPECTROMETER ON FF01 SERIES OF FIREX-I PROJECT

T. Ozaki, M. Koga[1], H. Shiraga[1], H. Azechi[1], H. Sakagami and FIREX Group[1]

National Institute for Fusion Science, 322-6, Oroshi, Toki 509-5292, Japan
[1] Institute of Laser Engineering, Osaka Univ., 2-6, Yamada-oka, Suita, 565-0871, Japan

ABSTRACT

In fast ignition, it is essential to heat an imploded core by a hot electron, which is produced by an auxiliary heating laser. We have re-calibrated an electron spectrometer against the electron energy and intensity, which had been developed last year. The integrated experiment, which is combination with the Gekko XII and the LFEX lasers, has started from this year. The spectra differences of the hot electron between target species and power dependence can be obtained. The spectrum of the hot electron when the effective core heating by the hot electron occurs, is obviously different from the spectrum without the effective heating. The electron temperature of the hot electron is too high to obtain the effective core heating because the pre-pulse of the LFEX laser is still large. Now the improvement of the laser specification has been proceeding.

I. Introduction

Fast ignition fusion[1)] is as follows;
A spherical shell target is imploded by lasers for compression, the imploded core is irradiated by an auxiliary strong heating laser. By those methods, an ignition can be achieved. The institute of Laser Engineering Osaka University has proposed that the spherical shell with gold conical guide is used as target. The heating laser (LFEX)[2)] is guided by the gold cone, which prevents the invading of the exploded plasma from the shell to the heating laser path. The hot electron is generated to the forward direction of the laser beam by irradiation of the LFEX laser to the tip of the gold cone. The hot electron hits and heats the imploded core. The suitable energy of the hot electron is determined by the areal density of the core to be less than several MeV[3)].

The pre-plasma, which is produced by the gold cone irradiation of the LFEX laser, is strongly related to the generation of the hot electron. The hot electron has spatially spread due to the complicated electro-magnetic dynamics, but mainly large amount at strait forward. The energy distribution depends on the pre-plasma scale length. Generally short scale length of the pre-plasma provides low energy hot electron, which is suitable for the core heating. Therefore the pre-pulse suppression is important for effective fast ignition.

The electron spectroscopic measurement is essential for investigating the mechanism of the core heating. The hot electron has isotropic spatial distribution. It is very interesting to study the effect of the anisotropy against the core heating efficiency. If the most proper value can be found in the spatial distribution, the laser irradiation and the target design can be changed.

Our goal is to obtain the accurate spatial distribution of the hot electron and to contribute the investigating of the mechanism of the core heating. The problem in this method is that the low energy electron cannot be obtained due to the extreme potential, which is created by the generation of the intense electron beam itself. Therefore there is the measurable limit in the electron spectrometer (ESM). In future we must compare the result of the x-ray measurement.

In this paper, we re-calibrate ESM#1[4)] more precisely than previous calibration[5)] especially the absolute calibration. The energetic electron spectra in the plane, conical and integrated targets irradiated by the LFEX laser can be obtained. The differences of the spectra between the effective and ineffective core heating are compared. We expect that our experimental results reflect the LFEX laser specification and the design of the integrated target.

II. Re-calibration of ESM

Last year we had performed the calibration of ESM, but we could not achieve the absolute

calibration because there were a few shots for calibration. As the thickness of the pinhole at the beam injection had been too short, the energy calibration had not been accurate. The thickness of new pinhole of 3 cm is used for obtain the sharp edge. The longitudinal shape of the pinhole is arc so as to obtain the same flux of the electron for small miss alignment. As a result, the very sharp irradiation spot on the imaging plate (IP) [6] can be obtained.

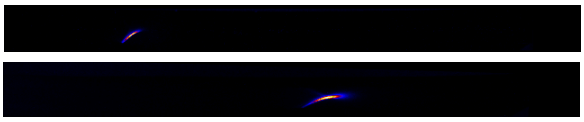

Fig. 1

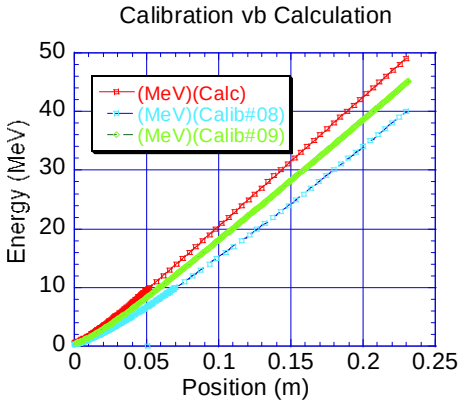

Fig. 2

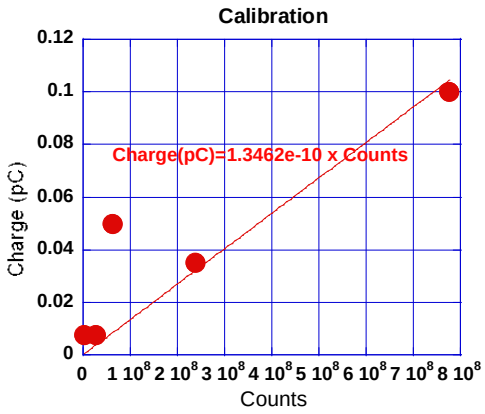

Fig. 3

Calibration has been performed at 9.5 MeV, which is almost minimum energy limit, and 27 MeV on L-band LINAC[7] in the Institute of Scientific and Industrial Research, Osaka University. Beam intensity is minimized so as to prevent the saturation of IP. Charge amounts from 0.01 pC to 0.1 pC are measured by the small size aluminum Faraday cup, where is installed behind the pinhole at the calibration shot. Typical irradiation spots on IPs are shown in Fig. 1. The energy calibration and absolute intensity calibration can be obtained as shown in Fig. 2 and Fig. 3, respectively. The energy calibration curve becomes more close to the calculation curve than previous calibration.

III. Comparison on various targets

From June to July and September to October in 2009, the experimental campaign "FF01", has been held. Target irradiation experiments have been done using one segment in 4 segments of the LFEX laser. Four different targets, aluminum and gold foils (10 μm-thickness), gold cone and CD (deuterium poly-ethylene, 500 μm-diameter) shell with gold cone are used. The LFEX laser energy is from 100 J to 1 kJ. The pulse width is 4 ps and 1.2 ps in the former and later experiments, respectively. The calibrated analyzer is installed on the Gekko XII[8] target chamber I at 159.1 degrees (port number 47) against the laser injection direction where is almost at the rear side of the target but slightly oblique. Therefore the observation of the intense hot electron can be expected.

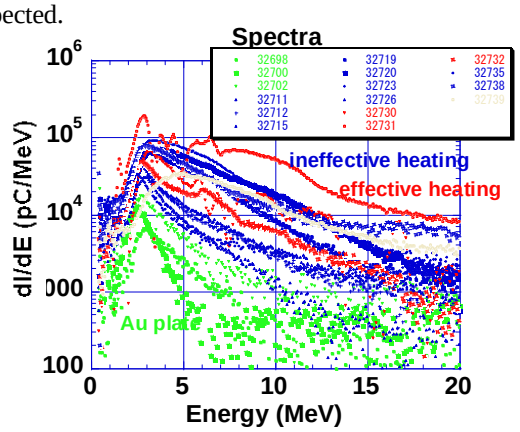

Fig. 4

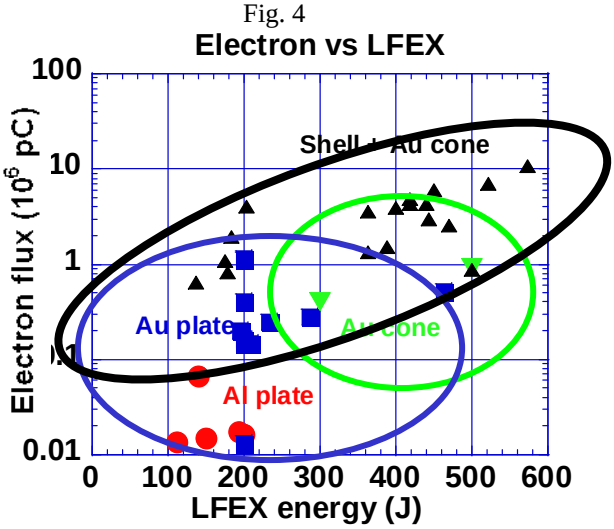

Fig. 5

Spectra difference and the electron flux v.s. laser power at various targets are shown in Fig. 4 and Fig. 5, respectively. The hot electron flux in gold plane is obviously smaller than tat in shell with gold cone. The reason is that the return current in shell with cone can be easily created although it is not enough due to the geometrical configuration in plane targets and the virtual cathode creates.

In Fig. 6, the electron temperature can be obtained from the approximation including the relativistic effect,

$$\frac{dN}{dE} = \left(\frac{N_0}{T}\right)\left(\frac{E}{T}\right)^2 \exp\left(-\frac{E}{T}\right), \qquad (1)$$

where N, and T are the beam amount and the effective electron temperature, respectively. According to the simulation result[9], there is the positive correlation between the hot electron temperature and the pre-plasma scale length. The hot electron temperature is strongly depended on the pre-plasma, which is created by the pre-pulse of the LFEX laser. If the hot electron energy is too high, the energy coupling from the electron to the imploded core becomes worse because the electron passes through the imploded core. It is important to produce the hot electron whose energy is within its range of the imploded core. The hot electron temperature becomes gradually higher at gold plane, gold cone and shell with cone. In gold cone, the pre-plasma is filled in the cone tip by the exploding pre-plasma from the cone inner wall. Therefore the hot electron temperature is higher because the scale length in gold cone expands than in the gold plane. The hot electron temperature in aluminum plane target is higher than in gold plane target because the growth rate of pre-plasma in low-Z material is higher than in high-Z one.

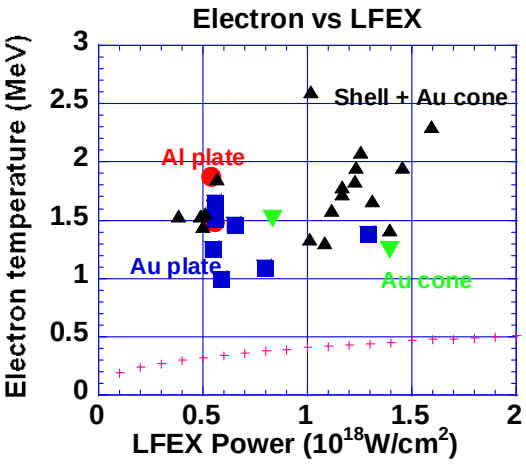

Fig. 6

As the current shell with cone target is not optimized yet, a part of the exploded plasma from imploding shell may enter to the cone. Therefore the hot electron temperature in shell with cone is higher than in other cases. In Fig. 6, pink plus symbol shows the scaling derived from the results in the PetaWatt experiment.

$$T_e(MeV) = 0.4 \times \left[\left(\frac{I_L(W/cm^2)}{10^{18}}\right)\lambda(\mu m)^2\right]^{1/3}, \qquad (2)$$

where T_e and I_L are the effective electron temperature and the laser beam intensity, respectively[10]. The hot electron temperature in the LFEX laser experiments are always higher than that in the PetaWatt laser experiments. This means that the pre-pulse in the LFEX laser is higher than that in the PetaWatt laser. The optimization of the LFEX laser is now proceeding so as to suppress the pre-pulse to 10^{-8} level.

The lower energy electrons less than 2.7 MeV may not be observed in any spectra because the large potential is appeared due to the virtual cathode.

IV. Integrated experiments

The integrated experiment means that the spherical shell of the CD shell with gold cone target is irradiated by the Gekko XII laser, the imploded core with maximum compression is auxiliary y heated by the hot electron which is generated by irradiation of the LFEX laser to the cone tip.

In “the Nature experiment” [11], the PetaWatt laser had been used as the heating laser, The maximum neutron yield enhancement of 1000 times could be obtained between with and without heating of the PetaWatt in the Nature experiment. In this experiment, we retry the Nature experiment by using the LFEX laser instead of the PetaWatt laser.

Nine laser beams are used for the implosion of pellet because the residual 3 beams are close sight lines of the gold cone. The average energy of each beam (green beam 0.53 μm) is 200-400 J. In order to complete the auxiliary heating, many relevant components should be improved. First is the timing of the LFEX laser timing. The coincidence between the Gekko XII and the LFEX lasers can be optically performed at the beam source, but cannot be changed after the discharge of laser amplifier. The best coincidence is roughly known by the simulation. The time window is within several tens to 100 ps, which is determined the stagnation time of the imploded core. However there is a jitter because the imploded core creation times are different due to the discrepancy of the Gekko XII laser energy. In the experiments, we choose most favorite shots in many shots. Second is the positioning of the imploded core.

This is due to the non-uniformity of each beam in the Gekko XII laser. Different laser power of a certain beam provides different ablation velocity, and moves the imploded core to off-center position as a result. The positioning of the LFEX laser is also important. By the vibration of the optics, the focal spot position of the LFEX laser is scattered. Third is the focal spot size of the LFEX laser. The LFEX laser consists of four independent components. This optimization is now proceeding. Forth is the pulse duration of the LFEX laser. Fifth is the effect of laser pre-pulse. The pre-pulse is related not only to the energy spectrum of the hot electron but also to the generation position of the hot electron. Sixth is the dependence of the laser power, and last is the design of target configuration, which is including the conical shape, cone material and so on. In this experiment, we describe the dependences of laser power and timing.

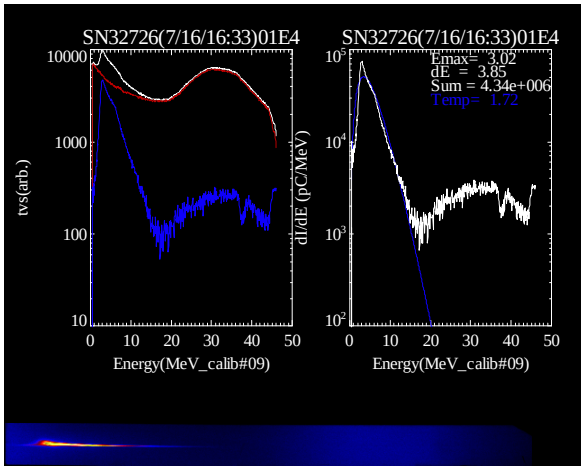

Fig. 7

Typical LFEX laser spot size is 30 x 60 μm. The spot size is confirmed by the irradiation of aluminum plane target. The imploded core size is monitored by the x-ray backlight to be 20-30 μm. In order to obtain more efficient energy coupling, the focusing of the LFEX laser is important. The position deviation of the LFEX laser is +-50μm in current configuration due to the vibration in optics. We choose the best shot in many trials. The position and focal size of the spot are monitored by the x-ray pinhole camera from the behind of the gold cone in integrated target.

Figure 7 shows the typical spectrum of the hot electron in the integrated target irradiated by the Gekko XII and the LFEX lasers. On left figure of Fig. 7, white, red and blue lines show the total signal, x-ray background and the real signal, respectively. Intense x-ray is generated from gold cone and target chamber hit by the hot electron at the irradiation of the LFEX laser. X-ray from imploded core is negligible. Therefore the real electron flux can be obtained by subtracting x-ray signal on the IP from total signal. Signal up to 20 MeV can be observed. *dN/dE* (white) and the fitting derived by (1) (blue) are shown on the right figure of Fig. 7.

Figure 8 shows the comparison of spectra between the effective and ineffective heating on the imploded core. The effective heating occurs when the timing of the LFEX laser irradiation correspond the imploded core creation time. When the hot electron hits the imploded core, the energy of the hot electron is reduced in the imploded core. The spread of the hot electron beam is larger than the exploded core in this configuration. The viewing position is oblique against the LFEX laser beam line. Therefore the hot electrons pass through the plasma of different thickness.

The time difference between the LFEX laser irradiation and the imploded core creation is monitored by an x-ray streak camera. When the hot electron hits the imploded core, the decelerated spectra as shown in Fig. 8 can be observed because the hot electron energy is decelerated due to the imploded core. In this configuration, the sight line of the ESM shifts from the line between the hot electron generation point and the imploded core. The hot electron passes through the exploding region around the imploded core, where the density is fluctuated. Therefore the disturbed spectrum can be observed when the generation timing of the imploded core corresponds the LFEX laser injection timing.

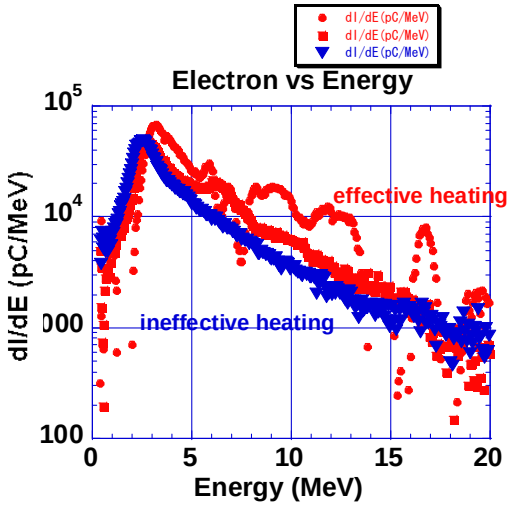

Fig. 8

At this timing, the maximum neutron yield can be observed by the time-of-flight scintillator photo-multiplier. The neutron is generated by the thermonuclear DD reaction in CD-shell. The neutron yield is strongly depended on the ion temperature of the imploded core. The neutron yield is large at the

high hot electron flux as shown in Fig. 9. This means that the increasing of the neutron yield is due to the auxiliary heating by the hot electron derived by the LFEX laser. Maximum amplification factor of 40 times can be achieved by the auxiliary core heating in this experimental campaign. According to the analysis of the hot electron energy spectrum, the high-energy tail still remains due to the pre-plasma which is produced by the pre-pulse of the LFEX laser. By the suppression of the pre-pulse, we can expect the re-realization of "Nature experiment" and overtake it.

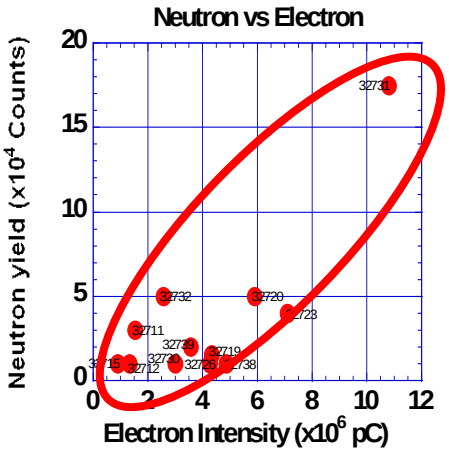

Fig. 9

V. Summary

The LFEX laser which heats the imploded core is the key device of the fast ignition in the FIREX-I. From this year, the integrated experiment, which is the combination between the implosion by the Gekko XII and the auxiliary heating by the LFEX, has started. The hot electron spectra differences in various irradiated targets and the power dependences can be obtained. The hot electron temperature is still too high to heat the imploded core efficiently because the large pre-pulse remains. The optimization of the LFEX laser should be necessary. It is important to reduce the effect of x-ray in the ESM measurement. Strong x-ray is generated not only from the target but also from the wall irradiated by the hot electron. X-ray will be reduced by covering the ESM with the low-Z material. Recently second the ESM has been completed. We will be able to study the spatial difference of the spectra in the next experimental campaign.

References

1) H.Azechi, et al, "High density compression experiments at ILE, Osaka", Laser Part. Beams 9, 193-207 (1991).
2) N. Miyanaga, et al., 2003 in Proc. of IFSA'03, ThF1.1.
3) T. Jozaki, "Core Heating Properties in FIREX-I 'Influence of cone tip'", Plasma Phys. Control. Fusion, 51, 014002 (2009).
4) T. Ozaki, et al., "Development of the compact electron spectrometer for the FIREX-I Project in Gekko XII", IFSA09.(to be submitted).
5) T. Ozaki, et al., "DEVELOPMENT OF THE ELECTRON SPECTROMETER FOR MEASUREING THE ENEGETIC ELECTRON FROM LFEX LASER IN FIREX-I PROJECT ", NIFS Report. (to be published)
6) http://www.duerr.de/.
7) http://www.sanken.osaka-u.ac.jp/labs/rl/facility.html.
8) Yamanaka C, et al., 1985 proc. 10th Int. Conf. London 3 3.
9) H. Sakagami, T. Johzaki, H. Nagatomo, and K. Mima, "Generation control of fast electron beam by low density foam for FIREX-I", Nucl. Fusion, 49, 075026 (2009)
10) Private communication.
11) R. Kodama, et al, "Fast heating of ultrahigh-density plasma as a step towards laser fusion ignition", Nature 412, 789-802 (2001).

RECENT TECHNOLOGY TRENDS OF THE SOLID-STATE HIGH VOLTAGE PULSED POWER SUPPLY

A. Tokuchi

Pulsed Power Japan Laboratory Ltd., 4-5-2 Nomura, Kusatsu shi, Shiga, 525-0027, Japan

ABSTRACT

High voltage pulsed power supplies are becoming further solid-state systems using semiconductor switches by the speed-up of semi-conductor switches and the progress of high frequency characteristics of pulse cores. Additionally, they are evolving to the suitable style for many kinds of industrial applications by the digitalization and modularization. While advancing the development of the SiC devices, it can be expected that they become smaller in size and result in creation of new industrial applications.

1. Important role of pulsed-power supply

At first, a pulsed power supply has an important role to achieve new industrial applications. Because a combination of new pulsed-power devices and new circuit makes new performances of the pulsed-power supply, and the new performances create new industrial applications.

For example, a combination of MOS-FET having high speed switching as a new pulsed-power device and series connection of the MOS-FETs in the inverter as a new circuit makes a new performance such as ±2kV, 20A, 1MHz, and these values are very high frequency, very high voltage and very high average output power. These new performance creates new accelerator concept known as an induction synchrotron[(1)] and this is expected to be used for material science, selective breeding and hybrid cancer therapy, etc..

In another case, a combination of MOS-FET having high speed switching as a new pulsed-power device and hybrid-charging circuit as a new circuit makes a new performance such as 50kV, 37kJ/s, 0.01% of charging voltage accuracy, and this value are very high accuracy. These marvelous performances achieves X-ray free electron laser in Japan[(2)] and this is expected to be used for imaging technology, ultra fast observation, protein structure analysis and live cell biology.

2. Keywords and technology trend

It is considered that the keywords required to expand a new industrial application with novel pulsed power supply are digitalization and modularization. Applications of the pulsed power supply are expanding to the industrial field, and the production method corresponding to mass production becomes important. In order to correspond to mass production, digitalization and modularization are quite important. A variety of pulse power supplies can be composed of the same power supply unit, and it comes to be able to correspond to mass production. The low cost and the high quality are obtained by the effect of mass production and the range of industrial applications is extending.

In addition, technology trends of the pulse power supply to expand an industrial application are as follows.

a. higher accuracy
b. higher frequency
c. higher speed

In addition, the range of an industrial application will extend though making to the unit advances structurally by the above-mentioned performance gain.

Especially, it seems that the pulse generating circuit where the combination of the semiconducting

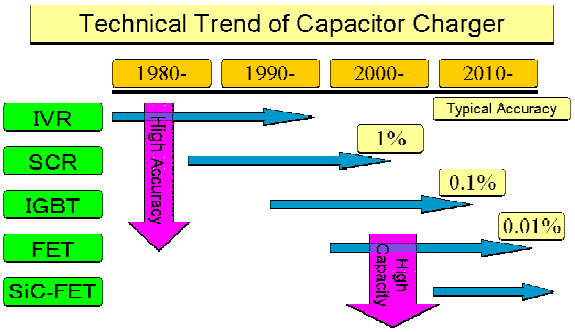

Figure 1 Technical trend of capacitor charger.

switch and the pulse core was used will become important in the future as a concrete technological technique.

3. technology trend of each unit

3.1 Capacitor charger or dc power supply

A technological intention of the charger in the future is as follows.

a. higher accuracy
b. higher efficiency and higher power foctor
c. smallersize
d. lower noise

Figure 1 shows a technical trend of the capacitor charger.

In the old age, we used IVR or SCR as control devices for capacitor charger. These devices are slow devices, so the accuracy is bad, such as 1%.

Recently IGBTs are most popular devices for high frequency inverter circuits. The inverter frequency is about 20kHz, this frequency is not so high and an accuracy is limited in 0.1% for the capacitor charger with repetitive operation such as 60Hz.

MOS-FETs are very fast switches. Switching time of the MOS-FETs is order of ns. Using MOS-FETs, we can get higher inverter frequency more than 100kHz, then we can obtain the high accuracy of 0.01%.

The capacitor charger of the Klystron modurator for X-FEL in Japan has achieved less than 0.01% of the voltage accuracy by using combination of IGBT inverter and MOS-FET inverter. Figure 2 shows the extra high precision high voltage capacitor charger of the Klystron modurator for X-FEL in Japan. Both fast charging and high accuracy are achieved by smooth switching from Main Charger (IGBT Inverter) to Sub Charger (FET Inverter). Using IGBT main charger, we can get rapid charging. The charging time from 0% to 99.7% is 10ms. After this period, the main charger stop the charging and FET sub charger charges from 99.7% to 100% in next 5ms. Finally we can obtain very high accuracy less than 0.01%. In this case the accuracy was 0.006%. This marvelous improvement of accuracy in charging voltage makes the beam quality high, and result in a high performance X-FEL.

In the next generation, As SiC devices develop, we can expect that the allowable power will become larger and the charger will become smaller in size, resulting in the creation of new industrial applications.

3.2 capacitor

A technological intention of the capacitor in the future is as follows.

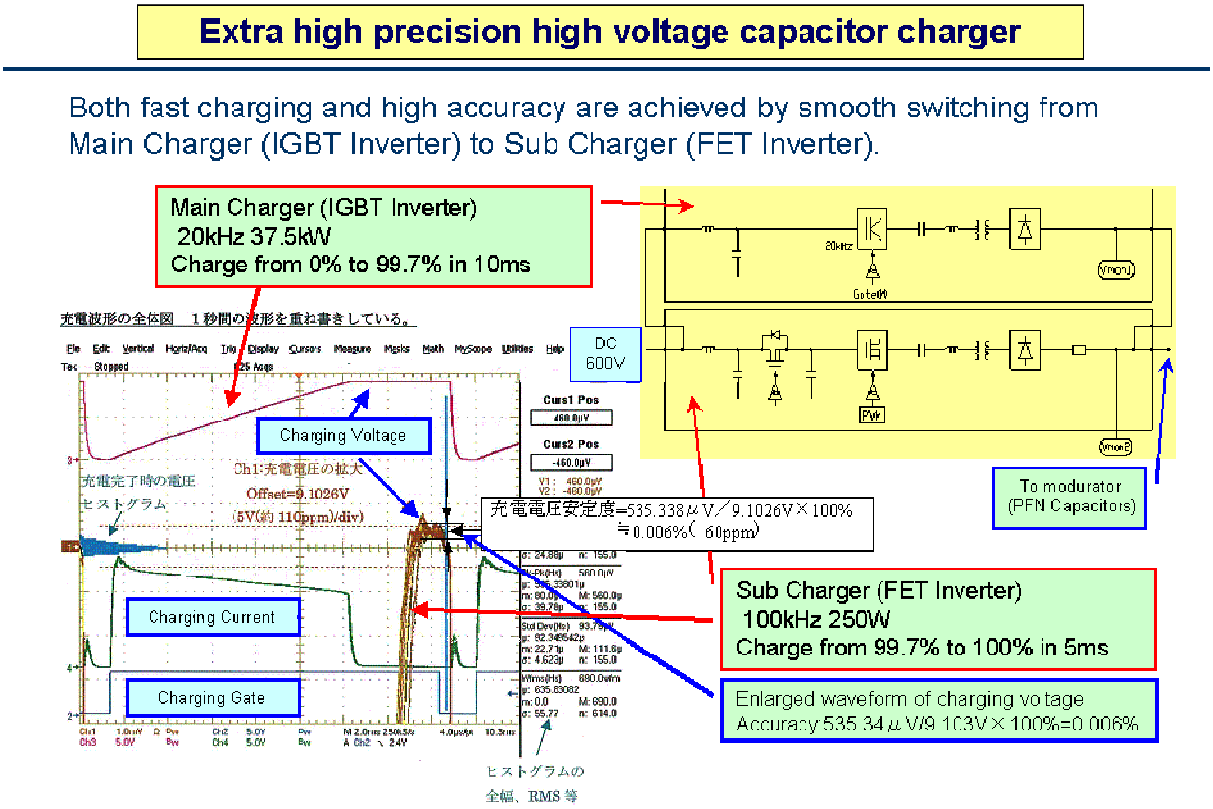

Figure 2 The extra high precision high voltage capacitor charger of the Klystron modulator for X-FEL in Japan.

a. lower inductance
b. larger current
c. longer life

Figure 3 shows a technical trend of the capacitor.

In the old age, we used liquid-filled capacitor, such as water or oil. The reason is that water has a high electric field strength as high as oil and a dielectric constant of the water is 40 times larger than the oil, then an energy density of the water-filled capacitor is 40 times larger than the oil capacitor. But very high power pulse machine using liquid capacitor such as Z-machine[3] is recently disappeared because of hardness to apply in the industrial application.

Recently a ceramic capacitor or a film capacitor is most popular device for many kind of induatrial pulsed power supply, for example, an excimer laser or a pulse klystron modulator.

An electric double-layer capacitor (EDLC) is attractive device as a higher energy density power capacitor. In the near future, it is expected for EDLC to be small-size capacitor having large stored energy used in small-size pulsed power supply.

A circuit of the pulsed power supply is changing from a pulse compression circuit using a pulse line to a direct switching circuit without the pulse compression circuit corresponding to increasing a switching speed of the switch. Then also the capacitor is required higher speed and larger current.

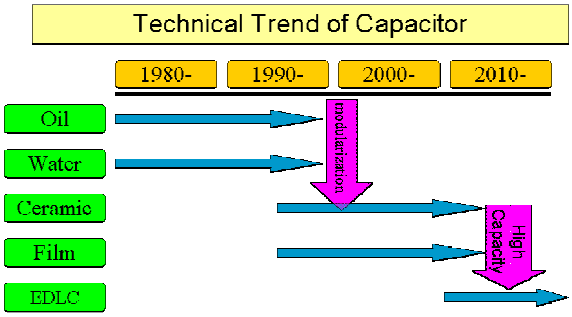

Figure 3 Technical trend of capacitor .

3.3 switch

A technological intention of the switch in the future is as follows.

a. higher speed
b. lower loss
c. longer life
d. higher heat dissipation

Figure 4 shows a technical trend of the switch.

In the old age, we used a spark gap or a vacuum tube as a high power switch. These discharge type switches have a large switchable power, however a short life and a low repetition rate of them are reasons not to expand to an industrial use.

Recently a performance of a semiconductor switch is rapidly improved. From GTO, IGBT to MOS-FET, the switching speed is highly improved. The major method to generate a high repetitive pulsed power is a combination of the semiconductor switch and a magnetic switch.

In the next generation, As SiC devices develop, we can expect that the switchable peak power of the semiconductor will be further improved, then the major method of pulsed power supply is changing to direct switch method without pulse compression.

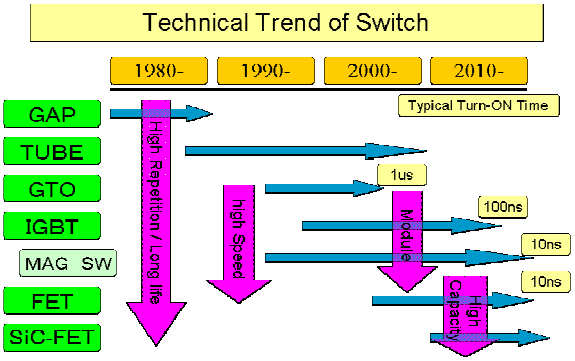

Figure 4 Technical trend of switch.

3.4 pulsed power supply circuit

A technological intention of the pulsed power supply circuit in the future is as follows.

a. higher repetition
b. longer life
c. higher speed
d. modularization

Figure 5 shows a technical trend of the pulsed power supply circuit.

In the old age, we used a MARX circuit to generate a high voltage pulsed power. But the repetition rate of the MARX circuit is low such as 10Hz, then the MARX circuit is recently disappeared because of the low repetition rate.

Recently pulsed power supply circuit using high voltage pulse transformer is used for many industrial applications such as an excimer laser generation.

The MARX circuit or the pulse transformer is hard to be correspond to a modularization, and each device become bigger. In the future, pulsed power supply

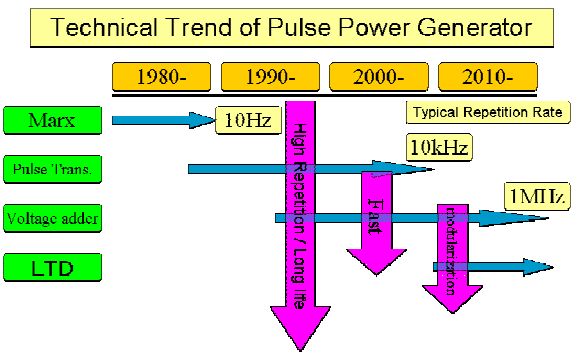

Figure 5 Technical trend of pulsed power generator.

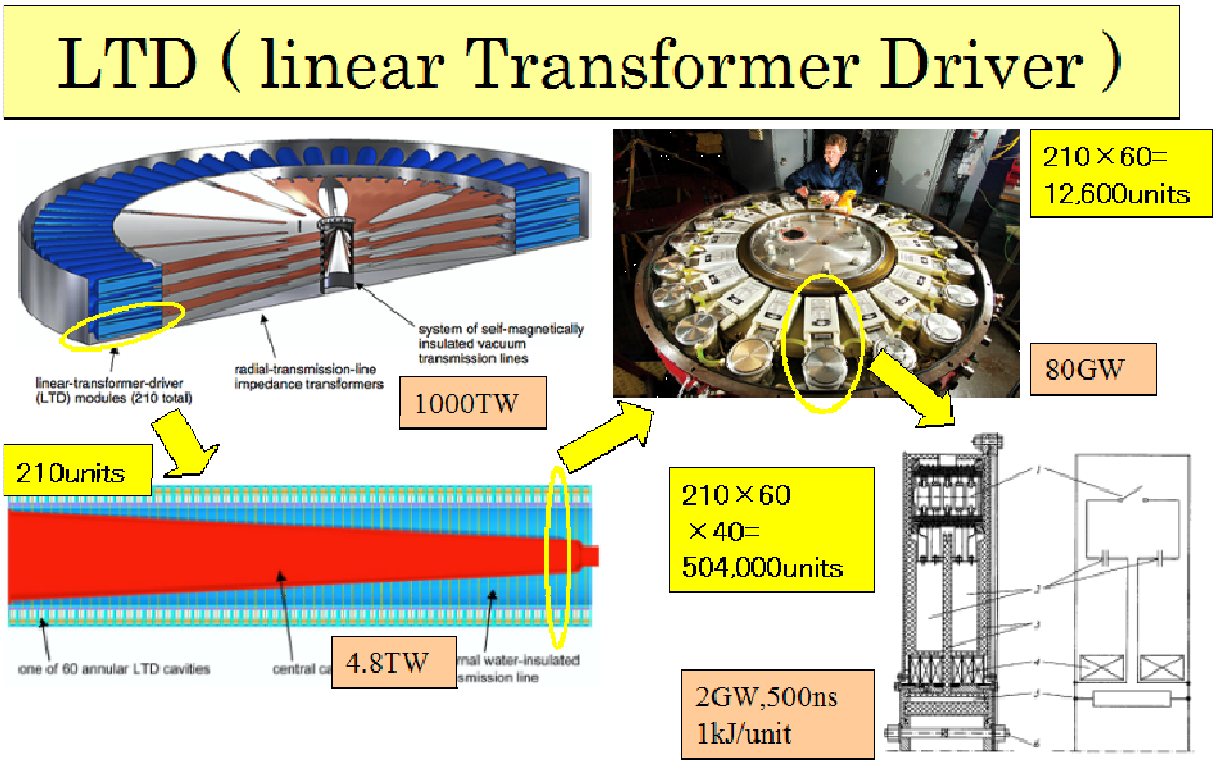

Figure 6 Linear transformer driver (LTD).

circuit will change to inductive voltage adder or linear transformer driver (LTD) [4].

Figure 6 shows a LTD explanation. The Z-machine generated an extra high power pulse using pulse compression circuits, thus the machine size was very big and hard to get modularization. The LTD generates an extra high power pulse using coincidently triggered many small units in parallel or in series. The current is increased by parallel connection, and the voltage is increased by inductively serial connection. We can choose the output power of the LTD by changing of a number of the small pulse power units. In the example shown in figure 6, a peak power of 1000TW will be obtained by using 504,000 numbers of LTD units.

4. summary

Due to increased speed of semi-conductor switches and improvements in high frequency characteristics for the pulse core, high voltage pulsed power supplies will increasingly be usable as solid-state systems.

Additionally, the devices will become more suitable for many kinds of industrial applications, thanks to digitalization and modularization.

As SiC devices develop, we can expect that they will become smaller in size, resulting in the creation of new industrial applications.

References

1) Ken Takayama, Kunio Koseki, Kota Torikai, Akira Tokuchi, Eiji Nakamura, Yoshio Arakida, Yoshito Shimosaki, Masayoshi Wake, Tadaaki Kouno, Kazuhiko Horioka, Susumu Igarashi, Taiki Iwashita, Atsushi Kawasaki, Jun-ichi Kishiro, Makoto Sakuda, Hikaru Sato, Makoto Shiho, Masashi Shirakata, Tsuyoshi Sueno, Takeshi Toyama, Masao Watanabe, and Isao Yamane,"Observation of the acceleration of a single bunch by using the induction device in the KEK proton synchrotron",Phys. Rev. Lett. 94, 144801 (2005).
2) A. Kawasaki, T. Aoki, A. Tokuchi, T. Shintake, T. Inagaki, H. Takebe, C. Kondo, “Development of High Voltage Capacitor Charger for XFEL/SPring-8", Proc. the 5th Annual Meeting of Particle Accelerator Society of Japan and the 33rd Linear Accelerator Meeting in Japan(Aug 6-8, 2008, Higashihiroshima, Japan)
3) Anne Van Arsdall, "PULSED POWER at Sandia National Laboratories the first forty years", Sandia National Laboratories,(2008).
4) W. A. Stygar, M. E. Cuneo, D. I. Headley, H. C. Ives, R. J. Leeper, M. G. Mazarakis, C. L. Olson, J. L. Porter, T. C. Wagoner and J. R. Woodworth, "Architecture of petawatt-class z-pinch accelerators", PHYSICAL REVIEW SPECIAL TOPICS - ACCELERATORS AND BEAMS 10, 030401 (2007)

DEVELOPMENT OF GATE DRIVE CIRCUIT FOR SILICON CARBIDE JUNCTION FIELD-EFFECT TRANSISTOR

K. Ise[a], H. Tanaka[a], K. Takahashi[a], K. Takaki[a],
M. Wake[b], K. Okamura[b], K. Takayama[b]

[a]Iwate University, 4-3-5 Ueda, Morioka, Iwate 020-8551, JAPAN
[b]High Energy Accelerator Research Organization (KEK), KEK Accelerator Lab, 1-1 Oho, Tsukuba-city, Ibaraki-prefecture, Japan

ABSTRACT

A gate circuit was developed for continuous drive of a silicon carbide(SiC) junction eld-e ect transistor(JFET) and the switching characteristics of the SiC-JFET were investigated experimentally. The results showed that the turn-on and the turn-o times of the gate-source voltage of the SiC-JFET were 15 and 14 ns, respectively. The SiC-JFET operated with gate-source voltage of 1 kV, drain current of 50 A and repetitive operation of 1 MHz driven by the developed gate circuit. The turn-on and the turn-o times of the drain-source voltage of the SiC-JFET were obtained to be 81 ns and 8 ns, respectively. The gate capacitance, the on-resistance of the drain-source and the switching loss were obtained to be 8.2 nF, 100 mΩ and 0.9 mJ/pulse, respectively.

I. Intrtoduction

Pulsed power generators are used in many industrial applications and most of these generators use semiconductor switches in order to achieve high repetition rate, long life-time and high e ciency [1,2]. Especially generation of high voltage pulse at high repetition rate is required by pulse modulator for an induction synchrotron(IS) [3–5]. The idea is to overcome shortcomings of the conventional Radio Frequency(RF) synchrotron, in particular the limited longitudinal phase space available for the acceleration of charged particles - in other words the distribution in energy and position around the ring of the accelerated particles. Instead of short RF bunches, extremely long bunches, called "super-bunches", can be captured and accelerated in the IS. The super-bunch con ned in the longitudinal direction by a pair of pulsed barrier voltages is accelerated with long induction voltages, as conceptually shown in Fig. 1. In this concept, the acceleration of a high-intensity beam is achieved by means of an e ective utilization of the longitudinal phase space, which is not available in a conventional RF synchrotron. Furthermore the luminosity is estimated to be at least 20 times higher than that in hadron colliders, based on conventional RF technology and all ions, including cluster ions in their possible and arbitrary charge state, are accelerated in the IS[6,7].

A switching generator that generates bipolar pulse is in one of key technologies for the IS. A present solid-state pulsed power modulator for the IS are composed of a full bridge circuit of Metal-Oxide Semiconductor Field-E ect Transistors(MOSFETs). The circuit

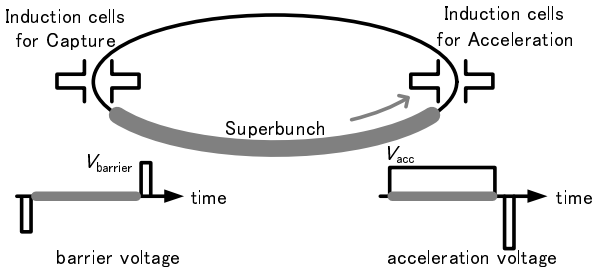

Fig. 1 Conceptual schematic of super-bunch acceleration.

schematic is shown in Fig. 2. The circuit generates an output pulse voltage of about 2 kV and a peak current of 17 A [8–10]. However there are several problems with the circuit. First the control of the switching generator is complex because the switching arm consists of 7 MOSFET devices connected in series. Moreover the applied voltage to the switching arms is distributed to the seven MOSFET devices in unbalance owing to the output capacitance of the devices. This unbalance voltage distribution reduces the capable operation voltage [8]. Second the modulator size and weight are limited to be large at large number of MOSFET devices connected in series. Furthermore the system maintenance and reliability are also serious issues to be improved [11]. In order to overcome these problems, a new switching generator based on silicon carbide(SiC) devices is one of the promising candidates because the electrical and the material properties of SiC power devices show higher performance than those of silicon(Si)

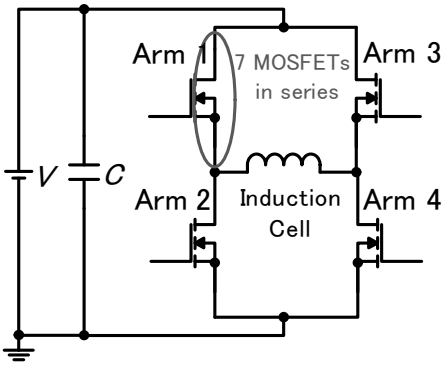

Fig. 2 Circuit of the switching generator.

based devices [5,12].

The SiC power semiconductors are characterized by outstanding performance concerning their voltage blocking capability, voltage drop at on-state, switching time and thermal resistance[13]. The conduction and switching losses could be reduced and the capability of operating temperature could be signi cantly increased compared to Si devices[14].

In this paper, the behavior of the gate drive circuit developed for a SiC junction eld-e ect transistor(SiC-JFET) is described and the switching characteristics of the SiC-JFET were investigated using the developed gate circuit experimentally.

II. Static Characteristic of the SiC-JFET

Photograph and a schematic internal circuit of the SiC-Cascode module used in the present experiment are shown in Figs. 3 and 4, respectively. The SiC-Cascode module is manufactured by SiCED Electronics Development GmbH. The module consists a SiC-JFET and a low voltage Si-MOSFET connected in series. The rating voltage and current of the SiC-JFET are 1200 V and 50 A, respectively. In this experiment, the gate and the source terminals of the Si-MOSFET are shorten to keep same potential to measure the characteristics of the SiC-JFET only.

The SiC-JFET is normally-on device that requires a negative gate voltage to turn o . In addition it is known that the variation of threshold voltage for each SiC-JFET devices is existed to be large[13]. Therefore the static characteristic of the SiC-JFET was measured at rst. The circuit for the measurement of the

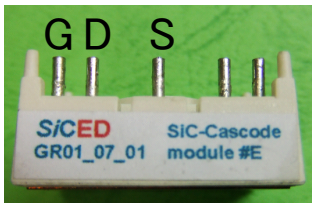

Fig. 3 Photograph of the SiC-Cascode module used in the experiment(G: gate, D: drain, S: source of SiC-JFET).

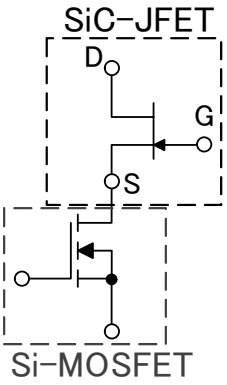

Fig. 4 Schematic internal circuit of the SiC-Cascode module.

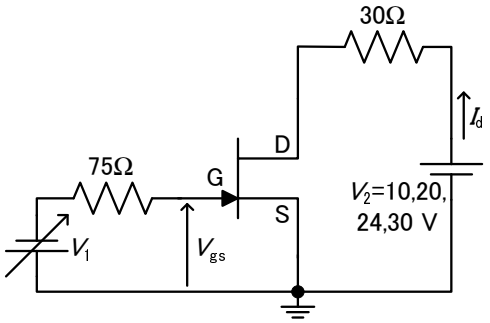

Fig. 5 Circuit for the measurement of the static characteristic of the SiC-JFET.

static characteristic of the SiC-JFET is shown in Fig. 5. The power supply V_1 was changed in range from 0 to -24 V at power supply V_2 of 10, 20, 24, 30 V as parameter.

Fig. 6 shows the drain-source current I_d as a function of gate-source voltage V_{gs} for various applied voltages V_2. The whole region can be separated to three parts. The saturation current region shows almost constant drain-source current determined with V_2 divided by 30 Ω and is in range from 0 to -10 V of the gate-source voltage V_{gs}. In the linear region, the drain-source current I_d decreases exponentially with decreasing gate-source voltage V_{gs} with independent of voltage V_2. This region is in range from -10 to -12.5 V of gate-source voltage V_{gs}. In the threshold region, the drain-source current I_d is almost interrupted by the negative bias when the gate-source voltage is lower than -12.5 V. Based on this result, we chose the gate-source voltage of -20 V as negative bias voltage when the SiC-JFET was controlled to be o -state to avoid mis-switching.

III. Gate Circuit

A conventional gate circuit of the SiC-JFET is shown in Fig. 7. When the MOSFET is turned on by applying pulse voltage as gate signal of the MOSFET(DE475-501N44A), the SiC-JFET is also turned on. This gate circuit is suitable to drive a

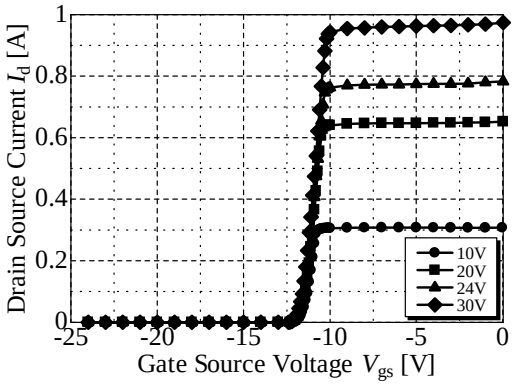

Fig. 6 Static characteristic of the SiC-JFET.

switching device in burst mode because fast recovery time can be realize by reducing RC delay with decreasing R_g value. However there are several problems with the gate circuit in the continuous wave mode because the gate resistor R_g is heated with circuit current. Moreover a large current capacity is required for the power supply V_{dc} to charge-up capacitance of the MOSFET and the gate-source capacitance of the SiC-JFET in short time through the resistor R_g. The measured thermography image of R_g using the conventional gate circuit at repetition rate of 10 kHz and pulse width of 500 ns is shown in Fig. 8. The value of R_g is 5 Ω and the power rating of R_g is 80 W. The temperature of R_g rises to be about 180 degrees because R_g is heated-up with large current determined as V_{dc}/R_g during turned-on time of the SiC-JFET devices.

To solve these problems, the gate circuit of the SiC-JFET was improved as shown in Fig. 9. The value of R_g is chosen to be larger than 100 Ω to reduce gate current. Moreover MOSFET S_2 is connected to R_g in parallel. The MOSFET S_1 and S_2 are switched in opposite phases, i.e. S_1 is switched o while S_2 is switched on to be worked as short-circuit of R_g. The turn-o time is reduced by shorting the resistor R_g.

The waveforms of V_{gs} are shown in Fig. 10 for three di erent R_g values; 100, 470 Ω and 1 kΩ. S_2 is always kept as o -state, i.e. the circuit is equivalent to the conventional gate circuit with R_g of 100, 470 Ω or 1 kΩ as shown in Fig. 7. The gate signal of S_1 is applied to the gate with 5 times at repetition rate of 1 MHz

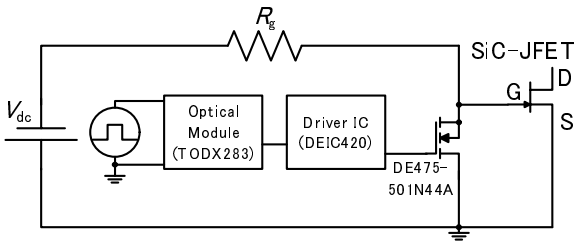

Fig. 7 Conventional gate circuit of the SiC-JFET.

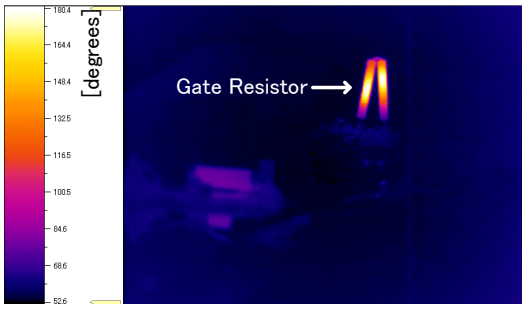

Fig. 8 Measured thermography of the conventional gate circuit.

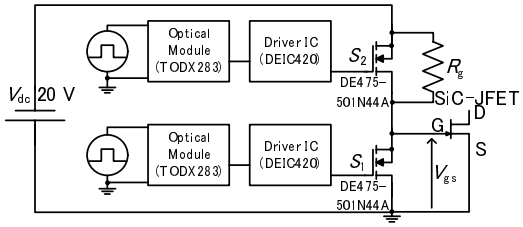

Fig. 9 Developed gate circuit of the SiC-JFET.

and pulse width of 500 ns. The each waveforms shown in Fig. 10 shows one pulse and the pulse duration is in range between 5 and 10 s. While the turn-on time is almost constant, the turn-o time depends on R_g because the charge-up time of the output capacitance of the MOSFET S_1 and the gate-source capacitance of the SiC-JFET depend on resistance of R_g. The four spikes of the voltage drop from 0 to -7 V are observed within 5 s at 100 Ω of R_g case. These spikes mean turn-o operation of the MOSFET S_1. However, the 500 ns time duration of o -state of the MOSFET is much smaller than time duration for charging-up the capacitance of MOSFET and of the SiC-JFET. Further the gate-source capacitance of the SiC-JFET can be calculated using time constant of the turn-o region. The capacitance is calculated to be 8.2 nF by time constant of the CR charging.

The waveforms of V_{gs} are shown in Fig. 11 for three di erent R_g values; 100, 470 Ω and 1 kΩ. The con-

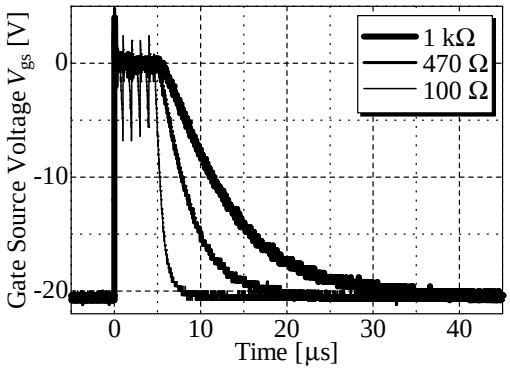

Fig. 10 Waveforms of gate-source voltage at S_2 of o -state.

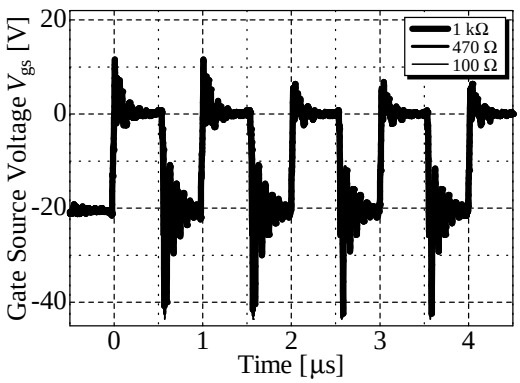

Fig. 11 Waveform of gate-source voltage of S_2 and its reversed operation of S_1.

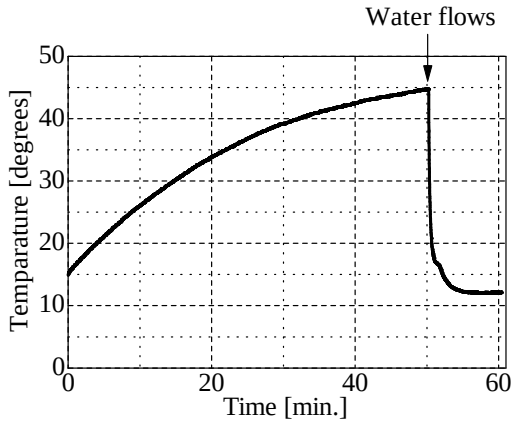

Fig. 12 Temperature change of MOSFET S_1 surface during switching operation..

ditions are that S_2 is switched in opposite phase with respect to S_1 as shown in Fig. 9. The gate signal of S_1 is the repetition of 5 times, the repetition rate of 1 MHz and the pulse width of 500 ns. The turn-on and turn-o times were obtained to be 15 and 14 ns, respectively and these times are almost independent of R_g. It is con rmed from Figs. 10 and 11 that the turn-o time can be reduced using the newly developed gate circuit shown in Fig. 9 instead of the conventional gate circuit shown in Fig. 7.

The surface temperature of S_1 is monitored in continuous wave mode using the developed gate circuit and is shown in Fig. 12. A water cooling system, i.e. heat sink, is employed to reduce temperature of S_1. First the heat sink on S_1 is not cooled by water at time from 0 to 50 minutes. The temperature rises gradually and starts to saturate around 50 degrees without water cooling. After the time 50 minutes the heat sink started to be cooled by owing the water and the temperature decreases to be about 12 degrees. This temperature of 12 degrees is much smaller the critical value of 150 degrees for the junction of the MOSFET used as S_1[15]. This result indicates that the continuous operation with high repetition rate larger than 1MHz can be realized using the water cooling system. Therefore the present gate circuit with the water cooling system has potential to be reduce the size of the synchrotron limited by the pulse repetition rate. This technique can contribute to the progress of applications of the accelerator, e.g. medical applications.

Fig. 13 shows the circuit for measurement of the on-state resistance R_{on} between the drain and the source of the SiC-JFET. In general, it is di cult to obtain the drain-source voltage V_{ds} at on-state of the SiC-JFET because the voltage changes from 1kV to several volts during short time; several tens nanoseconds. To overcome this di culty, a zener diode is used to cramp up the monitoring voltage to zener voltage at o -state of SiC-JFET and is connected SiC-JFET as shown in Fig. 13. While SiC-JFET is o -state, the voltage between the zener diode V_{dz} is xed to be zener voltage of 10 V. On the other hand, V_{dz} shows the drain-source voltage at on-state of the SiC-JFET because V_{ds} is much smaller than 10 V of the zener voltage. The voltage is approximately equal to the on-state voltage of the SiC-JFET because the almost current ow through the SiC-JFET and little current ow into the zener diode. R_{on} is calculated to divide V_{dz} by I_d and is determined to be shown in Fig. 14. R_{on} is in range from 50 to 100 mΩ and is slightly change by time.

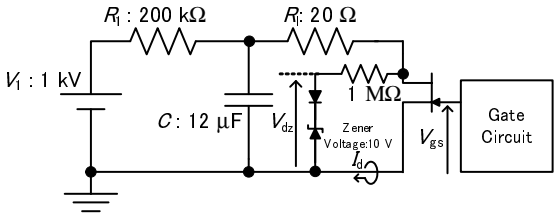

Fig. 13 Circuit for measurment of on-state resistance of SiC-JFET.

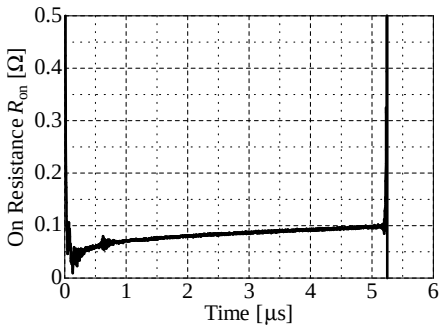

Fig. 14 Temporal change of the on-state resistance of the SiC-JFET.

IV. Switching operation of the SiC-JFET

Fig. 15 shows the experimental circuit for repetitive switching operation for the SiC-JFET. The gate circuit shown in Fig. 15 consists of two MOSFET switching devices as shown in Fig. 9. The storage capacitor C is charged up to 1 kV by the dc power supply V_1. V_{ds} and the drain current I_d are measured

for two di erent values of the current damping resistor R_l.

The results are shown in Fig. 16 for 56 Ω resistance and Fig. 17 for 20 Ω resistance, respectively. The gate drive pulse is applied to the gate terminal of the SiC-JFET with repetition rate of 1 MHz. From Figs. 16 and 17, the switching is successfully operated at 1 MHz repetition rate and the pulse widths are also controlled to be about 500 ns at both resistance cases. In o -state of the SiC-JFET, the voltage V_{ds} is almost 1 kV and the current I_d is inhibited for both resistance cases. In on-state of the SiC-JFET, the voltage V_{ds} is almost zero and the current I_d is controlled to be 50 and 17 A for the resistance of 20 and 56 Ω, respectively. The turn-on times of the SiC-JFET are 81 and 17 ns for the resistance of 20 and 56 Ω, respectively. The turn-o times are 8 and 31 ns, respectively.

The total energy losses at R_g of 20 and 56 Ω are shown in Figs. 18 and 19, respectively. The switching losses are obtained to be 0.9 and 0.19 mJ/pulse at R_g of 20 and 56 Ω, respectively. The almost energy loss is caused in the turn-o and the turn-on phases.

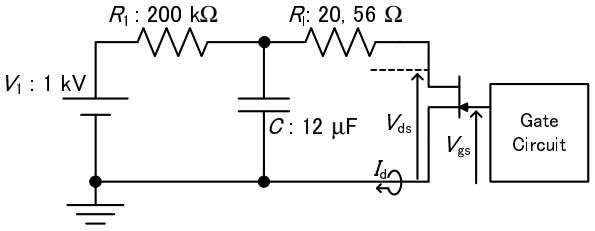

Fig. 15 Circuit for the measurement of the SiC-JFET switching characteristics.

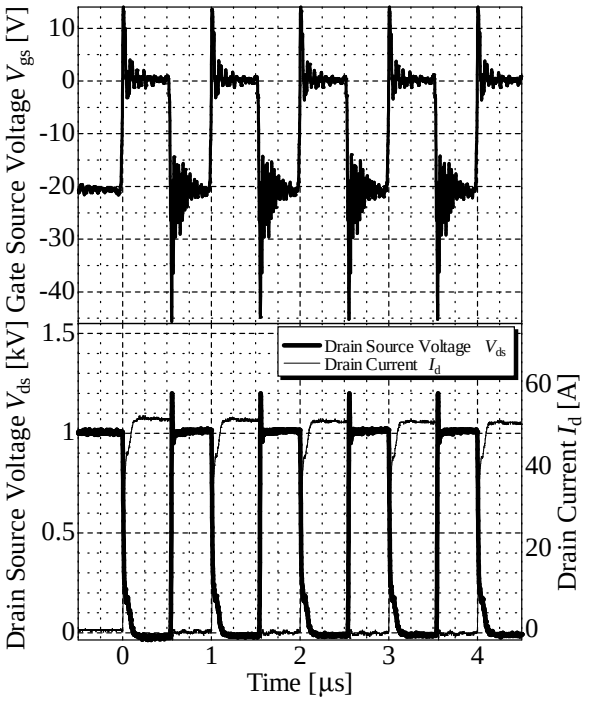

Fig. 16 Switching characteristics at R_l of 20 Ω .

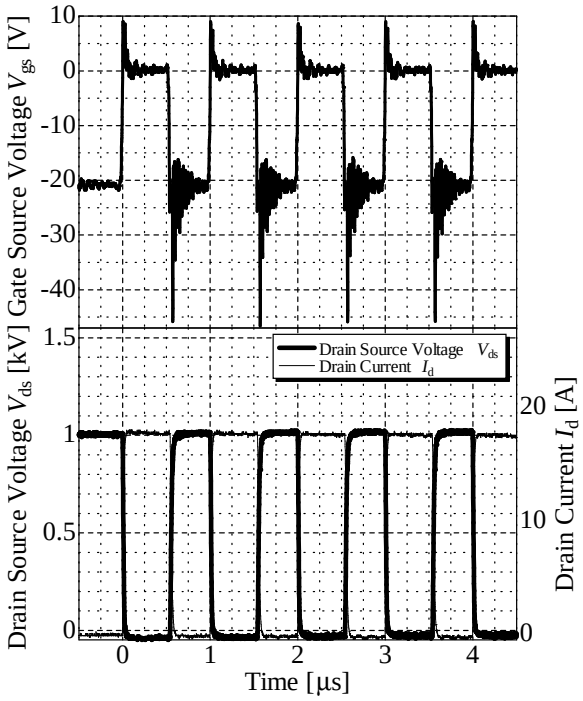

Fig. 17 Switching characteristics at R_l of 56 Ω.

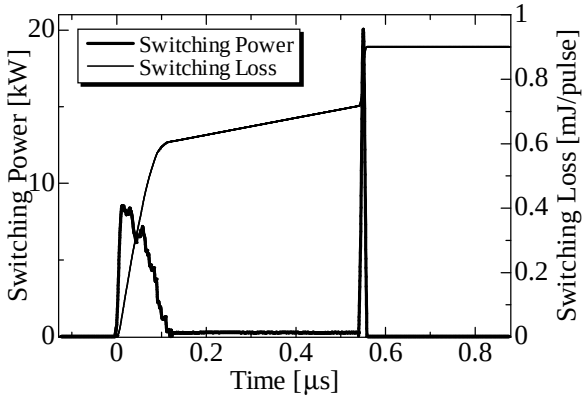

Fig. 18 Waveforms of calculated switching power and switching loss at R_l of 20 Ω.

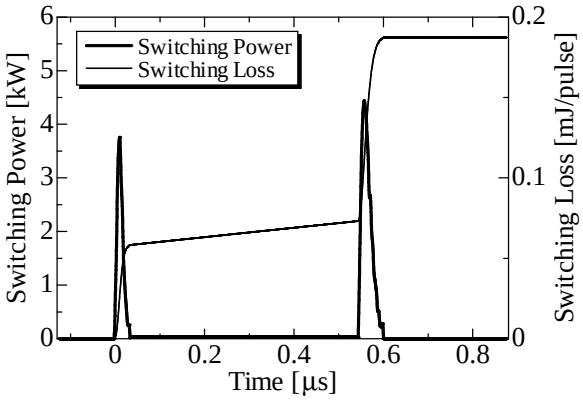

Fig. 19 Waveforms of calculated switching power and switching loss at R_l of 56 Ω.

V. Conclusions

The gate circuit of the SiC-JFET is developed for the operation in continuous wave mode with repetition rate of 1 MHz. The turn-on and turn-o times of V_{gs} were obtained to be 15 and 14 ns, respectively.

The switching characteristics of the SiC-JFET was measured using the developed the gate circuit. At the repetition rate of 1 MHz and V_{ds} of 1 kV and R_l of 20 Ω, the turn-on time of 81 ns, turn-o time of 8 ns and the switching loss of 0.9 mJ/pulse were obtained. In case of R_l of 56 Ω, the turn-on time of 17 ns, turn-o time of 81 ns and the switching loss of 0.19 mJ/pulse were obtained. Furthermore the value of R_{on} and the gate-source capacitance were obtained to be 100 mΩ and 8.2 nF, respectively.

References

(1) W. Jiang and K. Yatsui, "Compact Pulsed Power Generators for Industrial Applications", IEEJ Trans. FM, Vol.124, No.6, pp.451-455(2004).

(2) K. Horioka and W. Jiang, "Recent Progress in Pulse Power Technology and its Applications", IEEJ Trans. FM, Vol.127, No.11 pp.669-674(2007).

(3) K. Takayama and J. Kishiro, "Induction synchrotron", Nucl. Instr. and Meth. A, Vol.451, pp.304-317(2000).

(4) K. Takayama, K. Torikai, Y. Shimosaki, T. Kono, T. Iwashita, Y. Arakida, E. Nakamura, M. Shirakata, T. Sueno, M. Wake and K. Otsuka, "Experimental demonstration of the KEK induction synchrotron", Nucl. Instr. and Meth. A,Vol.577, pp.191-196(2007).

(5) K. Takayama, Y. Arakida, T. Dixit, T. Iwashita, T. Kono, E. Nakamura, K. Otsuka, Y. Shimosaki, K. Torikai and M. Wake, "Experimental Demonstration of the Induction Synchrotron", Phys. Rev. Lett., Vol.98, pp.054801(1)-054801(4)(2007).

(6) K. Takayama, J. Kishiro, M. Sakuda, Y. Shimosaki and M. Wake, "Superbunch Hadron Colliders", Phys. Rev. Lett., Vol.88, No.14, pp.144801(1)-144801(4)(2002).

(7) K. Takayama, Y. Arakida, T. Iwashita, Y. Shimosaki, T. Dixit and K. Torikai, "All-ion accelerators: An injector-free synchrotron", J. Appl. Phys., Vol.101, pp.063304(1)-063304(7)(2007).

(8) K. Koseki, M. Wake and K. Takayama, "Signi cance of isolation impedance in a solid-state power modulator", Nucl. Instr. and Meth. A, Vol.554, pp.64-74(2005).

(9) K. Koseki and Y. Shimosaki, "Parasitic resonance in a solid-state pulsed power modulator", Nucl. Instr. and Meth. A, Vol.556, pp.24-30(2006).

(10) M. Wake, Y. Arakida, K. Koseki, Y. Shimosaki, K. Takayama, K. Torikai, W. Jiang, K. Nakahiro, A. Tokuchi and A. Sugiyama, "Switching power supply for induction accelerators", Proceedings of PAC07, Albuquerque, New Mexico, USA, MOPAN042, pp.251-253(2007).

(11) W. Jiang, N. Oshima, T. Yokoo, K. Nakahiro, H. Honma, K. Takayama, M. Wake and N. Shimizu, "Repetitive pulsed power based on semiconductor switching devices", Pulsed Power Conference, 2007 16th IEEE International, Vol.1, pp.550-552(2007).

(12) M. Bhatnagar and B. J. Baliga, "Comparison of 6H-SiC, 3C-SiC, and Si for Power Devices", IEEE Trans. Electron Devices, Vol.40, No.3, pp.645-655(1993).

(13) S. Round, M. Heldwein, J. Kolar, I. Hofsajer and P. Friedrichs, "A SiC JFET driver for a 5 kW, 150 kHz three-phase PWM converter", Industry Applications Conference, 2005. Fourtieth IAS Annual Meeting. Conference Record of the 2005, Vol.1, pp.410-416(2005).

(14) K. Mino, S. Herold and J. W. Kolar, " A gate drive circuit for silicon carbide JFET", Industrial Electronics Society, 2003. IECON '03. The 29th Annual Conference of the IEEE, Vol.2, pp.1162-1166(2003)

(15) "DE475-501N44A", http://www.ixysrf.com/pdf /switch_mode/de475_501n44a.pdf.

FUNDEMENTAL EXPERIMENTS OF TRIBOLUMINESCENCE BY PEELING TAPES

Yuki ARAI and Seizo FURUYA

Faculty of Education, Gunma University, Maebashi 371-8510 JAPAN

ABSTRACT

Triboluminescence is a luminous phenomenon resulted from friction; for example, peeling scotch tape, breaking rock sugar with a hammer, peeling mica and so on. Triboluminescence is well known over 50 years but last year UCLA group reported the radiation of x-ray region by triboluminescence in vacuum for the first time. UCLA group made an automatic machine which peels scotch tape. With a view to practical application of triboluminescence to roentgen diagnosis we made an automatic peeling machine similar to that of UCLA group. Replacing conventional x-ray tube with triboluminescence is very useful to roentgen diagnosis. First, we made a spectroscopic analysis of visible light from triboluminescence when the parameters such as the followings are changed; peeling speed, atmospheric pressure, variety of scotch tape, emission angle etc. Then in a similar way we measured x-ray dose from triboluminescence using a potable dosemeter.

I. Introduction

Triboluminescence is a luminous phenomenon resulted from friction; for example, peeling scotch tape, breaking rock sugar with a hammer, peeling mica and so on. Triboluminescence is well known over 50 years but last year UCLA group reported the radiation of x-ray region by triboluminescence in vacuum for the first time.[1)] UCLA group made an automatic machine which peels scotch tape. With a view to practical application of triboluminescence to roentgen diagnosis we made an automatic peeling machine similar to that of UCLA group. An x-ray tube for conventional roentgen diagnosis needs a high voltage power supply. In contrast, triboluminescence does not need it. So it is very useful for roentgen diagnosis to replace a conventional x-ray tube with triboluminescence. First, we have attempted to make a spectroscopic analysis of visible light from triboluminescence when the parameters such as the followings are changed; peeling speed, atmospheric pressure, variety of scotch tape, emission angle etc. Then in a similar way we have attempted to measure x-ray dose from triboluminescence using a potable dosemeter.

II. Experimental setup

We made an automatic peeling machine similar to that of UCLA group. Fig. 1 shows a photograph of the machine. A geared motor of 200 RPM is used for a driving force.

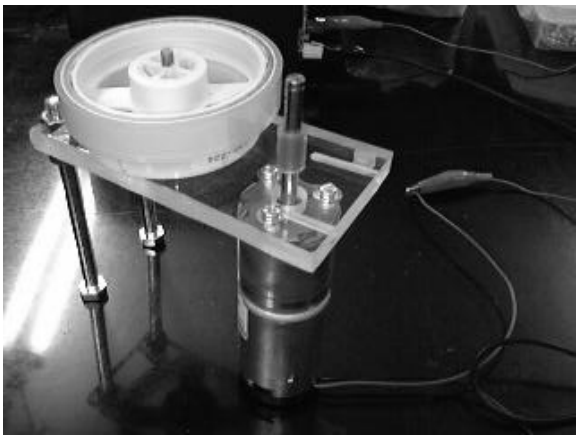

Figure 1 Photograph of automatic peeling machine

Fig. 2 shows the vacuum pump system. A turbo molecular pump (TMP) and a rotary pump (RP1) are a pair (PFEIFFER VACUUM, Turbomolecular Drag Pumping Station TSH261 with DUO2.5). The pumping speed of RP1 is 2.5 m^3/h and total pumping speed is 210 L/s. To enhance the pumping capability RP2 (SHINKU KIKO, GVD-135A, 135 L/m) is added.

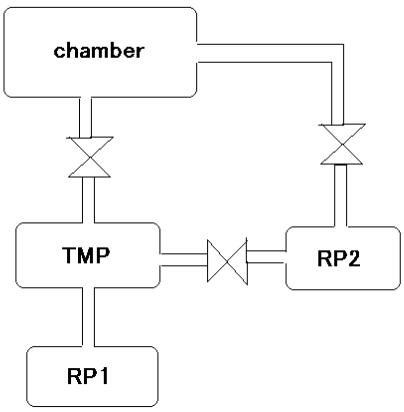

Figure 2 Vacuum pump system

Fig. 3 shows a photograph of the vacuum chamber. The inner diameter is 210.7 mm and the inner height is 200 mm.

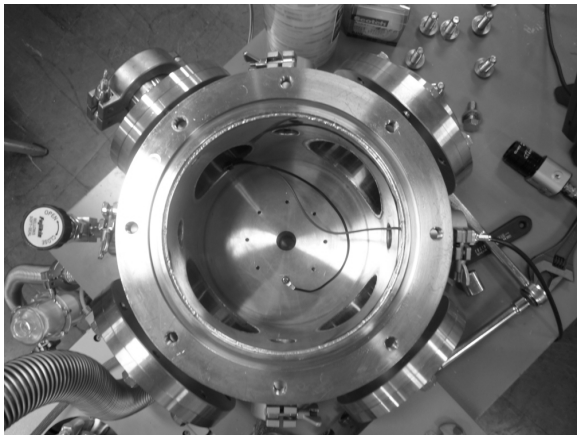

Figure 3 Photograph of vacuum chamber

Two kinds of Scotch tapes are prepared in our experiments, as shown in Fig. 4. One is a large-diameter tape. Another is a small-diameter tape. By degassing the tapes beforehand the vacuum chamber can be evacuated quickly. As for the large-diameter tape, the core is made from paper, so the core shrinks in the vacuum chamber. As a result, as shown in Fig. 5, a space is produced between the core and the tape, and this leads to a non-uniform peeling. As for the small-diameter one, the core is made of plastic, so such a phenomenon does not occur. Therefore, small-diameter tapes are used in this paper.

Figure 4 Photograph of two kinds of tapes

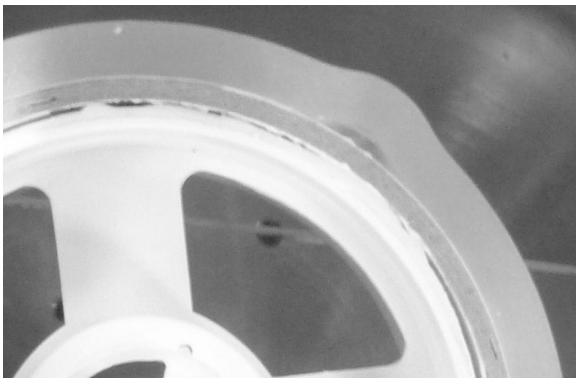

Figure 5 Photograph of distorted tape

III. Experimental results

We started to peel the tape after the vacuum chamber was evacuated to $3*10^{-3}$ torr. The peeling speed was 0.6-1.2 cm/s. First, we confirmed the emission of visible light from peeling tape by the naked eye. Then open-shatter photographs were taken. Fig. 6 shows an open-shutter photograph of emission of visible light from peeling tape in vacuum. It is clear that the peeling tape emits bluish white light. A thin piece of plastic scintillator (OKEN, NE102A) was put near the peeling tape. It emits visible light when irradiated with x-ray. It is very difficult to see but it is found that the edge of scintillator emits light. The plastic scintillator has a characteristic that its edge produces luminescence well. Fig. 6 was taken only by turning off a room light and Fig. 7 was taken by covering the vacuum chamber overall with a blackout curtain. It is clear from the photograph that the edge of plastic scintillator emits light.

Soon after peeling the tape, the pressure in the chamber started to increase. When the pressure was more than $7*10^{-3}$ torr, the plastic scintillator did not

emit light. As the peeling speed was increased, the intensity of visible light from peeling tape also increased. However, as the peeling speed was increased, the pressure also increased. That is the reason why the peeling speed in our experiments was 0.6-1.2 cm/s, slower than 3 cm/s of UCLA group, and why we added an additional rotary pump RP2 to the vacuum system. Above all, we could not control the pressure in the vacuum chamber.

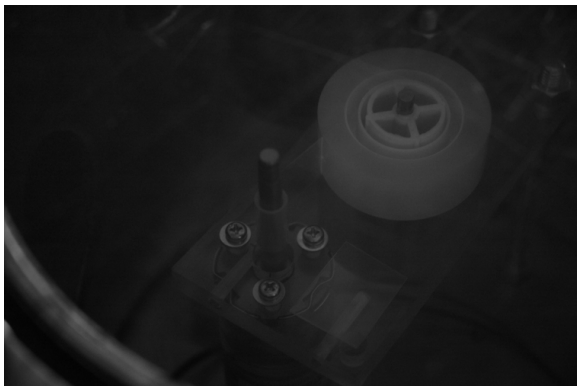

Figure 6 Photograph of light emission from peeling tape

Figure 7 Photograph of emission from scintillator

Next, we have attempted to measure the time variation of visible light emission from peeling tape using a photomultiplier. The visible light was led to a photomultiplier (Hamamatsu Photonics, R446) using optical fiber, as shown in Fig. 8. Fig. 9 shows the time variation of visible light emission from peeling tape. Although the signal includes some noises, we managed to obtain the signal. The visible light emission from peeling tape seems continuous by the naked eye but peeling tape emits light in pulses actually. We have also attempted to measure the pulse width but gave it up because it was difficult to distinguish a true signal from a noise. Then we have attempted to measure the visible light emission only from the plastic scintillator. To cut the visible light from peeling tape a slip of black paper was put on the scintillator, as shown in Fig. 10, but we were not able to confirm the light emission from the plastic scintillator.

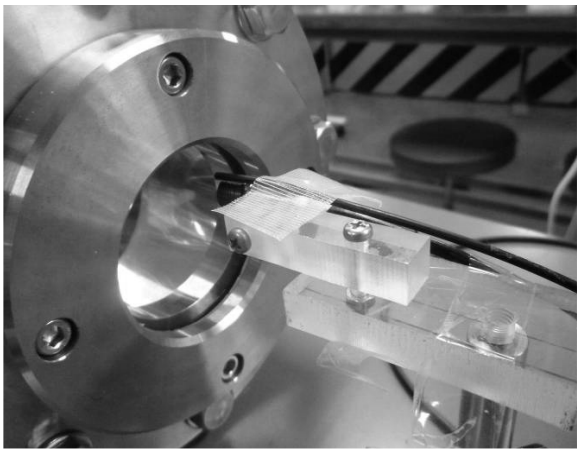

Figure 8 Optical fiber for measuring visible light

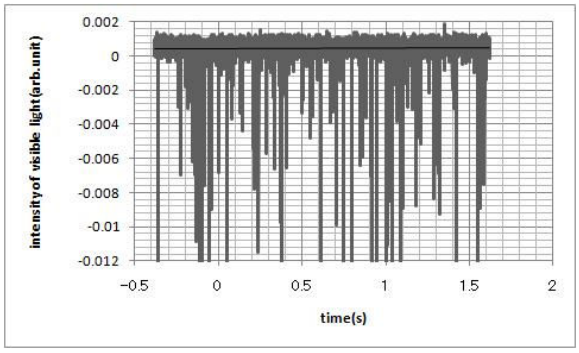

Figure 9 Time variation of visible light emission

Thirdly, we have attempted to measure the spectrum of visible light emitted from the peeling tape. However, we could not obtain the spectrum because the emitted light was very weak. It is necessary to set up a light collection optical system using mirrors and lens.

Finally, we have attempted to measure x-ray dose from peeling tape using a potable dosemeter. Fig. 11 shows a photograph of dosemeter. The dosemeter (ALOKA, PDM-117) was set on the vacuum chamber but it did not react.

IV. Conclusions

We have made an automatic peeling machine similar to that of UCLA group and have confirmed the visible light and x-ray emissions from the

peeling tape. The visible light emission from peeling tape seems continuous by the naked eye but we have verified using a photomultiplier that the peeling tape emits light in pulses actually.

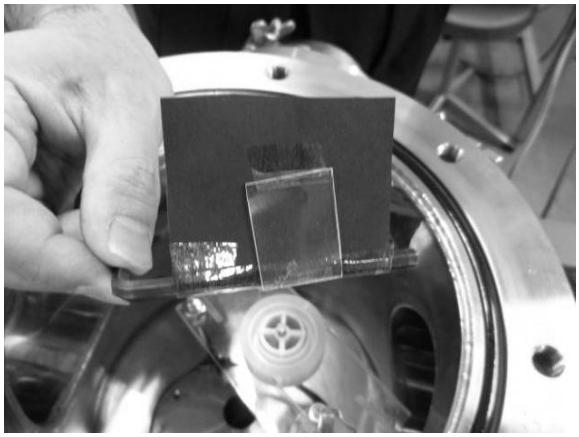

Figure 10 Black paper to cut visible light from tape

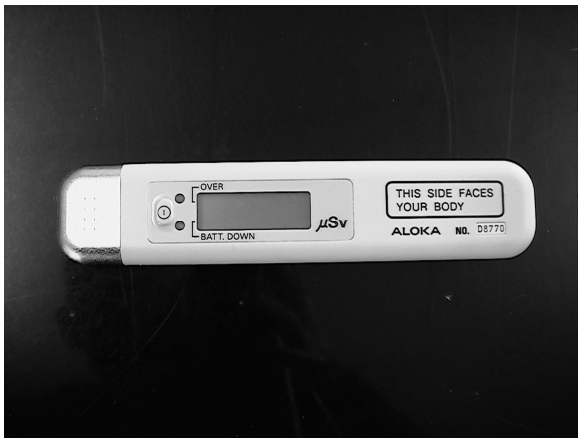

Figure 11 Photograph of portable dosemeter

Acknowledgements

We cordially thank Professor Shozo ISHII and Mr Shinji IBUKA of Tokyo Tech for their ungrudging support to our experiments.

References

1) C.G.Camara, J.V.Escobar, J.R.Hird and S.J.Putterman, “Correlation between nanosecond X-ray flashes and stick–slip friction in peeling tape”, nature, **455**, 1089-1092 (2008).

BRAGG RESONATOR FOR FREE ELECTRON MASER USING AN INTENSE RELATIVISTIC ELECTRON BEAM

Fumichika Kondo, Kota Nose, Ken Misawa, Shoko Yanagi,
Yukihiro Soga, Keiichi Kamada and Naum S. Ginzburg [a)]

Graduate School of Science and Technology, Kanazawa University,
Kanazawa, Ishikawa, 920-1192, JAPAN
[a)]Institute of Applied Physics, Russian Academy of Sciences, Nizhny Novgorod,
603600, Russia

ABSTRACT

A new scheme of Bragg resonator for an intense terahertz electromagnetic wave source using an intense relativistic electron beam was proposed. A hybrid Bragg resonator using an advanced and a traditional Bragg reflectors is expected to have an advantage on the frequency selectivity to a normal Bragg resonator using two traditional Bragg reflectors. About the reflectivity of an advanced and a traditional Bragg reflectors, the results of simulations and cold tests showed good agreements. Preliminary experimental results of FEM using both resonators were presented.

I. Introduction

Because of the lack of appropriate radiation sources, the frequency range of 0.1-10 THz is called THz gap. The THz gap lies between the upper frequency of classical electromagnetism (electron tubes) and the lower frequency of quantum electronics (LASER). Among many types of THz sources, electron tubes are expected to realize convenient THz sources, i.e., compact size, DC operation with output power over 1W [1-3].

Gyrotron is the most developed electron tube for THz source. The selectivity of the frequency is excellent because the quasi-cutoff frequency was used. As the radiated frequency of Gyrotoron depends on the strength of the magnetic field, over 20 T magnetic field is necessary for THz radiation. New ideas for THz Gyrotoron using lower strength of the magnetic field, for example large orbit gyrotron (LOG) etc., are now strongly developed [4].

One of the other candidates of THz source among electron tubes is a free electron maser (FEM). An intense relativistic electron beam (IREB) whose output power is over 1 GW is used for an energy source of an intense FEM. However, because of its strong self electric field, one of the problems for the intense FEM is the wide frequency spectrum. So that a normal Bragg resonator is utilized. In a normal Bragg resonator, traditional Bragg reflectors works as mirrors in the optical distributed feedback LASER (Fig.1)[5,6]. Many successful results of narrow band FEM are obtained by using the traditional Bragg reflector or resonators in mm waveband [7,8]. However, as the frequency

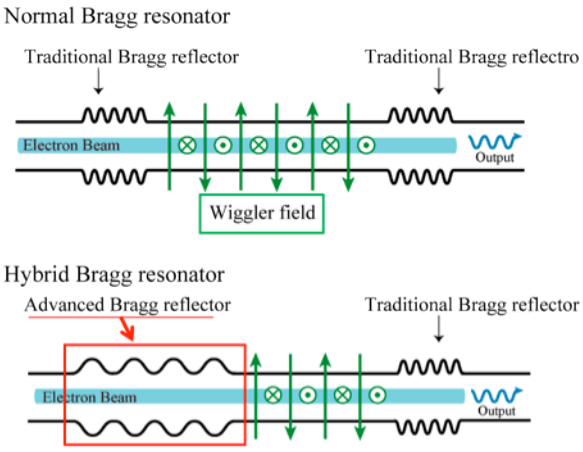

Fig. 1. Schematics of the Normal Bragg Resonator (upper) and the hybrid Bragg resonator.(lower). An IREB is injected from left side.

increases, the traditional Bragg reflector loses the selective features over transverse indexes. An advanced Bragg reflector was proposed by Ginzburg [9]. It utilizes the interaction between a propagating wave and a quasi-cutoff mode to provide a higher selectivity over the transverse index than a normal Bragg reflector. Structural difference between the traditional and the advanced reflectors is mainly on the periodic length of the corrugation. While the corrugated period length of a traditional Bragg reflector is a half of the guide wavelength, that of an advanced Bragg reflector is nearly equal to it. The words "reflector" and "resonator" are indicated in Fig. 1. In the hybrid Bragg resonator, an advanced Bragg reflector is used at the entrance side and at the exit side the traditional Bragg reflector is utilized.

The goal of our experiment is to clear the advantage of the newly proposed hybrid Bragg resonator. In this paper, we report the preliminary experimental results of FEM radiation and the results of cold tests of a normal and an advanced Bragg reflectors.

2. Experimental setup.

In Fig. 2, the schematic of the experimental setup is shown. An intense relativistic electron beam (IREB) with energy of around 700keV, current of around 200 A and the radius of 3 mm was injected into the drift tube with diameter of 20mm. As a liquid resister was set parallel to the diode as a shunt register to prevent the output impedance for the pulse line from decrease in time, the diode voltage was kept constant during 120 ns. The energy spread of the IREB was measured to be 720 ± 22 keV by a magnetic momentum analyzer. Axial magnet field (Bg) with strength of up to 1T was applied by two solenoid coils.

A helical wiggler coil located inside a solenoid coil provided a periodic radial magnetic field (Bh) up to 0.15 T. The axial positions of the strengths of the axial and radial magnetic field are shown in Fig. 2. The IREB was diverged to the wall at the exit of the axial magnetic field.

A horn antenna was set just behind the acrylic window to observe the radiated electromagnetic wave. The electromagnetic wave was detected through 3 band pass filters, with frequency of 26-31, 30.5-35.7 and 35.5-40 GHz, and a high pass filter over 40 GHz was used to detect the higher frequency. Four attenuators were set at each branch. We carried out FEM experiments using two normal Bragg resonators with frequencies of 54 GHz and 40 GHz. When the FEL radiation with the frequencies of 54 GHz was expected, simple high pass filters made by metal disks with various diameter holes at the center were

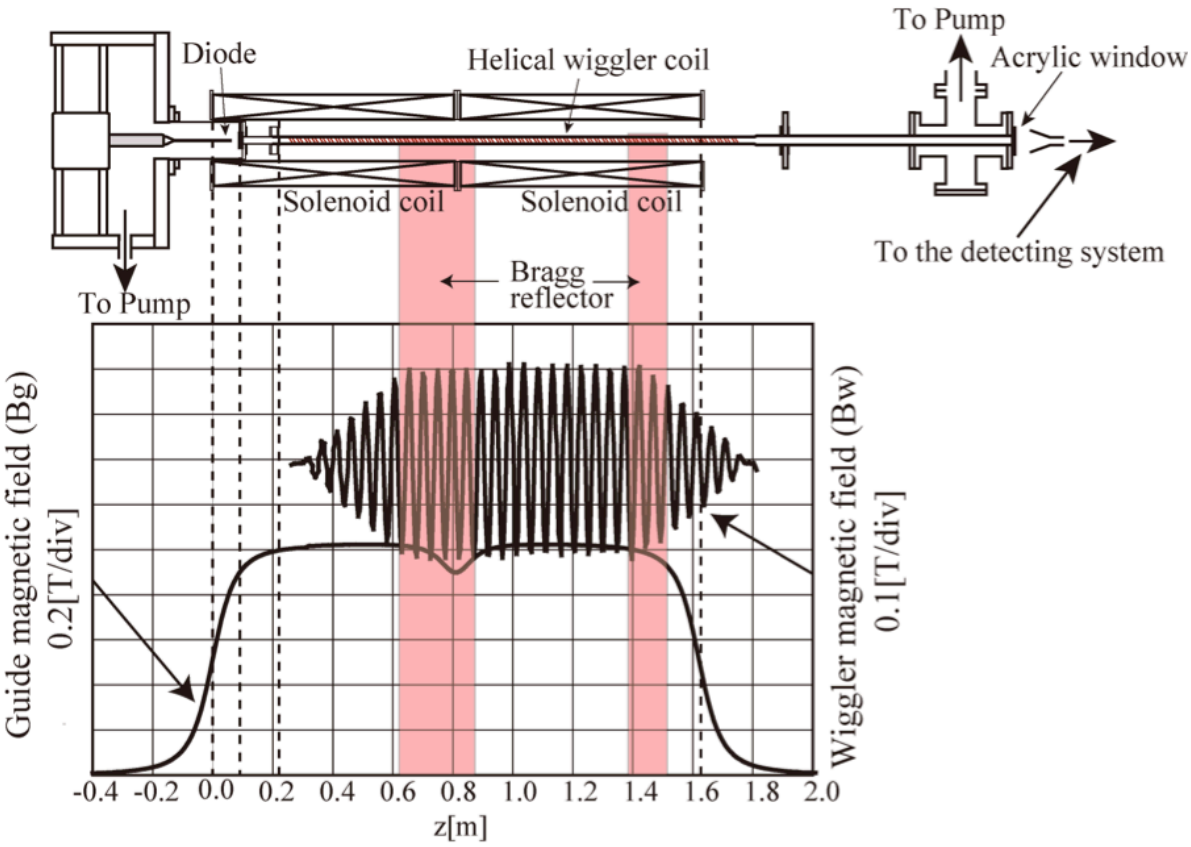

Fig.2 Experimental setup.

utilized to examine the radiated frequency roughly.

3. Experimental results.

3.1. 54 GHz FEM experiment

At first, no Bragg resonator was used. An IREB was injected into the cylindrical tube immersed in the helical and the axial magnetic field. The beam current and the energy were not changed by the strength of the helical magnetic field between 0-0.12 T and the axial magnetic field over 0.5 T. The signals of radiation over 40 GHz were shown in Fig. 3. Hereafter, in the figure, the upper waveform indicated the diode voltage as a time scale. When the strength of the helical magnetic field (Bh) was changed, the output power of radiation was not changed without Bragg resonator.

The metal disk with a hole at the center was placed at the end of the drift tube as a

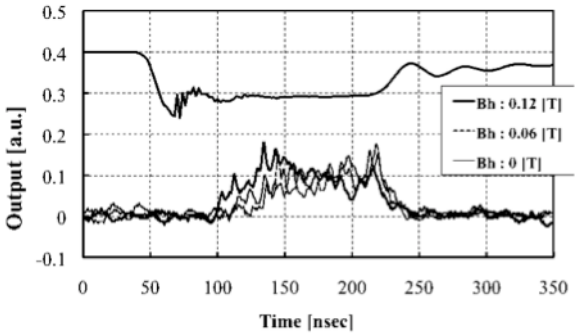

Fig. 3. The output signals of radiation without the Bragg resonator(lower). Upper signal indicates the diode voltage as a time scale.

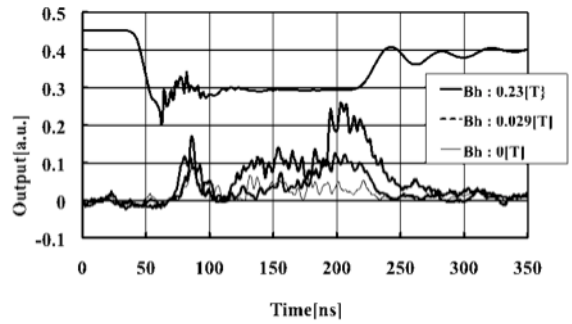

Fig. 4. The output signals of radiation with the 50 GHz high pass disk.

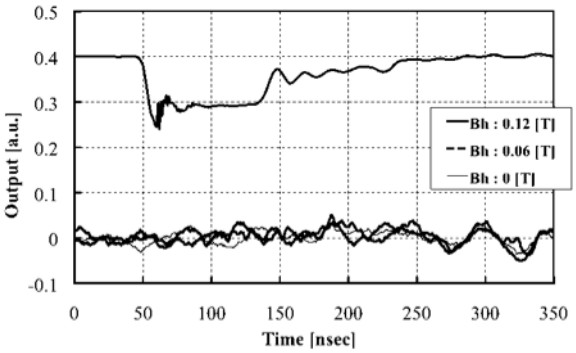

Fig. 5. The output signals of radiation with the 60 GHz high pass disk.

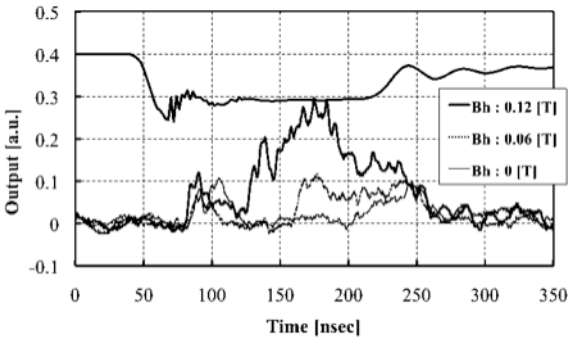

Fig. 6. The output signals of radiation with the 54 GHz normal Bragg resonator.

high pass filter. When the disk with 50 GHz cut-off frequency was utilized, the radiation power was changed by the strength of the helical magnetic field as shown in Fig. 4. No radiation was observed with the 60 GHz cut-off disk as shown in Fig. 5. It was suspected that the radiation with frequency below 50 GHz was observed and the 54 GHz FEM radiation was covered by it in Fig. 3.

Figure 6 shows the signals of radiation with the 54 GHz normal Bragg resonator. The radiation power increased as the strength of the helical magnetic field increased.

In Figs. 4 and 6, we notice that the radiation started to grow around 70 ns after the rise of the voltage waveform, as the theoretical prediction of the estimated growth time for FEM was around 100 ns. In both cases, the radiation power was not changed by the axial magnetic field. And the radiation power was not observed when the helical field was not applied. So that, we concluded that the FEL radiation was observed in Figs. 4 and 6. The mode was estimated to be 54 GHz TE_{11} mode. The 54 GHz normal Bragg resonator worked as a frequency selector.

3.2. 40 GHz FEM experiment.

Because the beam source was not good condition for 54 GHz experiment, we decreased the radiation frequency to 40 GHz. The traditional and the advanced Bragg reflectors were designed and made. The results of cold test for both reflectors are shown in Fig. 7. The microwave reflected by the Bragg reflector was observed. It is clear that the reflected frequency width of the advanced Bragg reflector is narrower than that of the traditional one.

We observed the radiation with the 35.5-40 GHz band pass filter.

Also in the 40 GHz case, the radiation whose output power depended on the strength of the helical magnetic field was not observed without any Bragg resonator.

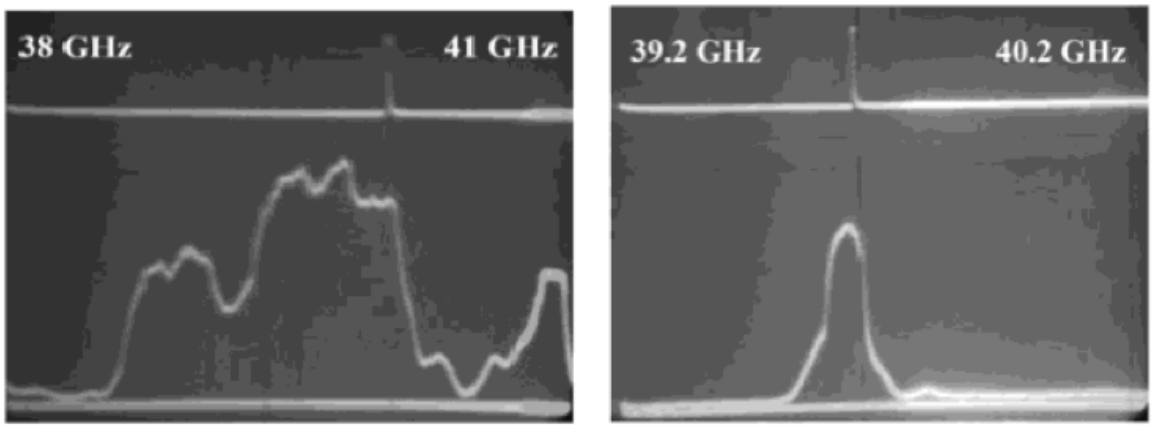

Fig. 7. Cold tests of the normal (left) and the advanced (right) Bragg rreflectors. The reflected signals are shown.

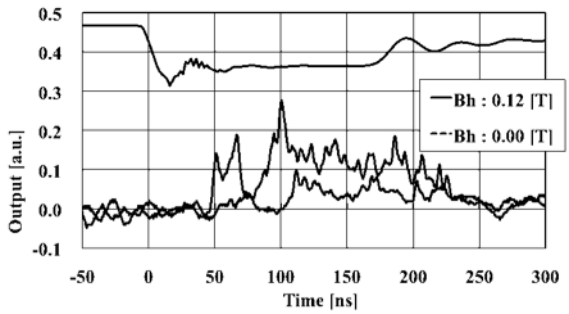

Fig. 8. The output signals of radiation with the 40 GHz normal Bragg resonator.

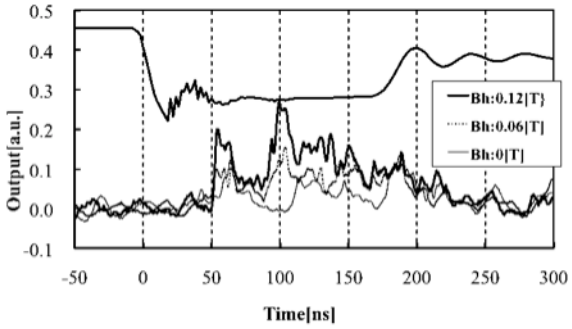

Fig. 9. The output signals of radiation with the 40 GHz hybrid Bragg resonator.

Figure 8 shows the observed radiation from FEM with the normal Bragg resonator, and figure 9 shows that with the hybrid Bragg resonator.

In both figures 8 and 9, the signals of radiation were observed after 70 ns from the beam injection and the signals whose output power depended on the strength of the helical magnetic field were detected. However, the advantage of the frequency selectivity of the hybrid Bragg resonator cannot be examined because we have not the spectrometer with high resolution. And problem of the

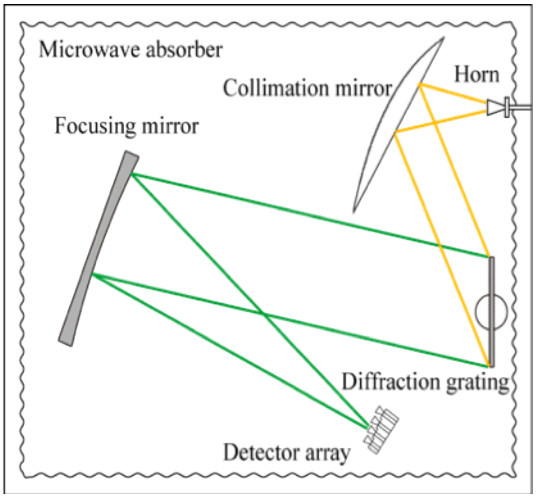

Fig. 10. Spectrometer using a diffraction grating.

reproducibility of the radiation was remained.

Now we started to calibrate the spectrometer with the frequency resolution less than 0.5 GHz using diffraction grating as shown in Fig. 10.

4. Conclusion.

We carried out the preliminary experiments on FEM radiation with a helical wiggler coil using an intense relativistic electron beam. It is concluded that the radiation whose output intensity was changed by the strength of the helical magnetic field was observed using the normal and the hybrid Bragg resonator. And the observed frequency lied between 35.5-40 GHz and the FEM radiation with TE11 mode was estimated from the experimental parameters. We will continue the experiments to clear the advantage of the advanced Bragg resonator.

A part of this work is supported by a Grant-in-Aid for Scientific Research from Ministry of Education, Science, Sports and Culture, Japan.

References

1) P. H. Siegel, IEEE Trans. on Microwave Theory Tech. 50, 910-927 (2002)
2) G. P. Gallerano, and S. Biedron, , Proceeding of the 2004 FEL Conference, 216-221 (2004)
3) V. L. Bratman,, 46, 769-781 (2003)
4) T. Idehara et al. IRMMW-THz. Joint 32nd Int. Conf. on, pp. 309 - 311, 2007.
5) V. L. Bratman, G. G. Denisov, N. S. Ginzburg, and M. I. Petelin, "FEL's with Bragg Reflection Resonators: Cyclotron Autoresonance Masers Versus Ubitrons", IEEE J. Quantum Electron., 19, 282-296 (1983)
6)C. K. Chong, D. B. McDermott, M. M. Razeghi, N. C. Luhmann, Jr., J. Pretterebner, D. Wagner, M. Thumm, M. Caplan, and B. Kulke, "Bragg Reflectors", IEEE Trans. on Plasma Sci., 20, 393-402 (1992)
7) T. S. Chu, F. V. Hartemann, B. G. Danly, and R. J. Temkin, "Single-Mode Operation of a Bragg Free-Electron Maser Oscillator", Phys. Rev. Lett., 72, 2391-2394 (1994)
8) J. Chen, M. C. Wang, Z. Wang, Z. Lu, L. Zhang, and B. Feng, "Study of a Raman Free-Electron Laser Oscillator with Bragg Reflection Resonators", IEEE J. Quantum Electron., 27, 488-495 (1991)
9) N. S. Ginzburg, A. M. Malkin, N. Yu. Peskov, A. S. Sergeev, A. K. Kaminsky, S. N. Sedykh, E. A. Perelshtein, A. P. Sergeev, A. V. Elzhow, "Improving selectivity of free electron maser with 1D Bragg resonator using coupling of propagating and trapped waves", Phys. Rev. Special topics accelerators and beams, 8, 040705 (2005)

PARTICLE SIMULATION STUDY OF BACKWARD WAVE OSCILLATOR USING CST STUDIO SUITE

Y. Soga, M. Kato, T. Mimura, K. Kamada and M. Yoshida [1)]

Graduate School of Natural Science and Technology, Kanazawa University, Kakuma-machi, Kanazawa, Ishikawa, 920-1192, Japan
1) High Energy Accelerator Research Organization, 1-1 Oho, Tsukuba, Ibaraki 305-0801 Japan

ABSTRACT

Simulation studies using CST Particle Studio have been carried out on newly designed compact helix and interdigital backward-wave oscillators (BWO). The steady state of oscillations is observed at a frequency of 8.3 GHz from the helix BWO stimulated by a hollow-shaped electron beam. An electron-beam injected into the outside of the helix circuit induces stronger radiation than the inner one. In the interdigital BWO steady radiation is observed at a frequency 100 GHz with output power of approximately 1 W stimulated by a single electron-beam. When two beams were injected into both sides of the interdigital circuit, the output power of radiation increased by a factor of four. These observations could offer a key to better performance of a compact BWO.

I. Introduction

Compact electron tubes at terahertz (THz) frequencies offer enormous applications for medical diagnostic, broad-band communication and spectroscopy. Backward-wave oscillator (BWO) is a typical candidate of compact terahertz sources [1]. One of the advantages of BWO is that the backward-wave frequency is tunable with electron-beam energy because the phase velocity of a backward-wave which is equal to approximate speed of the electron-beam depends on the frequency [2]. The output power of a terahertz band BWO, however, has been limited to 100 mW at most at 1 THz. This is because the structure of a terahertz BWO is comparable in size to the wavelength of 0.3 mm and then the interaction region and coupled-interaction impedance between electrons and a slow wave circuit reduces. The purpose of our study is to increase in the output power up to 1 W of a compact terahertz BWO with newly designed electron beam distributions and slow wave structures (SWS). In this paper, we report a preliminary investigation of the fundamental characteristics of a compact BWO by using CST Studio Suite.

II. Simulation Model : Helix BWO

At first we calculate a helix BWO at a frequency 10 GHz to evaluate the simulation method before starting a simulation of an interdigital BWO at terahertz frequencies.

We can achieve a massive simulation of charged particles by using Particle Studios (Electrostatic, Magnetostatic, and Particle Tracking solvers) in CST Studio Suite [3]. The algorithms used in CST Studio Suite are based on the Finite Integration Technique (FIT) and Perfect Boundary Approximation (PBA) to discretize the Maxwell equations on space. These methods combine good geometrical accuracy with the

memory efficiency and performance of broadband time domain solvers, delivering reliable results at high speed.

The electron-beam velocity could be synchronous with the axial phase velocity of the backward-wave because the wave propagates along a helical path of the slow wave circuit. At a frequency such that the electron transit angle from turn to turn is π, there are two turns per wavelength. A backward wave interaction can occur at the wave number between π and 2π [4].

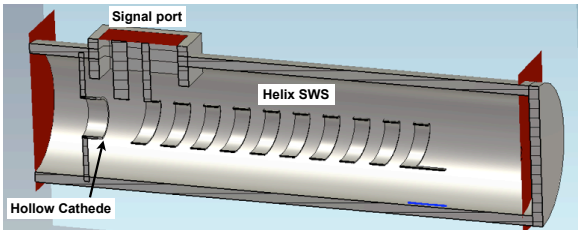

Fig.1: 3D view of helix BWO.

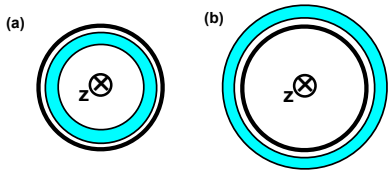

Fig.2: Configuration of electron beams.

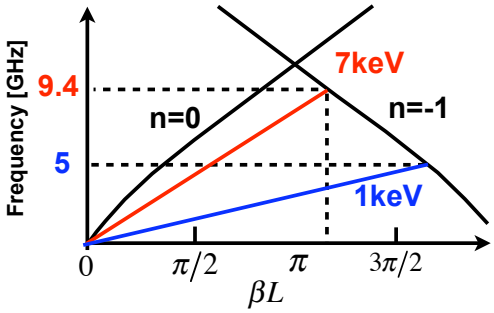

Fig.3: Dispersion relation of helix SWS and beam modes.

The basic scheme of the helix BWO we designed consists of the slow wave circuit which is helical in structure with 10 periods (3 mm/period) and electron-beam with energy of 7 keV, typical current density of 66 A/cm^2 emitted from hollow-shaped cathode in the homogeneous magnetic field 0.5 T as shown in Figs. 1 and 2(a). A backward-wave oscillation at frequency of 9.4 GHz with beam energy of 7 keV is predicted by the dispersion analysis (Fig. 2). The waveguide port is placed at the end of the tube on the same side of the cathode as shown in Fig. 1. We can detect backward-wave only by matching the load impedance of the waveguide port.

III. Simulation Result : Helix BWO

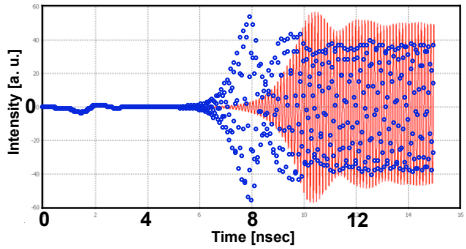

Fig.4: Output signal of helix BWO detected by observation port. The oscillation is stimulated by the inner beam (Blue) and the outer one (Red).

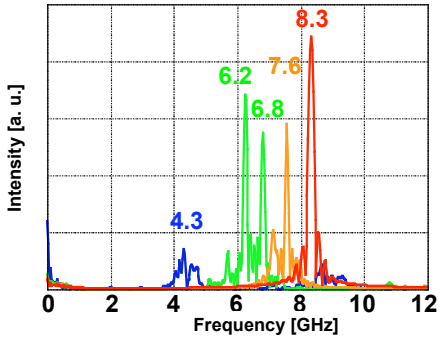

Fig.5: Spectrum analyses of helix BWO.

The steady state of oscillation at frequency of 8.3 GHz was observed at 8 nsec after the beam injection with beam current of 1.67 A injected into the inner of SWS (Fig. 4:Blue points). The slight difference of the frequencies between the observation and the calculation on the dispersion analysis (Fig. 3) is result

from distortion near the intersection at the wave number π in the dispersion.

We also verified the characteristics of broadband and tunability of a backward-wave frequency. As shown in Fig. 5, when the injection energy of the electron-beam is swept from 1 to 7 keV, the frequency of radiation changed from 4.3 to 8.3 GHz. These results show good agreement with the prediction of dispersion analyses (Fig. 3).

To increase the interaction region between electrons and SWS, we have examined new configurations of the electron-beam shown in Fig. 2(b). When the beam is injected into the outside of the helix circuit, the field strength of steady radiation increased shown in Fig.4 (Red). This result suggests that increasing the interaction region between an electron-beam and SWS is required to construct a high power BWO.

IV. Simulation Model : Interdigital BWO

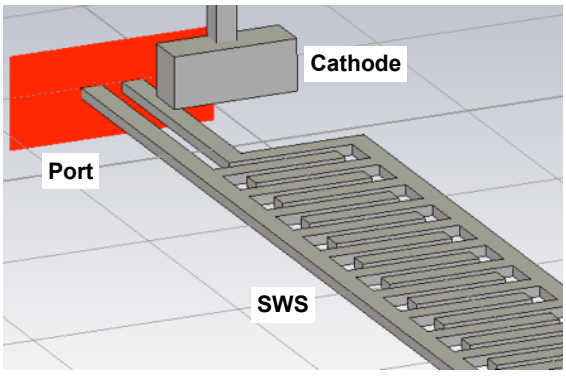

Fig.6: 3D view of interdigital BWO.

The basic scheme of the interdigital BWO we designed consists of the slow wave circuit which is interdigital in structure with 200 periods (0.15 mm/period) and electron-beam with energy of 10 keV, typical current density of 20 A/cm^2 emitted from 0.25 mm $\times$ 0.6 mm rectangular cathode in the homogeneous magnetic field 1 T. The distance between a bottom of the electron beam and the SWS surface in the interaction region is approximately 0.1 mm. A backward-wave oscillation at frequency of 100 GHz with beam energy of 10 keV is predicted by the dispersion analysis (Fig. 7). The waveguide port is placed at the end of the tube on the same side of the cathode as shown in Fig. 6. We can detect backward-wave only by matching the load impedance of the waveguide port.

V. Simulation Result : Interdigital BWO

The steady state of oscillation was observed at frequency of 100 GHz with output power of approximately 1 W, beam current of 30 mA at 17 nsec after the 10 keV beam injection (Fig. 8 (a) and Fig.9). The frequency is consistent with that of calculation on the dispersion analysis (Fig. 7). Figure 8 (b) represents a typical distribution of the axial electric field observed during the steady oscillation. Since the positive peak of the electric field exists at intervals of four periods of the slow wave circuit, it is obvious that a dominant phase shift $\pi/2$ per period occurs on the fundamental backward wave dispersion curve.

We also verified the characteristics of broadband and tunability of a backward-wave frequency. As shown in Fig. 9, when the injection energy of the electron-beam is swept from 5 to 20 keV, the frequency of radiation changed from 83 to 114 GHz. These results show good agreement with the prediction of dispersion analyses (Fig. 7).

The dependences of the electric field strength of radiation and the time until oscillation starts on a beam current density are plotted in Fig. 10. The oscillation occurred above the threshold beam current density 13.3 A/cm^2 and the field intensity keeps rising as beam current density increases. An interesting observation was that the field intensity is proportional to a beam current density more than 20 A/cm^2 while the time lag is inversely proportional to that for all data.

To increase the interaction region between electrons and SWS, we have examined new configurations of

BWO shown in Fig. 11. When two beams were injected into both sides of the interdigital circuit (Fig. 11(a)), the field strength of steady radiation increased by twice, that is, the output power increased by a factor of four. We have also observed the steady state oscillation in the structure shown in Fig. 11 (b). These results suggest that it is possible to construct a high power BWO using SWS and electron-beams piled alternately in the structure.

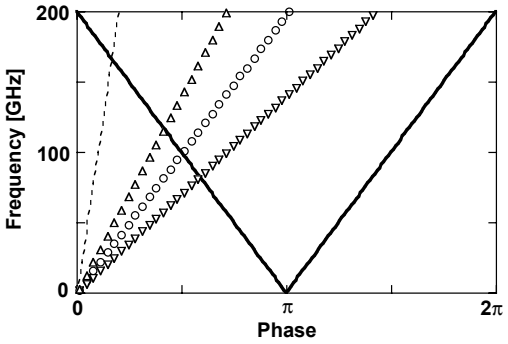

Fig.7: Dispersion relation for interdigital SWS (solid lines) and electron-beam modes with different energies.

VI. Conclusion

To increase the output power of radiation in a compact BWO it is favorable to increase an interaction region by using plural SWSs and beams (Fig. 11). Although the field strength increases linearly as a current density as shown in Fig. 10, it is difficult to use a beam with a high current density because of the limit of emitters in electron sources and the instability of the strongly bunched electrons.

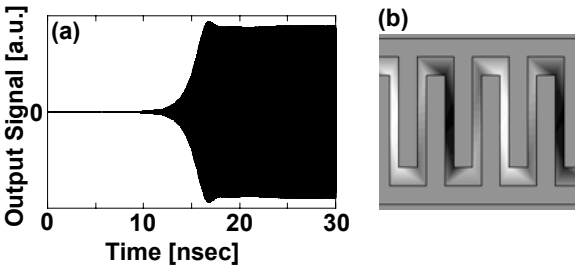

Fig.8: (a) Output signal detected at the waveguide port. (b)Axial electric field pattern. The luminosity increases with the strength of the electric field.

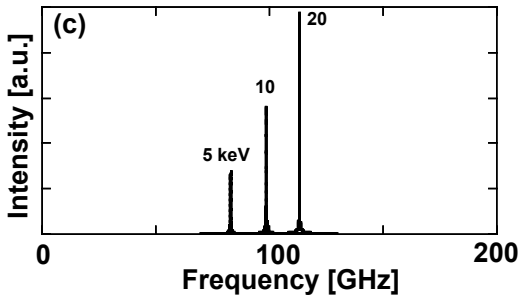

Fig.9: Spectrum analyses of interdigital BWO.

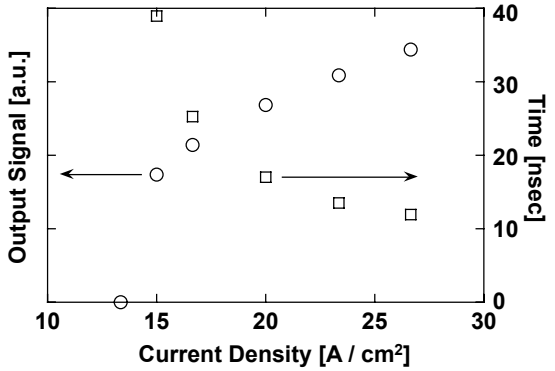

Fig.10: Beam current dependence of time until oscillation starts (square) and output intensity (circle).

In summary, we examined the fundamental characteristics of a compact BWO with interdigital circuit in structure using CST Studio Suite. The steady state of oscillation was observed at frequency 100 GHz with output power of approximately 1 W. The results indicated by CST simulations are in good agreement with the dispersion analyses. When two beams were injected into both sides of the interdigital circuit, the output power of radiation increased by a factor of four. This observation could offer a key to better performance of a compact BWO using plural SWSs and electron-beams.

This work is supported by a Grant-in-Aid for Young Scientist (B).

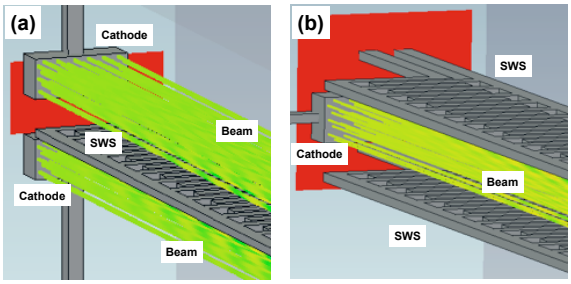

Fig.11: 3D view of newly designed BWO. (a) Single-beam and double SWSs. (b) Double beams and single SWS.

References

[1] Vishnu Srivastava, Journal of Physics Conference Series, 114, 012015, (2008)

[2] A. S. Gilmour, Jr., Principles of Traveling Wave Tubes, (Artech House Radar Library, 1994)

[3] www.cst.com

[4] Kenneth J. Button, Infrared and Millimeter Waves vol.1, (Academic Press, 1979)

Time integrated spectrum pinhole images of H-like N Z-pinch discharge plasma for realizing a Balmer α recombination soft X-ray laser

Yuya ISHIZUKA, Yusuke SAKAI, Yasuaki NAKANISHI,
Toru KAWAMURA, Masato WATANABE and Eiki HOTTA

Department of Energy Sciences, Tokyo Institute of Technology,
4259-J2-35, Nagatsuta, Midori-ku, Yokohama 226-8502, Japan

ABSTRACT

It is considered that lasing of a H-like N Balmer α soft X-ray laser (SXRL) at a wavelength of 13.4 nm might be possible by utilizing an expansion phase of Z-pinch discharge plasma. To realize the recombination SXRL, strong ionization to NVIII state with electron temperature of $T_e \approx$ 150-200 eV and electron number density of $n_e \approx 1 \times 10^{20}$ cm^{-3} at the maximum pinch and following rapid recombination caused by expansion cooling of the non-equilibrium plasma resulted in temperature below $T_e \approx 50$ eV and $n_e \approx 10^{19}$ cm^{-3} in about 10 ns are required. Utilizing a triangular current with peak amplitude of about 50 kA and a pulse width of about 50 ns, characteristics of spectrum pinhole images emitted from H-like N plasma are shown to investigate the correlation between estimated plasma parameters and the nitrogen ionic charge states for future Balmer α SXRL study.

I. Introduction

A capillary Z-pinch discharge soft X-ray laser (SXRL) is a promising scheme with its long plasma column of about a few 10s cm in which the radiation is efficiently amplified[1]. Lasing of the Ne-like Ar SXRL at wavelength of 46.9 nm has been observed as a spike in X-ray photodiode signal, which occurred supposedly in an implosion phase with concave electron density profiles, by utilizing a discharge current of about 10 kA[2, 3] and its high coherence has been shown by the clear interference fringes[4, 5, 6, 7]. Concerning the shortening of its wavelength, much effort has been made resulting in an amplification of a 13.2 nm Ni-like Cd line and a 18.2 nm H-like C VI recombination line[8, 9, 10, 11, 12]. However, there is no demonstration of saturated lasing at these shorter wavelengths, because it is still difficult to generate a highly uniform long plasma column with length of several to several 10s cm by using a medium which is solid at room temperature. To realize the SXRL at shorter wavelength utilizing capillary discharge scheme, the possibility of the H-like N recombination SXRL at wavelength of 13.4 nm has been investigated[13, 14]. To generate the population inversion between the principal quantum number n=2 and 3, sufficient ionization to NVIII state at the maximum pinch and following rapid expansion cooling of the non-equilibrium plasma are

necessary.

At the maximum pinch, electron temperature of $T_e \approx$ 150-200 eV and electron number density of $n_e \approx 1\times 10^{20}$ cm^{-3} are needed in order to generate sufficient NVIII ions in about several ns[15]. In the subsequent expansion phase where the population inversion between the principal quantum number n=2 and 3 is expected, formation of a rapidly cooled expanding plasma with $T_e < 50$ eV and $n_e \approx 1\times 10^{18\text{-}19}$ cm^{-3} in which the collisional de-excitation process from a higher excited level dominates is required[13]. Furthermore, the rapid expansion cooling should be completed within about 10 ns while the recombination from NVIII to NVII state proceeds, in order to avoid establishment of thermal equilibrium with respect to a ground state of the H-like N ion, which is mainly caused by the radiation trapping between n=1 and 2[16, 17]. In this study, characteristics of the emission spectrum of H-like N ion generated by capillary discharge is investigated to show the correlation between estimated plasma parameters and the nitrogen ion charge states for future realization of H-like N Balmer α SXRL.

II. Experimental

Capillary discharge plasma was generated by utilizing a triangular current with peak amplitude of about 50 kA and pulse width of about 50 ns. A pulsed power supply system with a wave shaping transmission line was used[18, 19]. An alumina (Al_2O_3) ceramics capillary with an inner radius of 1.5 mm and a length of 75 mm was filled with nitrogen molecular gas at initial filling pressures (estimated initial NII number density) of about 2500 mTorr (*NII* ≈ 1.5×10^{17} cm^{-3}), 1500 mTorr (*NII* ≈ 1.0×10^{17} cm^{-3}), 1000 mTorr (*NII* ≈ 6.5×10^{16} cm^{-3}), 750 mTorr (*NII* ≈ 5.0×10^{16} cm^{-3}), 250 mTorr (*NII* ≈ 1.5×10^{16} cm^{-3}). The gas was pre-ionized by RC discharge with amplitude of about 10 A and decay time constant of 3 μs.

Schematic diagram of time integrated spectrum pinhole imaging setup is illustrated in Fig. 1. The measurement of radiation from the nitrogen plasma was carried out using a transmission grating spectrometer with a lattice constant of 1/1000 mm^{-1} in combination with an X-ray CCD camera which has 1024×1024 pixels. Each pixel has an area of 13 μm square. The transmission grating was placed at a distance of 600 mm from the end of capillary and a distance between the grating and the CCD camera was 425 mm. In addition, two slits which have width of 1mm were placed between the capillary and the transmission grating.

Radiation temperature of the nitrogen plasma was estimated by fitting the slope of the obtained spectrum with the following Planck formula assuming that electron and photon are in thermal equilibrium in high density z-pinch plasma.

$$I \propto \exp(-\hbar\omega/T)$$

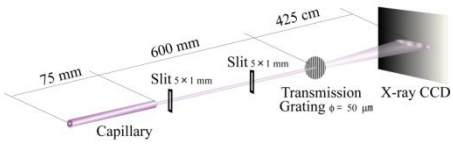

Fig. 1. Time integrated spectrum pinhole imaging setup

III. Experimental results and discussions

Obtained spectrum pinhole images are shown in Fig. 2. In the z-pinch plasma, ionization to NVI state is proceeded in the implosion phase with T_e of only a few 10s eV. However, ionization to NVII or NVIII higher charge states, which have larger ionization potential, are possible to exist only at the maximum pinch instant. Therefore, spatial distribution of the He α line at a wavelength of about 3 nm is mainly

supposed to have information at the maximum pinch instant and spatial distribution of Balmer series at wavelength below about 10 nm are considered to have information in the expansion phase. Plasma parameter at the maximum pinch is possible to be obtained using the on-axis spectrum profiles and that in the expansion phase is possible to be obtained using the off-axis spectrum profiles.

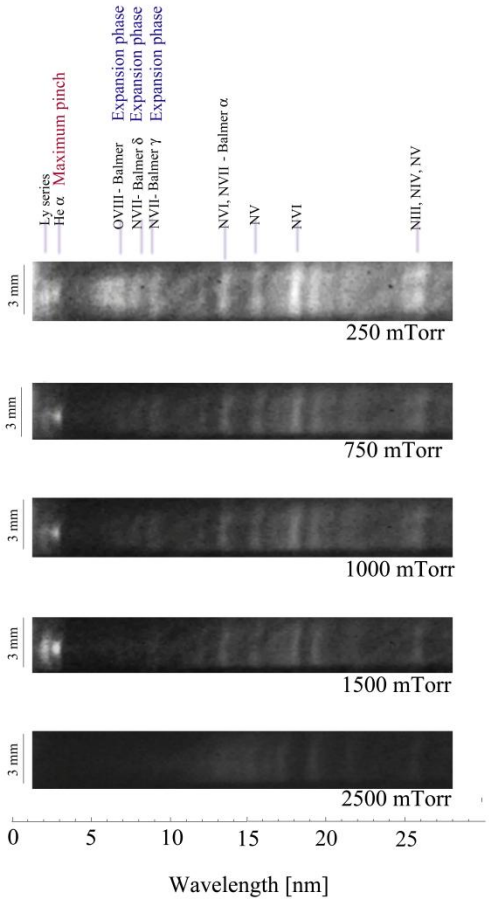

Fig. 2. Observed time integrated spectrum pinhole images at various initial N_2 gas pressures

III.A. Maximum pinch

Obtained on-axis spectrum profiles for various initial gas pressures, at wavelength of below 15 nm, are shown in Fig. 3 and radiation temperature are estimated as shown in Fig. 4 using the photon energy spectrum at around several 10s eV. Correlation between the estimated radiation temperature $T_{rad} \approx T_e \approx T_{ion}$ and ion charge state at various gas pressures is analyzed as follows.

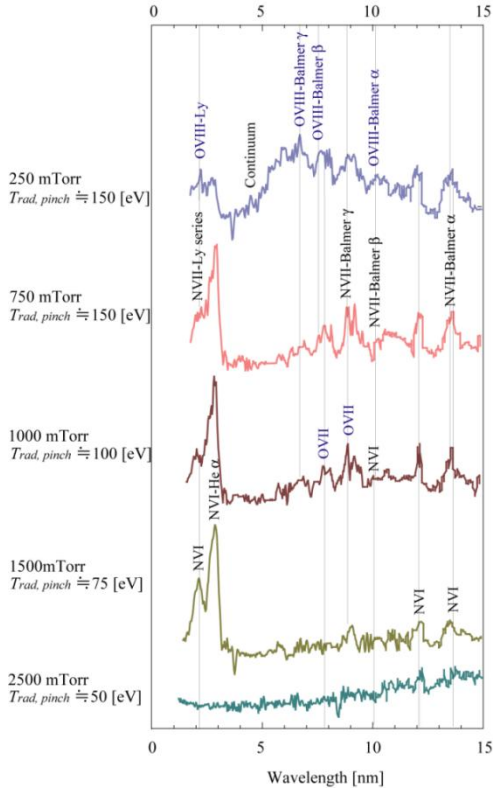

Fig.3. On-axis emission spectrum profiles at various initial gas pressures. These spectra are expected to have the information at the maximum pinch.

(a). $N_{2,\ initial}$ = 2500 mTorr, $T_{rad,\ pinch} \approx$ 50 eV

Estimated radiation temperature is about 50 eV and no line of highly ionized NVII state is observed. Line spectra of NVI at wavelength of 12 nm are observed.

(b). $N_{2,\ initial}$ = 1500 mTorr, $T_{rad,\ pinch} \approx$ 75 eV

Estimated radiation temperature is increased to about 75 eV and He α lines, at wavelength of around 3 nm, of NVI are clearly confirmed. However, electron temperature is considered to be not enough in order to ionize the nitrogen ions up to H-like N state, which has an ionization potential of about 500 eV. Therefore, weak radiation at around 13-14 nm is considered to be mainly radiated from NVI states.

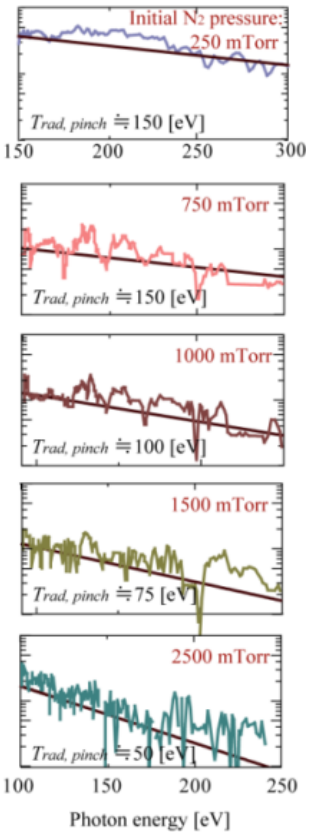

Fig. 4.Estimated on-axis radiation temperature, fitted with a spectrum profile at around several 10s eV using Planck formula.

(c). $N_{2,\ initial}$ = 1000 mTorr, $T_{rad,\ pinch} \approx$ 100 eV

Discrete line spectra at wavelength below 10 nm are observed with estimated radiation temperature of about 100 eV. Although it is hard to distinguish the Balmer series of NVII states and OVII and Balmer series of OVIII clearly, weak radiation at wavelength of 6-7 nm may indicate the Baler series of OVIII with higher ionization potential than that of NVII. Therefore, existence of NVII is anticipated with radiation temperature of about 100 eV. In addition, radiation from NVI at wavelength of about 12 nm clearly exists.

(d). $N_{2,\ initial}$ = 750 mTorr, $T_{rad,\ pinch} \approx$ 150 eV

By reducing the initial nitrogen gas pressure, estimated radiation temperature at the maximum pinch is increased to about 150 eV, resulting in the enhancement of Lyman series at shorter wavelength. Therefore, highly excited states of H-like N ions are expected and existence of essential NVIII is anticipated.

(e). $N_{2,\ initial}$ = 250 mTorr, $T_{rad,\ pinch} \approx$ 150 eV

Estimated radiation temperature at the maximum pinch is saturated to about 150 eV. Radiation of Balmer series of OVIII is strongly enhanced at wavelength of about 6-8 nm, which suggests the increase of material ablated from the alumina capillary inner wall. In addition, continuum radiation from the H-like O is expected at wavelength of bellow 6-7 nm. Although it is still hard to distinguish the Balmer series of H-like N ions and H-like O, existence of fully stripped oxygen ion could be an evidence of generation of NVIII with maximum radiation temperature of about 150 eV. Radiation from an Al ion which has nearly continuous spectrum in highly excited states is expected to be added as like a back ground radiation at wavelength of several nm range. It can be considered that increase of amount of aluminum and oxygen ions prevents the increase of the maximum electron temperature at the maximum pinch by insufficient compression or radiation cooling of pinched plasma.

The minimum pinch radius was estimated by using the spatial distribution of the He α line which is expected to exist at the beginning of the maximum pinch. Estimated minimum radii at initial gas pressure of 750 mTorr and 1000 mTorr are about 150 μm, that is one tenth of capillary inner radius. Assuming that at the maximum pinch nitrogen plasma is fully ionized to over NVI state, the electron number density at the maximum pinch is estimated to be

$$n_e \approx Z \times (r_{initial} / r_{\min})^2 \times n_{N\prod}$$
$$\approx 5 \times 10^{19} [cm^{-3}],$$

where Z is the average charge state number $Z \approx 5$,

n_{NII} is the initial NII number density of about $n_{NII} \approx 5 \times 10^{16}$ cm^{-3}. In addition, assuming that duration of maximum pinch is about 5 ns[20], the number density of fully stripped nitrogen is estimated to be

$$j(150[eV]) \times n_e \times \Delta t \approx j(150[eV])[cm^3 s^{-1}] \times (5 \times 10^{19}\,[cm^{-3}]) \times 5[ns] \leq 0.5,$$

where j is the Seaton's ionization rate coefficient[21].

III.B. Expansion phase

Spatial distribution of pinhole images radiated from NVII ion at wavelength of around several nm has information in the expansion phase. From obtained off-axis emission spectrum profiles, radiation temperature and electron number density estimated by utilizing the plasma radius are shown in Fig. 5 at initial gas pressures of about 1500 mTorr, 750 mTorr and 250 mTorr. In Fig. 5, spectrum profiles at radii of 0-200 μm, 400-600 μm and 800-1000 μm are shown.

(a). $N_{2,\ initial}$ = 1500 mTorr, $T_{rad,\ pinch} \approx$ 100 eV

When the initial gas pressure is 1500 mTorr, in which estimated maximum radiation temperature is $T_{rad,\ pinch} \approx$ 100 eV, ionization to NVIII cannot be expected and relative intensity of Balmer α and γ series to a line of NVI at wavelength of 12 nm is almost same in on- and off-axis regions.

(b). $N_{2,\ initial}$ = 750 mTorr, $T_{rad,\ pinch} \approx$ 150 eV

When an initial gas pressure is about 750 mTorr, it is expected that pinched plasma with radius of about 200 μm, $T_{rad,\ pinch} \approx$ 150 eV and $n_e \approx 5 \times 10^{19}$ cm^{-3} expands to a radius of about 400-600 μm and is cooled down to 75 eV and $n_e \approx 1 \times 10^{19}$ cm^{-3}, and to a radius of about 800-1000 μm, 50 eV and $n_e \approx 2 \times 10^{18}$ cm^{-3}. It is expected that the expansion cooling proceeds in about 10 ns[20]. Along with the cooling of electron temperature, relative intensity of Balmer series, especially Balmer α line becomes slightly enhanced with respect to the line of NVI at wavelength of 12 nm at $T_{rad,\ exp} \approx$ 75 eV. However, these enhancement of relative intensity of Balmer series could not be observed at $T_{rad,\ exp} \approx$ 50 eV. The reason might come from the decrease of the electron number density with expansion cooling, resulting in decrease of collisional de-excitation rate from higher excited level. Also, in case of $T_{rad,\ exp} \approx$ 75 eV, it is observed that slight enhancement of emission intensity at the longer wavelength of Balmer series, which might suggest the satellite lines emitted through the dielectric recombination in the expansion phase. These results might show that there exists the possible induced emission of Balmer α line in the expansion phase. However, clear amplification of Balmer lines could not be observed in these experiments.

(c). $N_{2,\ initial}$ = 250 mTorr, $T_{rad,\ pinch} \approx$ 150 eV

When an initial gas pressure is 250 mTorr, relative enhancement of Balmer α is also observed in the off-axis region. In this case, although the pinched plasma with $T_{rad,\ pinch} \approx$ 150 eV is cooled down to $T_{rad,\ exp} \approx$ 75 eV with plasma radius of about 400-600 μm, temperature at radius of about 800-1000 μm is not cooled down to less than 75 eV. It is considered that with the decrease of initial ion density, additional heating is increased which is caused by mismatching between shorter pinch time and triangular current.

As a result, in case of estimated electron temperature of about 150 eV, relative enhancement of the Balmer α line emission from the recombining plasma has been observed, which might be initiated by the possible stimulated emission from the recombining plasma. However, clear amplification of laser line could not be observed in these experiments. In order to realize the recombination lasing, it is considered that higher electron and NVIII densities

are required, which needs slightly higher discharge current to generate higher energy density of the pinch plasma.

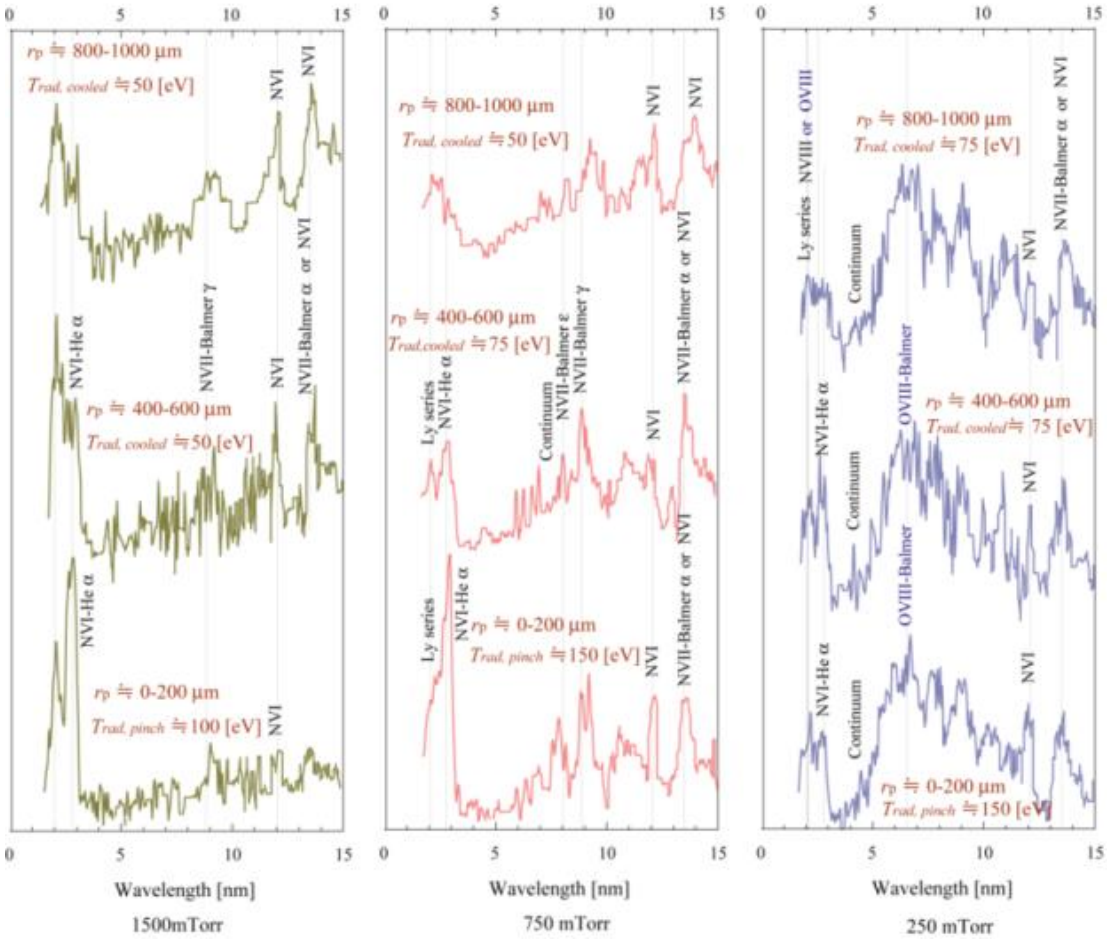

Fig. 5. Off-axis spectrum profiles at various initial gas pressures, which are expected to have information in the expansion phase.

Conclusion

Emission characteristics of capillary discharge plasma are analyzed by using time integrated spectrum pinhole images. Existence of H-like N ion is expected with estimated maximum radiation and electron temperature of over 100 eV and existence of NVIII is anticipated with electron temperature of about 150 eV from the on-axis spectrum profiles. In addition, slight relative enhancement of Balmer α and γlines might be observed in the off-axis spectrum profiles, which are expected to have information in the expansion phase. However, no clear amplification of laser lines was observed so that slightly higher NVIII and electron number density are required to realize the recombination lasing.

References

[1] J. J. Rocca, V. Shlyaptsev, F. G. Tomasel, O. D. Cortázar, D. Hartshorn, and J. L. A. Chilla, Demonstration of a Discharge Pumped Table-Top Soft-X-Ray Laser, Phys. Rev. Lett., Vol. 73, pp.

2192-2195 (1994)

[2] G. Niimi, Y. Hayashi, N. Sakamoto, M. Nakajima, A. Okino, M. Watanabe, K. Horioka, E. Hotta, Development and characterization of a low current capillary discharge for X-ray laser studies, IEEE Transactions on Plasma Science, Vol. 30, pp. 616-621 (2002)

[3] G. Tomassetti, A. Ritucci, A. Reale, L. Palladino, L. Reale, S. V. Kukhlevsky, F. Flora, L. Mezi, A. Faenov, T. Pikuz and A. Gaudieri, Toward a full optimization of a highly saturated soft-X-ray laser beam produced in extremely long capillary discharge amplifiers, Optics Communications, Vol. 231, pp. 403-411 (2004)

[4] J. J. Rocca, Table-top soft x-ray lasers, Rev. Sci. Instrum., Vol. 70, pp. 3799 (1999)

[5] Y. Liu, M. Seminario, F. G. Tomasel, C. Chang, J. J. Rocca, and D. T. Attwood, Achievement of essentially full spatial coherence in a high-average-power soft-x-ray laser, Phys. Rev. A, Vol. 63, No. 3, pp. 33802 (2001)

[6] A. Ritucci, G. Tomassetti, A. Reale, F. Flora and L. Mezi, Coherence properties of a quasi-Gaussian submilliradiant divergence soft-x-ray laser pumped by capillary discharges, Phys. Rev.A, Vol. 70, 023818 (2004)

[7] Y. Sakai, Y. Xiao, Y. Kakuya, M. Watanabe, A. Okino, and E. Hotta, Output characteristics of soft X-ray laser pumped by capillary discharge, IEEJ Transactions on Fundamentals and Materials, Vol. 126, No. 8, pp. 739-743 (2006)

[8] J. J. Rocca, M.C. Marconi, B. Szapiro, and J. Meyer, Experiments on soft x-ray laser development in a table top capillary discharge, Proceedings of SPIE, Ultra-short Wavelength Lasers, Vol. 1551, pp. 275, San Diego, California (1991)

[9] J. J. Rocca, M. C. Marconi, F. G. Tomasel, Study of the soft X-ray emission from carbon ions in a capillary discharge, IEEE Journal of Quantum Electronics, Vol. 29, Issue 1, pp. 182-191 (1993)

[10] H. J. Shin, D. E. Kim and T. N. Lee, Soft-x-ray amplification in a capillary discharge, Phys. Rev. Lett. E, Vol. 50, pp. 1376-1384 (1994).

[11] J. J. Rocca, J. L. A. Chilla, S. Sakadzic, A. Rahman, J. Filevich, E. Jankowska, E. C. Hammarsten and B. Luther, Advances in capillary discharge SXR research, Proceedings of SPIE, Vol. 4505, pp. 1-13 (2001).

[12] S. S. Ellwi, Z. Andrei, S. Plesli and H. J. Kunze, Probing of the active layers in a capillary discharge soft X-ray laser at 18.22 nm, Phys. Lett. A, Vol. 292, Issues 1-2, pp. 125-128 (2001)

[13] P. Vrba, M. Vrbova, N.Dezhda, A. Bobrova and P. V. Sasorov, Modeling of a nitrogen x-ray laser pumped by capillary discharge, Central European Journal of Physics, Vol. 3, pp. 564-580 (2005)

[14] N. S. Kampel, A. Rikanati, I. Be'ery, A. Ben-Kish, A. Fisher, and A. Ron, Feasibility of a nitrogen-recombination soft-x-ray laser using

capillary discharge Z pinch, Phys. Rev. E, Vol. 78, 056404 (2008).

[15] Y. Sakai, S. Takahashi, T. Hosokai, M. Watanabe, A. Okino and E. Hotta, The possibility of a capillary discharge soft X-ray laser with shorter wavelength by utilizing a recombination scheme, Journal of Plasma and Fusion Research Series, Vol. 8, pp. 1317-1312 (2009)

[16] K. Lee, J. H. Kim and D. Kim, Analytical study of the dynamics of capillary discharge plasmas for recombination x-ray lasers using H-like ions, Phys. Plasmas, Vol. 9, 4749 (2002)

[17] M. Masnavi, M. Nakajima , K. Horioka, Numerical Study on Gain Coefficient of a Capillary-Discharged Neon-Like Argon X-Ray Laser, IEEJ Transactions on Fundamentals and Materials, Vol. 126, pp. 250-255 (2006)

[18] Y. Sakai, T. Komatsu, I. Song, M. Watanabe, G. H Kim and E. Hotta, High efficient pulsed power supply system with a two-stage LC generator and a step-up transformer for fast capillary discharge soft X-ray laser at shorter wavelength, Review of Scientific Instruments., Vol. 81, 013303 (2010)

[19] Y. Sakai, S. Takahashi, M. Watanabe, G. H Kim and E. Hotta, Pulsed current wave shaping with a transmission line by utilizing superposition of a forward and a backward voltage wave for fast capillary Z-pinch discharge, Review of Scientific Instruments, Vol. 81, 043504 (2010)

[20] Y. Sakai, S. Takahashi, T. Hosokai, M. Watanabe, G. H Kim and E. Hotta, MHD control of capillary Z-pinch discharge by using a triangular current pulse for lasing a recombination soft X-ray laser, Journal of Applied Physics, Vol. 107, 083303 (2010)

[21] M. J. Seaton, The spectrum of the solar corona, Planetary and Space Science, Vol. 12, Issue 1, pp. 55-74 (1964)

PRELIMINARY INVESTIGATION ON PULSE LASER DEPOSITED AIN FOR FBAR APPLICATION

Z.P. Wang*, H. Ito, K. Masugata

Department of Electric and Electronic system Engineering, University of Toyama, 3190 Gofuku, Toyama 930-8555, Japan

ABSTRACT

In order to prepare high quality Aluminum nitride (AlN) films by pulse laser deposition for FBAR applications, dependence of N_2 pressure on crystal structure and surface morphology have been studied. The as-grown films were investigated using X-ray diffraction (XRD) and field-emission scanning electron microscopy (SEM). High-speed camera was used to capture the instantaneous states of ablation plasma. Poly-crystalline hexagonal AlN was formed under room temperature. It is found that average particle size increases with N_2 pressure.

I. Introduction

Aluminum nitride (AlN) is one of the most important optoelectronic materials in the wide band gap III-V semiconductors because of its wide and tunable energy band gap in conjunction with other nitrides, high thermal conductivity, doping capabilities, and high hardness (around 23.7 Gpa) [1].

With these properties, AlN has attracted much attention as a promising material for applications in microelectronic and optoelectronic devices, such as the piezoelectric layer in thin film bulk acoustic wave resonator (FBARs) [2,3], short-wavelength emitters and electronic packaging. In FBAR application, the devices basically consist of a piezoelectric film, sandwiched between metal electrodes. Most of piezoelectric materials can be used in FBAR devices, thereamong, AlN, Lead Zirconate Titanate (PZT) and zinc oxide (ZnO) are the most frequently employed. Compared to PZT film, AlN is not only a material with higher thermal and chemical stability, but also does not contain any pollution-contribution elements and is a harder material as well. [4]. AlN is preferred to ZnO since it has superior compatibility with silicon, higher BAW velocity, higher electrical resistivity, lower mass density, and a wider band gap [5]. Besides, ZnO is a n-type semiconductors that have low breakdown voltage and high dielectric losses [6].

In order to optimize the performance of FBAR devices, formation of high-quality AlN films becomes very important. There are several growth techniques have been developed to deposit AlN thin film, such as metal-organic chemical vapor deposition (MOCVD) [7,8], laser chemical vapor deposition (LCVD) [9], reactive sputter deposition [10-13], electron cyclotron resonance-plasma assisted chemical vapor deposition (ECR-PACVD) [14] and molecular beam epitaxy (MBE) [15]. There is one common disadvantage of these conventional methods that is the high substrate temperature ranging 800-1200 ^{O}C. Interfacial reaction between gas and substrate occurs while using temperature above 700℃, which brings extreme damage to the substrate. Pulse laser deposition (PLD) is believed to be a good choice to prevent interfacial reaction because of its low temperature growth process. Another very important feature of PLD is that it preserves nitrogen or oxygen stoichiometry of the target in deposited films [16]. However, there are also some drawbacks, such as mechanisms and dependence on parameters not well understood and not well suited for large-scale film growth. Whereas, since sensor application does not need large-area deposition, it is reasonable to not consider these

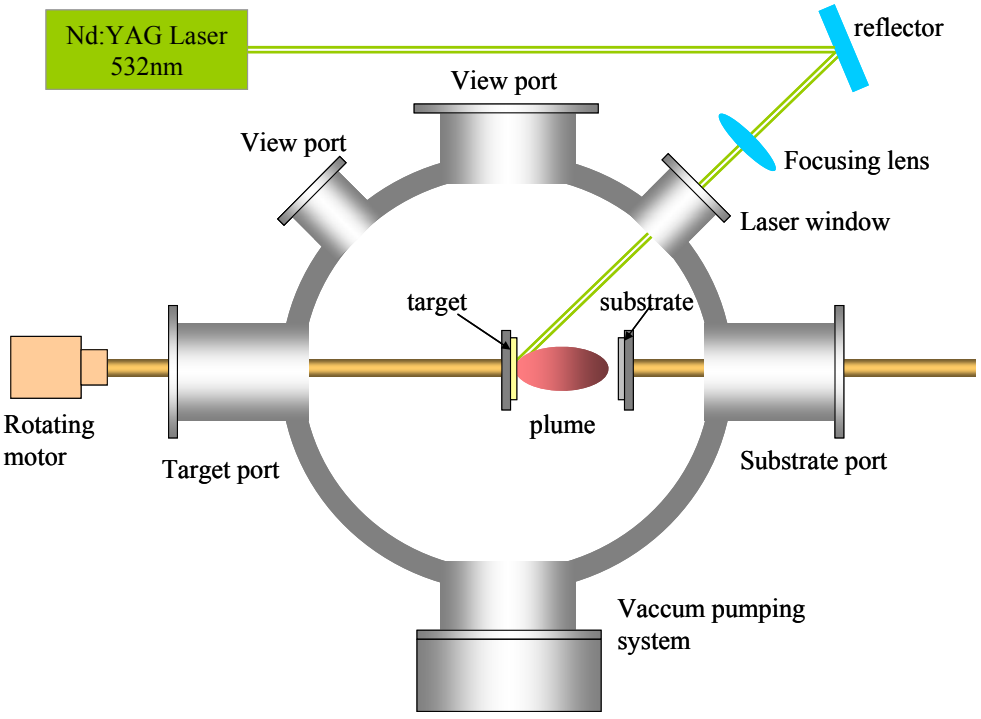

Fig.1. Experimental set-up.

limitations. In this paper, we report on our preliminary results on AlN formation by PLD.

Experiment

A second harmonic Q switched Nd:YAG laser (Continuum, Surelite III-10M), operating at 532nm with 5 ns pulse duration delivers a chosen energy of 380 mJ at a repetition rate of 10 Hz. The laser ablation of aluminum target in nitrogen plasma may not be suitable for the formation of a good quality nitride film as aluminum is known to eject a high fraction of aluminum particulates in PLD that can not readily and completely react to form stoichiometric nitride. As a result, the beam is focused with an energy density of 2 J/cm^2 on a rotating sintered AlN target (99.999%) located inside a vacuum chamber (base pressure 3×10-3 pa). Prior to deposition, substrates are cleaned in ultrasonic baths of acetone, rinsed in deionised water and dried in N_2. The physical properties of AlN films prepared by PLD mainly depend on the processing parameters such as deposition pressure, substrate temperature apart from the oxygen partial pressure, target substrate distance, laser pulse energy and pulse repetition rate.

In the present paper, in order to systematically study the growth of AlN thin films various conditions were reported: 1. Deposition in vacuum and at different nitrogen partial pressures. High purity nitrogen (99.999%) was used as the background gas applying subsequent pressure levels of N_2: 1, 10, 20, 30, 40, 50, 100, 200, 400, 600, 800 and 1000 Pa. 2. Deposition at various target-substrate distances ranging from 35 mm to 45 mm. 3. Deposition under different substrate temperature ranging from room temperature (RT) to 300 ℃. The as-deposited samples were investigated by X-ray diffraction (XRD, XRD-6000, Shimadzu), field-emission scanning electron microscopy (SEM, JSM- 6700F JEOL). High-speed camera was used to capture the instantaneous states of ablation plasma under different partial pressures.

Results and discussion

As known that pressure is a crucial parameter to pulse laser deposition, which affects the surface morphology and crystal structure a lot. In order to study the dependence of N_2 partial pressure on AlN film formation, the present experiment developed AlN films at different N_2 partial pressure ranging from vacuum to 2 Kpa by the flow of nitrogen into chamber. However, the interference fringes appeared in the films deposited at the N_2 partial pressure between 1 pa and 400 pa. The emergence of such interference fringes indicates not uniform surface with a thickness gradient [17]. Most of the films were smooth and

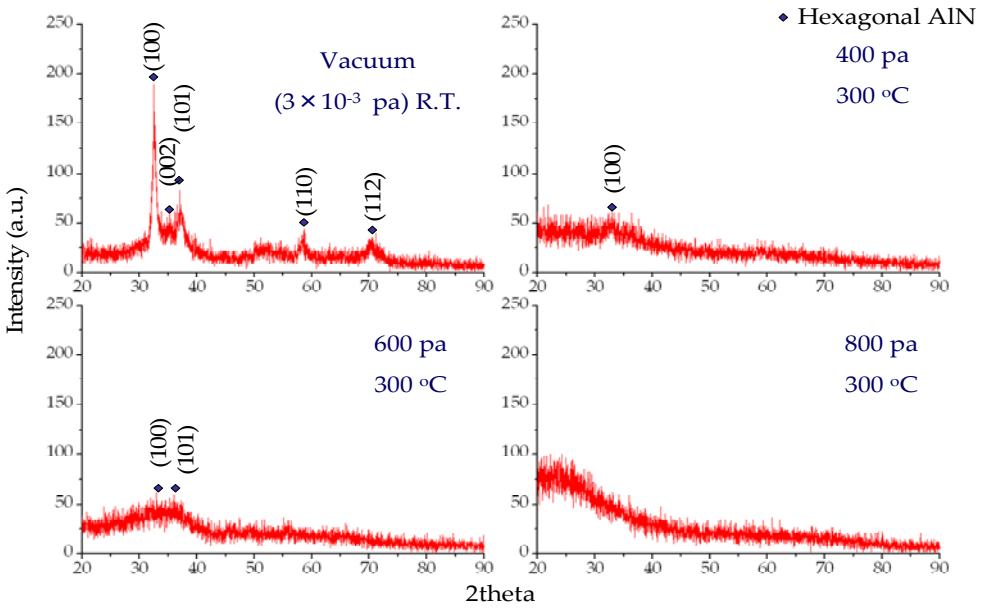

Fig.2. XRD pattern measured at various partial pressures.

transparent, but some of them appear very loose surface indicating high stress in the films according to the high mismatch between film and substrate, especially when at high N_2 partial pressure. As a consequence, four samples deposited at vacuum, 400 pa, 600 pa and 800 pa were selected for characterization.

1. XRD results

Structural properties of films were investigated with a X-ray diffractmeter (XRD-6000, Shimadzu Corporation). XRD patterns were measured over the range of 2θ = 20–80°. Fig. 2 shows the XRD patterns of samples deposited at different pressures. It is worth to mention that crystalline AlN has two types of lattice structures: hexagonal and cubic ones [18]. Most of the current applications are based on the hexagonal lattice structure, because AlN is a wide band-gap material with this structure. The diffraction peaks observed at 33.2°, 36 °, 37.9 °, 59.4 ° and 71.4° corresponding to (100), (002), (101), (110) and (112), of hexagonal AlN (pdf no.: 25-1133). Apparently, polycrystalline AlN peaks were observed in the sample deposited in vacuum. In which, orientation (100) is predominated as compared to other orientations. AlN (100) peak was also observed both in the samples deposited at higher N_2 partial pressure of 400 and 600 pa. It reveals that all the deposited films with crystal structure are predominantly oriented along the (100) direction. However, the intensive decreasing intensity and broadening of (100) peaks from samples deposited in vacuum to the samples deposited at higher pressure

indicates either an amorphous phase, or decrease in crystallinity and increase in internal tension (higher the intensity, lower the width, better the crystallinity and lower stress) [19]. Finally, (100) peak was totally disappeared when the N_2 partial pressure climbed up to 800 pa. Furthermore, (002) peak wasn't observed at high partial pressure. The appearance of (002) peak indicates the deposited films were grown along c-axial direction, which is perpendicular to the substrate surface. Electromechanical coupling coefficient, dielectric losses and acoustic losses of the piezoelectric thin film strongly influence the FBAR performances and AlN layers must be c-oriented [5]. The film achieved at low pressure is quite in accord with this requirement. It is attributed that the mean free path of the constituent particles of plasma is higher and hence higher kinetic energy can be imparted to the deposited atoms/ions and molecules at the growing surface of the thin film. Particle bombardment with sufficient kinetic energy results in augmented mobility of the deposited species thereby rearranging the film surfaces under equilibrium and filling the voids. The wurtzite phase of

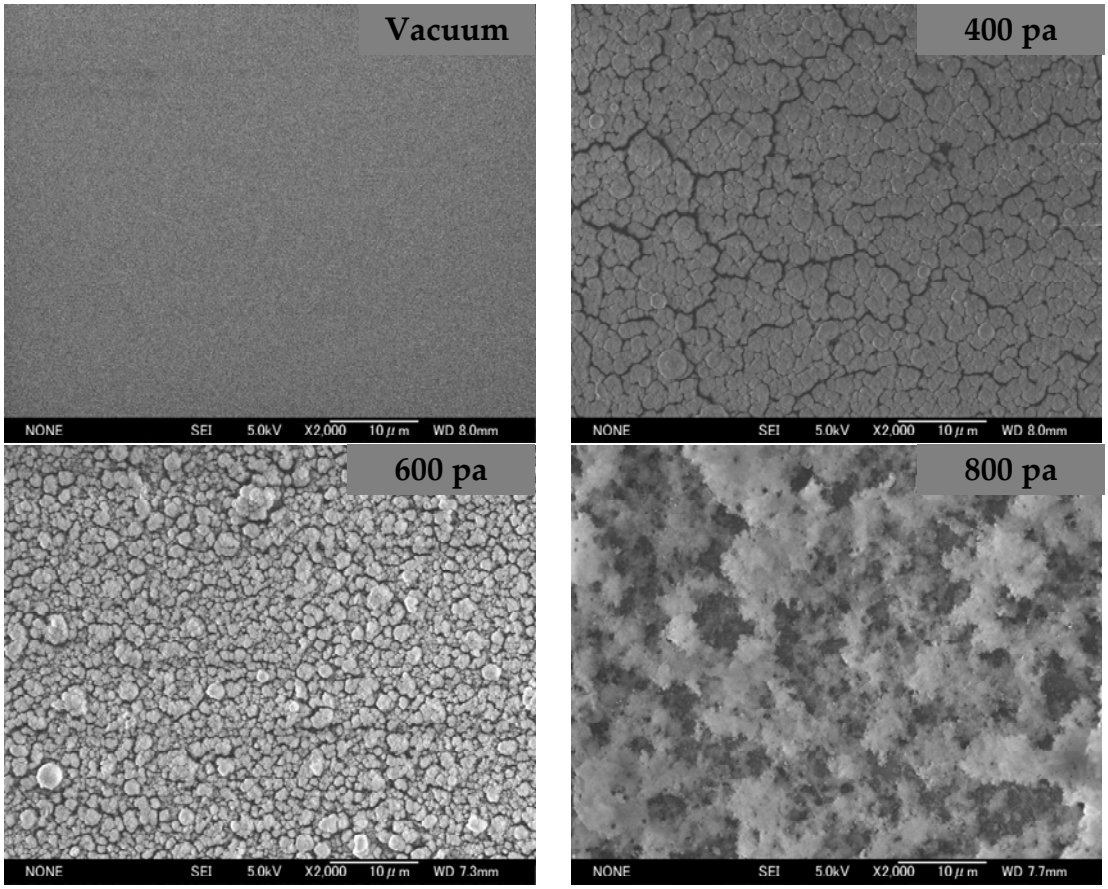

Fig.3. SEM images of as-deposited AlN samples.

AlN is more stable due to its close-packed stacking than the zinc-blended phase and the (0 0 2) orientation have the lowest surface energy [20–22]. As a result, islands corresponding to the lowest surface energy can nucleate and grow in an orientation parallel to the substrate to reduce its free energy favouring the growth along (0 0 2) orientation of AlN film. At higher pressures, increased number of collisions in gaseous phase made the particles in plasma lost most of there kinetic energy that can't afford enough energy to form crystal structure [20].

2. SEM results

Surface morphology of films was observed by a Field-Emission Scanning Electron Microscopy (SEM, JSM-6700F JEOL), which were shown in Fig.3. The surface of the sample deposited in vacuum is smooth with no visible features. At high nitrogen partial pressures, the surface is smooth with small inclusions on the surface. In addition, bigger agglomerate was observed at 600 pa as compared to that of

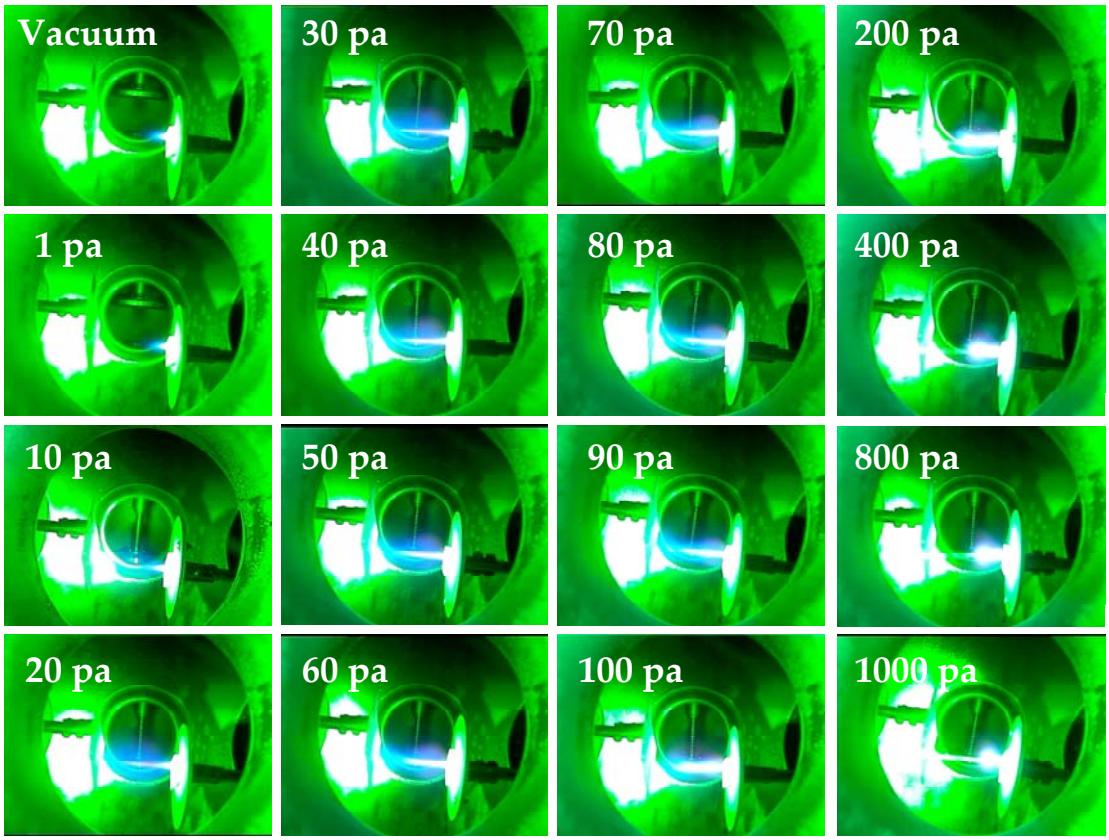

Fig.4. High-speed camera captured instant laser-induced plasma images under different partial pressures.

400 pa. Fluffy surface was inspected at 1000 pa.

3. High-speed camera

Instant states of laser-induced plasma were captured by high-speed camera outside chamber from view port, as shown in figure 4. In the vacuum stage, where the plume is very narrow and forward directed; almost no scattering occurs with the background gases. After the gas admission, the ions in the plume scattered with the gas and started to compress toward center direction and the shape emerged. After 200 pa, the plume began to shrink back to the surface of target. Finally, the plasma was almost confined near the surface of target. These results suggest a simple model for the PLD growth of thin films in the presence of a variable partial pressure in the chamber: the plume generated by the laser pulse from the target consists of Al, AlN and activated N and N ions. If λ_{mfp} of these species exceeds the target–substrate distance, the impingement of species with substantial energy is expected to enhance the surface diffusion rate. Lower pressures also decrease the formation of immobile surface dimers. In this case, a film that consists of oriented grains is formed. An increasing N partial pressure reduces the energy of the species by increasing the number of collisions in the gas phase. There is also an increase in nucleation sites due to increase Al–N reaction at the surface. Thereby, the surface diffusion length of ad-atoms is reduced. Consequently, films are composed of smaller grains, which is what we observe. At even higher N partial pressures, there is a further increase in nucleation sites, which reduce the surface diffusion length further [21].

Conclusion

In summary, influence of partial pressure on AlN film formation was systematically studied. Poly-crystalline hexagonal AlN was formed under room temperature. It is observed that orientation of deposited AlN thin films changes from (0 0 2) preferred orientation at low N_2 pressure to (1 0 0) preferred orientation at high N_2 pressure. Surface morphology of deposited films was dependent on N_2 pressure. It is found that average particle size increases with N_2 pressure and nanostructured growth of AlN (0 0 2) thin films through reactive pulsed laser deposition can be achieved at low N_2 pressure. It is believed that the increase in particle size with N_2 pressure is due to coagulation of particulates at higher pressure.

Reference

1) R.D. Vispute, J. Narayan, J.D. Budai,

Thin Solid films 299 (1997) 94-103.
2) K.M. Lakin, J.S. Wang, Appl. Phys. Lett. 38 (1981) 125.
3) S.H. Lee, K.H. Yoon, J.-K. Lee, J. Appl. Phys. 92 (2002) 4062.
4) Morito Akiyama, Yukari Morofuji, Toshihiro Kamohara, Keiko Nishikubo Masayoshi Tsubai, Osamu Fukuda, and Naohiro Ueno, Journal of Applied Physics 100, 114318 (2006).
5) C. Cibert, M. Chatras, C. Champeaux, D. Cros, A. Catherinot, Applied Surface Science 253 (2007) 8151–8154
6) Kok-Wan TAY, Cheng-Liang HUANG and Long WU, Japanese Journal of Applied Physics Vol. 43, No. 3, 2004, pp. 1122–1126
7) K. Tsubouchi, N. Mikoshiba, IEEE Trans. Son. Ultrason. 32 (1985) 634.
8) A.J. Shukus, T.M. Reeder. E.L. Paradis, Appl. Phys. Lett. 24 (1974) 155.
9) G. Radhakrishan. J. Appl. Phys. 78 (1995), p. 6000.
10) S. Wang and K.M. Lakin. Appl. Phys. Lett. 40 (1982), p. 308.
11) C. Caliendo, F. Saggio, P. Verardi, E. Verona, IEEE Int. Ultrason. Symp. (1993) 249.
12) H. Okano, N. Tanaka, Y. Takahashi, T. Tanaka, K. Shibata and S. Nakano. Appl. Phys. Lett. 64 (1994), p. 166.
13) W.J. Meng, J.A. Sell, T.A. Perry, L.E. Rehn and P.M. Baldo. J. Appl. Phys. 75 (1994), p. 3446.
14) W. Zhang, Y. Someno, M. Sasaki and T. Hirai. J. Cryst. Growth 132 (1993), p. 337.
15) G.W. Auner, T.D. Lenane, F. Ahmad, in: M.A. Prelas, et al. (Eds.), Wide Band Gap Electronic Materials, Kluwer Academic Publishers, Dordrecht, 1995, p. 329.
16) K. Jagannadham, A. K. Sharma, Q. Wei, R. Kalyanraman, and J. Narayan, J. Vac. Sci. Technol. A 16.5., Sep/Oct 1998
17) H. Hobert et al. Vibrational Spectroscopy 19(1999)205–211.
18) S. Bakalova, A. Szekeres, A. Cziraki , C.P. Lungu , S. Grigorescu ,G. Socol , E. Axente , I.N. Mihailescu, Applied Surface Science 253 (2007) 8215–8219.
19) C. Ristoscu, C. Ducu, G. Socol, F. Craciunoiu, I.N. Mihailescu, Applied Surface Science 248 (2005) 411–415.
20) Gaurav Shukla, Alika Khare, Applied Surface Science 255 (2008) 2057–2062.
21) G.S. Sudhir, H. Fujii, W.S. Wong, C. Kisielowski, N. Newman , C. Dieker, Z. Liliental-Weber, M.D. Rubin, E.R. Weber, Applied Surface Science 127–129 (1998) 471–476

Generation of pulsed discharges in water using high-voltage double-pulsed voltages and its characterization

M. Kanemaru*, S. Sorimachi, S. Ibuka and S. Ishii

Department of Electrical and Electronic Engineering, Tokyo Institute of Technology
2-12-1, O-okayama, Meguro-ku, Tokyo, Japan

ABSTRACT

We discussed a pulsed discharge in a single gas bubble, which was generated using double pulsed voltages with variable time intervals. The development of gas bubbles was characterized by high-speed photography and time-resolved optical emission spectroscopy. Gas bubbles were created by the discharges and stayed for approximately 400 μs, which was affected by the discharge energy. Electrode erosion due to the discharge with and without a gas bubble was investigated.

(key words : double-pulsed voltages, gas bubble, water, electrical discharge machining,)

Ⅰ. Introduction

Plasma processing involving liquid phases is widely used in a variety of applications, such as biomedical processes [1], material processes [2-4], dielectric breakdown [5], and sterilization in water treatment [6]. Electrical discharges in liquids have been studied from the viewpoint of the dielectric strength in high-voltage engineering for a long time. Pulsed arc discharges between microgaps in liquid include complex physical phenomena, such as the heating of the electrode surface, streamer formation, the formation of bubbles, the creation of ions, electrons, and radicals, and their interaction with liquids. The characteristics of pulsed discharges in liquids are different from those of the discharges in gases, namely, they are highly reactive because they are composed of species generated from liquids and electrode metals.

Pulsed microdischarges in liquids are closely related to micro-electrical discharge machining(Micro-EDM). Micro-EDM is one of the effective methods for machining the miniature size parts or extremely difficult-to-cut materials such as tungsten carbide [7]. However, few studies have been done on the characterization of discharge itself [8]. The machining processes and the limiting of minuteness need to be understood by examining the discharge between microgap in liquid.

In this study, we discussed a pulsed discharge in a single bubble, which was generated using double pulsed voltages with variable time intervals. The gas bubble was created by the discharge and stayed for approximately 400 μs that was affected by the discharge energy. Bubbles are considered to play an important role in the micro-EDM, in which repetitive high-voltage pulses are used and a number of bubbles are created in the discharges. The lifetime of the bubbles affects the characteristics of repetitive discharges. To discuss this issue, we used the double

pulsed microdischarges. The first microdischarge was used to generate the bubble, in which the second one was used to create plasmas. The temporal and spatial development of the gas bubbles and discharge in them was characterized by high-speed photography. Excitation temperature and electron density were obtained using optical emission spectroscopy.

Ⅱ. Experimental apparatus

A schematic of the experimental setup for the double pulsed microdischarges in distilled water is shown in figure 1. A tungsten wire electrode of 100 μm diameter was placed above a copper rod electrode of 3 mm diameter. A part of the lateral side of the rod was made flat to obtain a plane electrode surface. The gap length was 500 μm.

The double-pulsed microdischarges with variable interval times were operated using two discharge circuit units consisting of a capacitor with a gap switch connected in parallel to the discharge electrodes. The first discharge for generating a bubble, which originated between the electrodes, was powered by a capacitor of 800 pF. The second one for characterizing the discharge development in the bubble was powered by a capacitor of 2000 pF. The interval time of the discharges was adjusted by changing the timing to trigger the gap switches.

Gap voltage and discharge currents were monitored

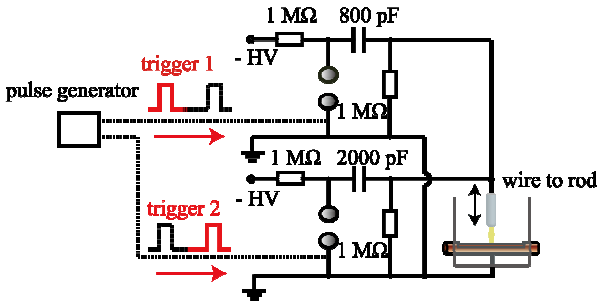

Figure. 1. Experimental setup.

using a high-voltage probe (Tektronix P6015A) and a current transformer (Pearson 110), respectively. The temporal and spatial development of the bubble was observed with a framing camera (Specialized imaging. SIM). Time-resolved spectral measurements are made with a monochromator (Acton SpectraPro) fitted with an intensified CCD camera (DH734-18U-03, Andor Technology). The timing of the imaging system was precisely controlled by a delay generator (Stanford Research, DG535). The crater on the surface of the copper plate electrode created by the pulsed discharge was observed using a scanning electron microscope (SEM).

Ⅲ. Results and discussion

1. Development of a gas bubble

Time-resolved observation of bubble dynamics was carried out using the high resolution framing camera with an exposure time of 5 μs. The bubble generated by the first pulsed discharge with an energy of 40 mJ developed in two successive stages, namely its expansion and contraction having a hemispherical shape as shown in figure 2. The image at t = 0 (s) was taken immediately before the discharge, the pulsed current of which decayed within 1 μs. The thin discharge channel heated the water, which vaporized and formed the bubble between the gaps of 500 μm. The expanding spherical bubble reached its maximum radius of 2.5 mm at 200 μs. Then, the bubble contracted to the minimum detectable size at 400 μs and expanded again to form irregular shapes at 450-500 μs. This successive expansion is due to the increase in pressure in a gas bubble after the bubble shrank. The pressure increased with decreasing bubble size because noncondensable gases existed in the bubble. The temporal change in bubble radius for the capacitor energy range from 25 to 200

mJ is shown in figure 3. In this case, the cube of the maximum radius is directly proportional to the energy, because the expansion of hemispherical bubble is originated by the input electrical energy released within 1 μs. In other words, the maximum bubble volume is determined by capacitor energy, but it is varied also by gap distance, electrode size and so on.

The evolution of the bubble generated by discharges is described by a theoretical model of bubble radius evolution [9]. The bubble lifetime was calculated by using the Rayleigh relation,

$$\tau = 2\cdot(0.915)\cdot R_m \cdot \sqrt{\frac{\rho}{p}} \qquad (1)$$

R_m is the maximum radius of bubbles, ρ is the water density and p is the pressure. Eq. (1) was derived assuming an infinitely-large volume of uniform incompressible liquid. The pressure is the one at infinite distance. We took the pressure as 1 atmosphere. Figure 4 shows the bubble lifetime as a function of capacitor energy for both experimental and theoretical results. It increases with increasing capacitor energy. The theoretical result was almost the same as the experimental one with an accuracy of 10 %.

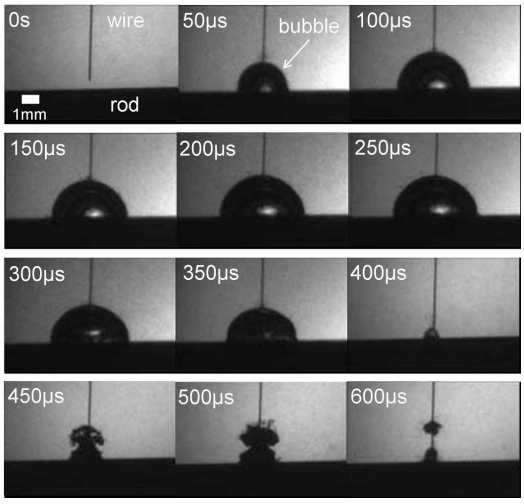

Figure. 2. Temporal evolution of bubble generated by a pulsed discharge in water.

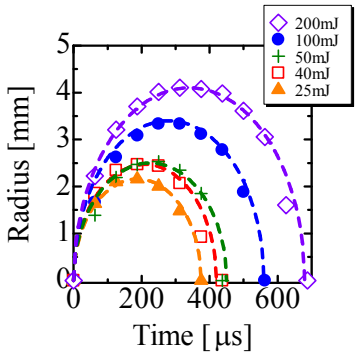

Figure. 3. Temporal changes of bubble radius for different capacitor.

2. Pulsed microdischarges in a gas bubble

Bubbles are used as the cavities of plasma microreactors surrounded by water. To make the situation simple, we adopted the second pulsed discharge with a variable interval time. A visible light image of the discharge developed in the bubble, which was generated by the first microdischarge with an energy of 40 mJ, is shown in figure 5(a). The interval time was set to 200 μs, in which the bubble radius reached its maximum. The bubble radius was not affected by the second discharge, which occurred in ambient gases. The temporal changes in gap voltage and discharge current shown in figure 5(b)

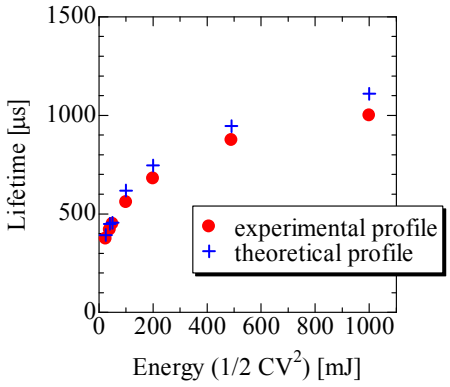

Figure. 4. Bubble lifetime as a function of capacitor energy.

were similar to those for the discharge in air. They, however, decayed within one cycle for the discharge in water.

Optical emission spectroscopy was conducted for the discharge. Figure 6(a) shows the temporal changes of CuI lines at 510.55, 515.32, 521.82 and 529.25 nm. Figure 6(b) shows that of the H_α line at 656.28 nm. In both figures, the spectral intensities were normalized to those of the CuI line at 521.82 nm and the H_α line at 656.28 nm. In contrast to the discharge in water, the continuum radiation was not observed for the first 1.5 μs, during which the discharge developed in the bubble. The continuum radiation appeared for the discharge with an interval time of more than 700 μs, in which the bubble contracted and disappeared. The continuum radiation is usually observed at the early stage of discharges in liquids [10]. The mechanism of continuum radiation is not fully understood because it involves complex discharge processes and occurs in a short duration of the order of a few microseconds.

The excitation temperature T_{exc} was determined from the measured copper atomic-line intensities, assuming that the population of energy levels follows the Boltzmann distribution law [11]. The electron number density N_e was determined by the Stark broadening of the H_α line at 656.28 nm [12]. Figure 7 shows the temporal changes in T_{exc} and N_e for the period of 2 μs, during which the second discharge developed and decayed. T_{exc} and N_e decreased from 11500 to 9000 K and from 2×10^{17} to 1×10^{16} cm^{-3}, respectively.

The physical and chemical states in the bubble changed as the bubble expanded and contracted. The interval time affected the second discharge in the bubble. Figure 8 shows T_{exc} and N_e as a function of interval time ranging from 20 to 380 μs. The bubble radius is shown as a reference. With an increase in interval time, T_{exc} gradually decreased until 200 μs because the gas pressure decreased as a result of bubble expansion. Subsequently, it increased again to 10000-11500 K. N_e increased similarly in the range of

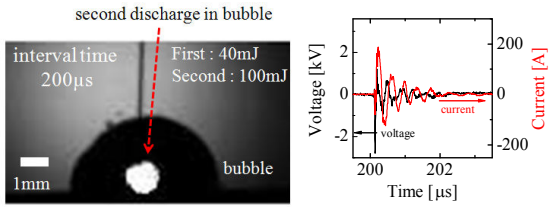

(a) (b)

Figure. 5. Pulsed microdischarge in a bubble, (a) visible photograph and (b) gap voltage and discharge current.

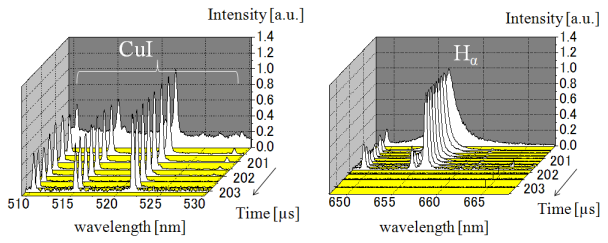

(a) (b)

Figure. 6. Time-resolved spectra for second pulsed discharge in bubble for ranges of (a) 510-530 nm and (b) 648-668 nm.

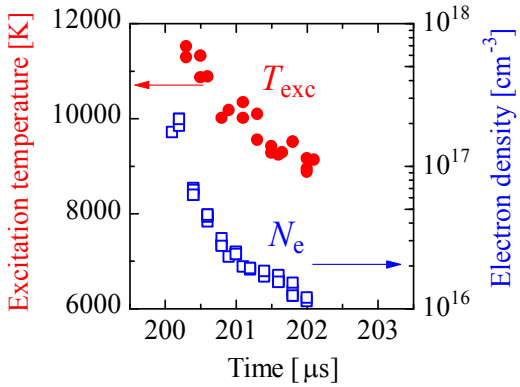

Figure. 7. Temporal changes in excitation temperature T_{exc} and electron density N_e for second pulsed discharge in bubble. The abscissa represents the elapsed time from the initiation of bubble formation.

3.5×10^{16} to 1.5×10^{17} cm^{-3}. The interval time affected the plasma generated in the second discharge significantly.

We characterized the electrode erosion as a result of the second discharges in the bubble or water by varying the interval time. The interval time was adjusted to 100 μs and 1000 μs for the discharges in the bubble and water, respectively. The electrode erosion is also related to the application of micro-EDM. Figure 9 shows typical images of the electrode erosion taken using the SEM for the discharges in the bubble and water. The first discharge for bubble generation was powered by the capacitor with an energy of 40 mJ. The electrode damage caused by this discharge was negligible owing to the low input energy. The second discharge was powered by the capacitor with an energy of 1000 mJ. The absence of craters and only a slight alteration in the color of the surface of the electrode, which often appeared in pulsed discharges in air, were observed for the second discharge in the bubble. On the other hand, a crater with a diameter of 100 μm, which was almost equal to the wire-electrode diameter, was observed in the discharge with an interval time of 1000 μs. The experimental data of the effect of the second discharge on the electrode erosion are summarized in Figure 10. The difference in crater size is explained by with or without bubbles in water when the second pulsed discharge develops. In the case of an interval time of 1000 μs, the pulsed discharge had to develop between the electrodes in water because the bubble with the lifetime of 400 μs

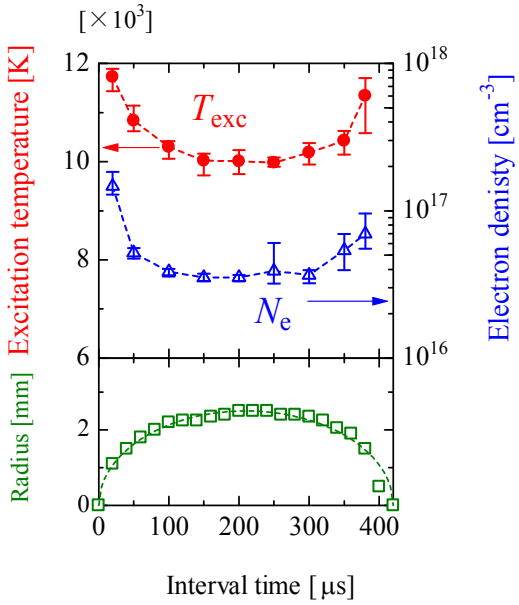

Figure. 8. Excitation temperature T_{exc} and electron density N_e values at different interval times. The bubble radius is shown as a reference of interval time.

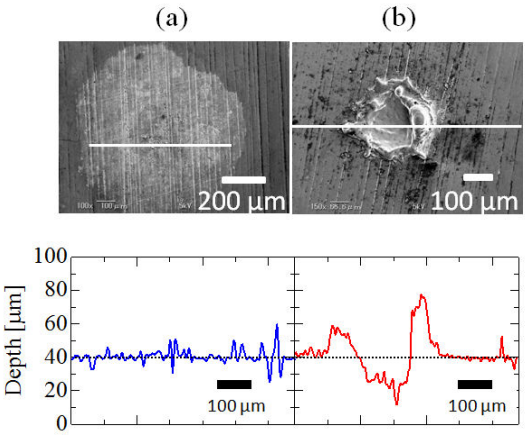

Figure. 9. Images of electrode erosion and depth of the eroded surface for discharges in (a) bubble (interval time: 200 μs) and (b) water (interval time: 1000 μs). Depth data were obtained by scanning along the white line.

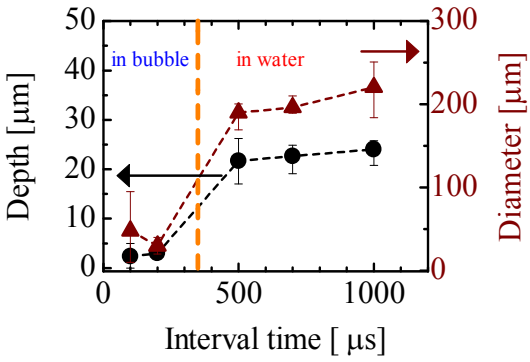

Figure. 10. Depths and diameters of eroded regions for the discharge in bubble (●) and water (▲), as a function of interval time.

already disappeared completely. The current density of the discharge is higher than that for the discharge in the bubble owing to the cooling effect of the surrounding water. This causes the significant effect of heating on the electrode material compared with that in the case of an interval time of less than 400 μs.

Ⅳ. Conclusion

We applied double-pulsed voltages successively with variable interval time to examine the contribution of bubble in the micro-EDM that uses repetitive high-voltage pulses. The excitation temperature and the electron number density influenced on the interval time. From the evaluation of electrode erosion, the frequency of the discharges for efficient processing depended on the existence of the bubble in water.

Acknowledgments

This work was supported by a Grant-in-Aid for JSPS Fellows (21-7799) from the Japan Society for the Promotion of Science (JSPS).

References

[1] Sun Y, Xiao S, White J A, Kolb J F, Stacey M and Schoenbach K H 2007 Compact, Nanosecond, High Repetition Rate, Pulse Generator for Bioelectric Studies IEEE Trans Dielect Elect Ins 14 863-870
[2] Parkanskya N, Alterkopa B, Boxmana R L, Goldsmitha S, Barkay Z, Lereah Y 2005 Pulsed discharge production of nano- and microparticles in ethanol and their characterization Pow Tech 150 36-41
[3] Cho C H, Park S H, Choi Y W, Kim B G 2007 Production of nanopowders by wire explosion in liquid media Sur Coat Tech 201 4847-4849
[4] Saito N, Hieda J, Takai O 2009 Synthesis process of gold nanoparticles in solution plasma Thin Sol Films 518 912-917
[5] Schoenbach K H, Kolb J F, Xiao S, Katsuki S, Minamitani Y and Joshi R P 2008 Electrical breakdown of water in microgaps Plas Sour Sci Tech 17 024010 (10pp)
[6] Sato K and Yasuoka K 2008 Pulsed Discharge Development in Oxygen, Argon, and Helium Bubbles in Water IEEE Trans. Plasma Sci 36 1144-1145
[7] Jahan M P, Wong Y S and Rahman M 2009 A study on the quality micro-hole machining of tungsten carbide by micro-EDM process using transistor and RC-type pulse generator J Mater Proc Tech 209 1706-1716
[8] Schumacher B M 2004 After 60 years of EDM the discharge process remains still disputed J Mater Proc Tech 149 376-381
[9] Jomni F, Denat A and Aitken F 2009 The dynamics of microscopic bubbles in viscous insulating liquids J Appl Phys 105 053301 (9pp)
[10]Descoeudres A, Hollenstein C, Walder G, Demellayer R, and Perez R 2008 Time- and spatially-resolved characterization of electrical discharge machining plasma 17 024008 (10pp)
[11] Hafez M A, Khedr M A, Elaksher F F and Gamal Y E 2003 Characteristics of Cu plasma produced by a laser interaction with a solid target Plas Sour Sci Tech 12 185-198
[12] Gigososy M A and Cardenoso V 1996 New plasma diagnosis tables of hydrogen Stark broadening including ion dynamics J Phys B: At Mol Opt Phys 29 4795-4838

HIGH REPETITIVE PULSED GLOW MICRODISCHARGES WITH A MINIATURE HELIUM GAS FLOW

Jun Kikuchi, Koichi Igarashi, Naoaki Yoshida, Takaaki Muto,
Shinji Ibuka, and Shozo Ishii

Department of Electrical and electronic Engineering,
Tokyo Institute of Technology,
2-12-1 S3-9 Ookayama, Meguro-ku, Tokyo 152-8550, Japan.

ABSTRACT

Atmospheric pulsed glow microdischarges, which were generated with double-pulsed high voltages using a miniature helium gas flow, were characterized by varying helium gas flow rate and pulse interval of the pulsed voltages. The helium gas flow rate affected significantly the development of pulsed discharges. We developed a double-pulsed voltage generator with the variable pulse interval to examine the effect of the first discharge on the second one in high repetitive double-pulsed discharges. When the pulse interval was less than 200 μs, the second pulsed discharge took place with a breakdown voltage of less than 1.0 kV. The high repetitive operation is effective way of generating the atmospheric pulsed microdischarge with low-pulsed voltages.

I. Introduction

Atmospheric glow discharges have the potential of various applications such as the destruction of toxic compounds, the detection of trace contaminants, the depositing of films and the surface process with simple and low cost systems because these systems do not require expensive vacuum pumps [1, 2]. However, the atmospheric condition makes a mean free path short and the transition to arc discharge easily.

To obtain atmospheric glow discharges, one has to pay attention to discharge electrodes, input power, and feeding gas control. Recently, microplasmas with a size of 10 – 1000 μm are used to generate the stable atmospheric glow discharge powered by direct current (DC) voltages. Energy balance between electrical power input and energy loss from the surface of the plasma is established, because the plasma volume is so small that a specific surface area is large [3, 4]. However, the DC voltage operations cannot supply high power to the discharge because the discharge current is limited within a few mA to prevent the glow-to-arc transition.

The pulsed voltage operation can provide high instantaneous power. If the applied voltage is made zero before the inception of glow-to-arc transition, the atmospheric pulsed glow discharge develops. Adjusting the duty ratio of pulsed voltage, one can control the particle number densities of electron, ion, and radical to be pertinent value for the applications. Radical number densities depended on instantaneous input power [5]. Pulsed voltages having a short pulse width of 10 ns can generate high-density plasmas with a low power-consumption and a high efficiency [6]. We previously obtained an atmospheric transient glow microdischarge powered by fast high-voltage pulse-trains, which were generated using a pulse generator with a nonlinear transmission line, between the nozzle and metal plate electrodes with a miniature gas flow [7, 8]. It was confirmed that the miniature helium gas flow, a short pulsed-voltage of less than 1.0 μs and a smooth surface of a cathode were effective for generating the glow microdischarge.

However, we have not understood how the electrode structure and the pulsed-voltage waveform affect the atmospheric transient glow discharge yet. It is necessary to examine the effects of the helium gas flow rate and the preceding pulsed discharge on repetitive pulsed discharges. We characterized the atmospheric transient glow discharge by observing a discharge development, conducting optical emission spectroscopy, and measuring the electron number density. We developed a double pulsed voltage generator, which generated two successive burst pulses with variable pulse intervals, to discuss the effect of afterglow plasma resulted from the previous pulsed discharge,.

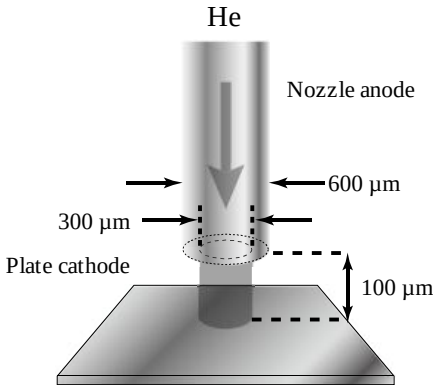

Figure 1 The nozzle anode and the plate cathode.

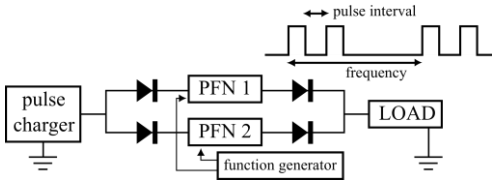

Figure 2 The double-pulsed voltages generator.

II. Experimental setup

Figure 1 shows a nozzle-to-plate electrode system for the pulsed glow microdischarges. The inner and outer diameters of the nozzle anode were 300 μm and 600 μm, respectively. The surface of the plate cathode was polished with an abrasive compound to suppress the glow to arc transition. Both the electrodes, made of stainless steel, were placed on micro positioning stages, which enabled them to move independently. The separation between the nozzle anode and the plate cathode was 100 μm. The helium gas flow rate out of the nozzle anode was regulated with a mass flow controller, which adjusted the maximum flow rate of 500 sccm.

We previously reported the generation of pulsed glow discharge with the fast high-voltage pulse trains generated by a nonlinear transmission line [7]. In this method, however, it was difficult to control the pulse width and the pulse interval. We developed a double-pulsed high-voltage generator in which the pulse width and the pulse interval were varied easily. The double-pulsed voltages, consisted of two successive rectangular high-voltage pulses, were generated using two pulse forming networks (PFNs) as shown in Figure 2. The PFN outputs are connected

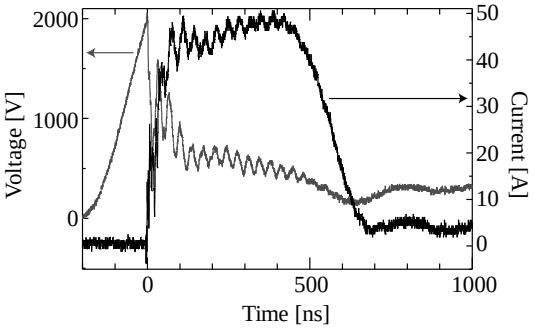

Figure 3 Typical voltage and current waveforms of atmospheric pulsed glow discharges.

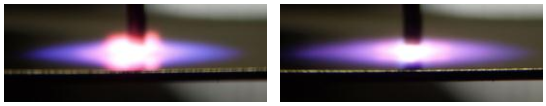

(a) 180 sccm (b) 400 sccm

Figure 4 Time integrated images of pulsed glow discharges.

to the nozzle anode in parallel via semiconductor diodes (STTA812D: breakdown voltage1200V, four series connection) to decouple each pulse of two Blumlein type PFNs with a characteristic impedance of 50 Ω and a pulse width of 600 ns. Their output voltages are equal to the charging voltage, which is 2.0 kV in this experiment. We varied the switching time of the PFNs, the pulse interval, up to 300 μs. The double-pulsed voltages were operated with a repetition rate of 100 Hz.

We measured the gap voltage between electrodes and the pulsed discharge current by a high voltage probe, Tektronix P6015A, and a current probe, Pearson 2878, respectively. Visible light images of the discharges were recorded by a digital camera, OLYMPUS E-410, with microscope lens, Edmund optics VZM 450 that had variable optical magnification of 0.7 - 4.5 times. Temporal behavior of the discharge development was observed by an image intensified charge-coupled device (ICCD) camera with a minimum exposure time of two ns, Andor DH734 18U-03. Optical emission spectroscopy was conducted to measure the electron number density. We obtained the electron number density using Stark broadening of the hydrogen Balmer system (486.1 nm) [5].

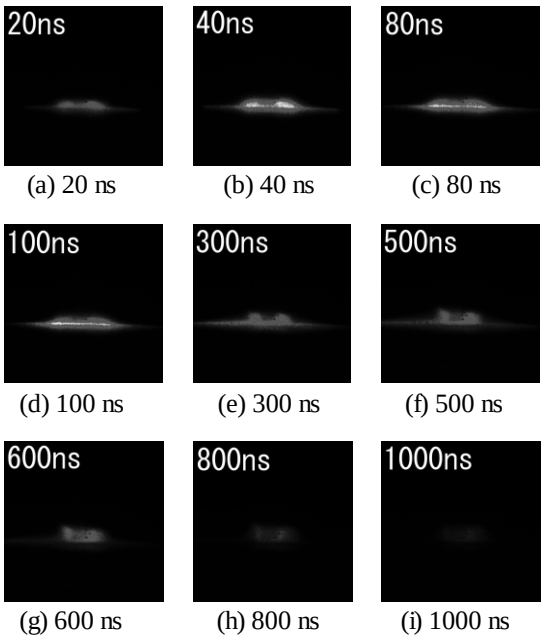

(a) 20 ns (b) 40 ns (c) 80 ns

(d) 100 ns (e) 300 ns (f) 500 ns

(g) 600 ns (h) 800 ns (i) 1000 ns

Figure 5 The development pulsed glow discharge with the He gas flow rate of 180 sccm.

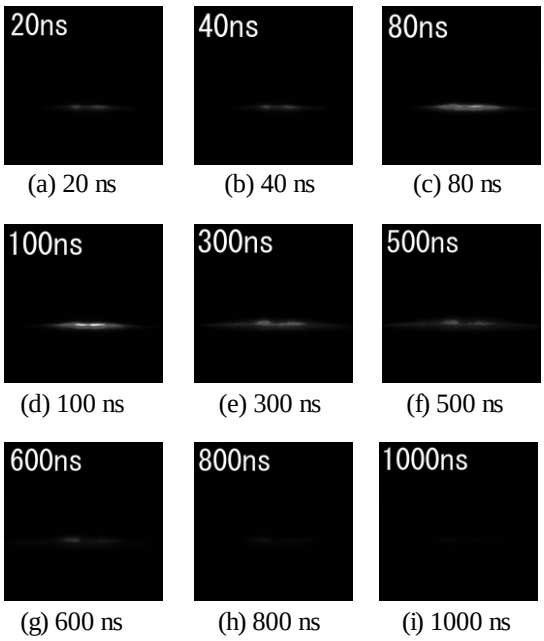

(a) 20 ns (b) 40 ns (c) 80 ns

(d) 100 ns (e) 300 ns (f) 500 ns

(g) 600 ns (h) 800 ns (i) 1000 ns

Figure 6 The development pulsed glow discharge with the He gas flow rate of 400 sccm.

III. Results and Discussions

A. Effect of the He gas flow rates

Atmospheric pulsed glow discharge was characterized by varying the He gas flow rate and the gap separation. Figure 3 shows typical waveforms of a gap voltage and a discharge current for the discharge with an electrodes separation of 100 μm and a repetition frequency of 100 Hz. A pulsed glow discharge developed because the gap voltage kept at approximately 500 V. Time integrated images taken by varying the He gas flow rate are shown in Figure 4. The optical emission covered not only the plate cathode but also the tip of nozzle anode for the discharge at 180 sccm.

The discharge developments with the He gas flow rate of 180 and 400 sccm are shown in Figure 5 and Figure 6, respectively. The exposure time of each image is 5 ns and frame timings correspond with the time in Figure 3. When the He gas flow rate was 180 sccm, the visible light near the nozzle tip appeared at 300 ns. The light lasted even after 700 ns, at which the pulsed current decreased. On the other hand, there was no emission near the nozzle tip at 400 sccm.

To discuss the difference between the two cases, the temporal change in intensity of the nitrogen molecular line (N_2 Second positive band: 337 nm), the nitrogen ionic line (N_2^+ First negative band: 391 nm), and He atomic line (587 nm), which are useful lines to recognize atmospheric discharges using helium, was measured. Figure 7 shows the gap voltage, discharge current, and the intensity of lines for the discharge with 180 sccm and 400 sccm. There appeared significant rise in the N_2 and N_2^+ emission lines at a breakdown phase. On the other hand, both of He emission intensities rose slowly. At 200 ns, however, the temporal variation of the He emission at 180 sccm differed from that at 400 sccm, for which the increase of the He emission ceased at 400 ns. The He emission at 180 sccm, however, continued to increase and reached its peak at the fall of the discharge current. The emission observed near the nozzle tip in Figure 5 originated from the He emission at the decay phase.

The relation between helium gas-flow rate and time integrated emission intensity of N_2 line, that of N_2^+ line, and their intensity ratio is shown in Figure 8. N_2^+ is excited through the processes of the penning ionization of a metastable He and N_2 and a charge transfer of He ion and N_2 [9, 10]. The ratio of N_2^+ to N_2 indicates the generation of metastable He atoms and a increase of electron temperature because the formation of metastable He atoms is necessary to have electrons, which must have higher energy than an excitation energy of N_2 [9]. The ratio has its peak

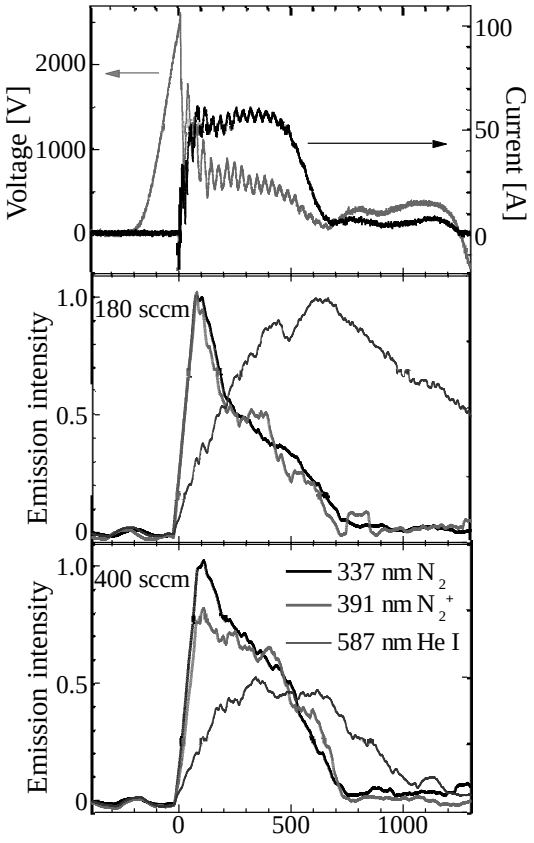

Figure 7 Temporal changes of emission spectral lines (Upside; voltage and current, middle; 180 sccm, down; 400 sccm).

at 180 sccm. This result supports that the optimum He gas flow rate realizes higher electron temperature.

B. Pulsed glow microdischarges using double-pulsed voltages

To discuss the effect of the preceding discharge, the double pulsed glow discharges were operated with the variable pulse interval. Figure 9 shows temporal changes of the emission line intensities for the pulse intervals of 1.0 μs and 100 μs when the He gas flow rate was 180 sccm. The emission at the first pulsed discharge was similar to that single-pulsed discharge. If the pulse interval was 1.0 μs, radicals and charged particles generated by the first pulsed discharge remained and affected the development of the second discharge. The emission intensities for the second discharge were different from those for the first one. The emission intensities of N_2 and N_2^+ lines are less than half of those for the first discharge. The He emission intensity increased slowly and reached its peak at the beginning of decay of the current.

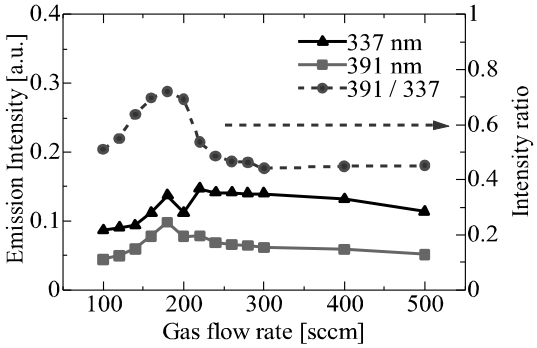

Figure 8 Emission intensities of N_2 and N_2^+ lines and intensity rate (N_2 / N_2^+) dependent on the He gas flow rate.

When the pulse interval was 100 μs, the temporal change of the emission intensities for the second discharge was almost similar to those for the first one. However, there remain a small fraction of residual active particles in the gap because N_2 and N_2^+ line intensities are weak.

Figure 10 is the dependence of breakdown voltage for the second discharge, which was affected by residual radicals and charged particles, on the pulse interval. The data points were determined by averaging three or five measurements. Their standard deviation is illustrated as the error bars. The data for the single-pulsed discharge is taken at the pulse interval of 10 ms, which is equivalent to the repetition frequency of 100 Hz. Both the breakdown voltages for the gas flow rates of 180 and 400 sccm were similar at the pulse interval of less than 10 μs. When the pulse interval was 10 - 100 μs, the breakdown voltages for 180 sccm were lower than those for 400 sccm. An increase of the He gas flow rate attributed diffusion of residual active particles to be fast. The breakdown voltages exceeded 1000 V for the pulse interval of above 200 μs. This means that the dielectric strength increased significantly. The breakdown voltages for the second discharge became less than 1 kV at the repetition frequency of more than 5 kHz, which corresponded to the pulse interval of 200 μs. In other words, pulsed glow discharges can be obtained applying pulsed voltages less than 1.0 kV as long as the repetition frequency is more than five kHz.

The effect of successive discharge in highly repetitive pulsed discharges was discussed from the view point of the temporal change in electron number density. The electron number densities of the discharge were obtained by the Stark broadening of

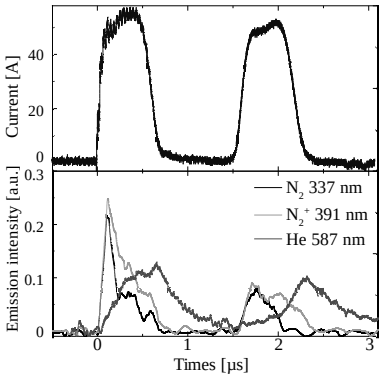

(a) The pulse interval of 1.0 μs

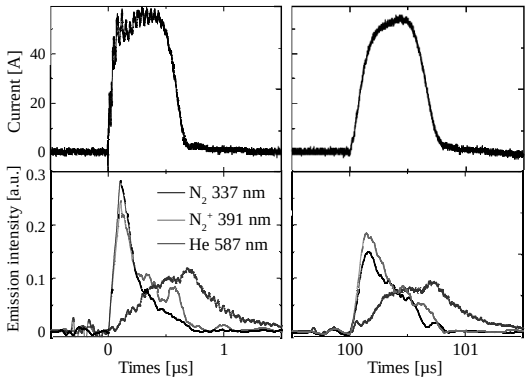

(b) The pulse interval of 100 μs

Figure 9 Temporal changes of current waveform and N_2, N_2^+ and He emission lines at 180 sccm.

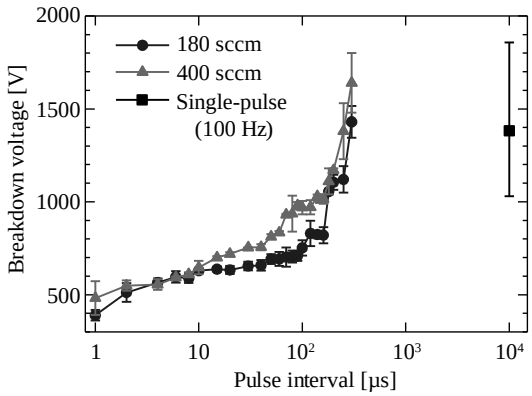

Figure 10 The brakedown voltage of the second discharge.

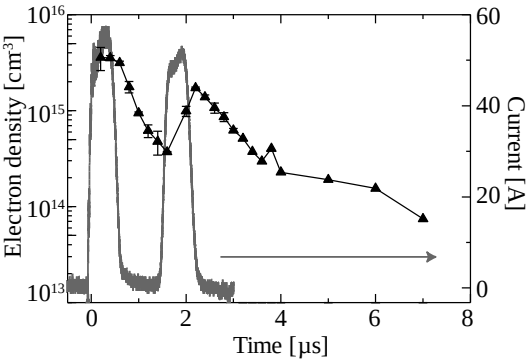

Figure 11 The temporal change of an electron number density with the pulse interval of 1.0 μs.

the hydrogen Balmer system at a time resolution of 200 ns. They decayed slowly after the current became zero fall as shown in Figure 11. If the second pulsed voltage is applied within the pulse interval of 1.0 μs the electron number density decays within 10 percent range. An average electron number density of more than 10^{15} cm^{-3} will be obtained in the repetitive pulsed discharge with the repetition rate of 1.0 MHz.

IV. Conclusion

We characterized the effect of the He gas flow rate on the atmospheric pulsed glow discharges. If the He gas flow rate was 180 sccm and the gap separation 100 μm, the He atomic emission line intensity had its peak. A higher electron temperature seems to be realized by optimizing the relation of the He gas flow rate and the gap separation.

It was also verified that the first pulsed discharge affected the second one in the double-pulsed discharge, of which the pulse interval was varied to 300 μs. Since the breakdown voltage of the second pulsed discharge became less than 1.0 kV setting the pulse interval less than 200 μs, the repetitive pulsed discharge can develop with 1.0 kV pulsed voltages having the repetition frequency of more than five kHz. Furthermore, 1.0 MHz repetition frequency has a potential of achieving a high average electron number density, which exceeds 10^{15} cm^{-3}.

References

1) K H Becker, K H Schoenbach and J G Eden, "Microplasma and applications", J. Phys. D: Appl. Phys, Vol. 39,pp.55-70 (2006).
2) J. Benedikt, K. Focke, A. Yanguas-Gil, and A. von Keudell, "Atmospheric pressure microplasma jet as a depositing tool", APPLIED PHYSICS LETTERS, Vol. 89, 25104 (2006).
3) T. Yokoyama, S. Hamada, S. Ibuka, K. Yasuoka and S. Ishii, "Atmospheric dc discharges with miniature gas flow as microplasma generation method", Journal of Physics, Vol. 38,

pp.1684-1689, (2005).
4) David Staack, Bakhtier Farouk, Alexander Gutsol and Alexander Fridman, “DC normal glow discharges in atmospheric pressure atomic and molecular gases”, Plasma Sources Sci. Technol., Vol. 17, 025013 (2008).
5) K H Becker, U Kogelschatz, K H Schoenbach and R J Barker, “Non-Equilibrium Air Plasmas at Atmospheric Pressure”, Institute of Physics Publishing (2005).
6) Michael A. Lieberman and Allan J. Lichtenberg, “Principles of Plasma Discharges and Materials Processing”, WILEY INERSCIENCE (2005).
7) S. Ibuka, K. Harada, J. Kikuchi, K. Igarashi, and S. Ishii, “Application for carbon materials production with atmospheric transient glow discharge in microgap electrode”, The Papers of Technical Meeting on Pulsed Power Technology, IEE Japan, PPT-07-39 pp.7-12 (2007). (in Japanease)
8) S. Ibuka, K. Harada, J. Kikuchi, K. Igarashi, and S. Ishii, “Application for carbon materials production with atmospheric transient glow discharge in microgap electrode”, The Papers of Technical Meeting on Pulsed Power Technology, IEE Japan, PPT-07-39 pp.7-12 (2007). (in Japanease)
9) S.D. Anghel, A. Simon, A.I. Radu, I.J. Hidi : “Spectroscopic characterisation of a cross-flow plasma jet”, Nuclear Instruments and Methods in Physics Research Section B: Beam Interactions with Materials and Atoms, Vol.267,No.2, pp.430-433 (2009)
10) R Rahul, O Stan, A Rahman, E Littlefield, K Hoshimiya, A P Yalin, A Sharma, A Pruden, C A Moore, Z Yu and G J Collins : “Optical and RF electrical characteristics of atmospheric pressure open-air hollow slot microplasmas and application to bacterial inactivation”, Journal of Physics D: Applied Physics, Vol.38, No.11, pp.1750-1759 (2005)

Electrical Conductivity Measurements of Warm Dense Matter with Semi-rigid Vessel

Takeshi Hosoi, Mitsuo Nakajima, Tohru Kawamura, and Kazuhiko Horioka*
Department of Energy Sciences, Tokyo Institute of Technology,
Nagatsuta 4259, Midori-ku, Yokohama, 226-8502, Japan

Thin wires were rapidly vaporized and ionized in a semi-rigid capillary by means of a current with ∼10kA-μsec pulse. The wires melted, evaporated and evolved to a high temperature plasma through a warm dense matter region. The semi-rigid capillary confined homogeneous plasma at least for a few micro-second level, which enabled measurements of the electrical conductivity in a well-defined condition as a function of density and input energy. Results indicated that the electrical conductivity has a minimum value around $1/30\rho_s$ (ρ_s:solid density) regardless of materials. Behaviors of the wire explosion in glass capillary were compared with those in sapphire capillary to examine effect of deformation of the vessel and also reliability of the experimental data.

Keywords: Warm Dense Matter, Wire Explosion, Electrical Conductivity, Capillary, Pulse-Power

I. INTRODUCTION

Figure 1 shows various state of matter in a density-temperature plane. As shown, all of the state of matter can be placed in the density-temperature diagram with logarithmic scale. In a relatively low temperature and high density regime(-10^5K, $10-10^4$ g/m^3), there is a state in which we have no appropriate models for equation of state and transport coe cients. Materials in this regime are characterized as Warm Dense Matter (WDM). When we deposit pulsed energy in a solid, the matter evolves from a solid to a high temperature plasma through a warm dense state. Therefore, when we quantitatively evaluate the evolution of matter in a broad parameter region, it is crucially important to characterize the WDM.

Properties of matter in the warm dense state are of interest concerning interiors of giant planet (e.g., Jupiter) and hydrodynamics of fuel pellet of inertial con nement fusion [1]. In the WDM, there are no appropriate models for the equation of state, and accurate experimental data of conductivity are lacking [2]. Exploration of the complex thermodynamical regime connects solid state physics and plasma physics.

Electrical conductivities have been investigated using wire explosion in water [4] [5]. However, in the previous study, the state of matter is not de ned well due to inde nite equation of state. One of the important points to evaluate the property of WDM is to make it in a well-de ned condition. We measured conductivity of wire plasma in a semi-rigid capillary. Electrical conductivity was measured as a function of internal-energy and density. Our nal goal is to make a scaling law, in particular, for electrical conductivity of WDM. To make the scaling law, it is important to estimate electrical conductivity under well de ned condition over a wide range of density-temperature region.

In this research, a cylindrical plasma in a warm dense state is produced by a wire explosion in a semi-rigid capillary driven by a fast pulse power generator. In case of the capillary discharge, the plasma is con ned in a condition with constant volume until the vessel is destroyed due to the abrupt pressure rise. If the plasma lls its inside volume completely, it is possible to con ne uniform sample of WDM and that enables us to measure input energy, material density, conductivity in a well de ned condition. As the container is transparent, capability of optical measurement from outside is also advantageous.

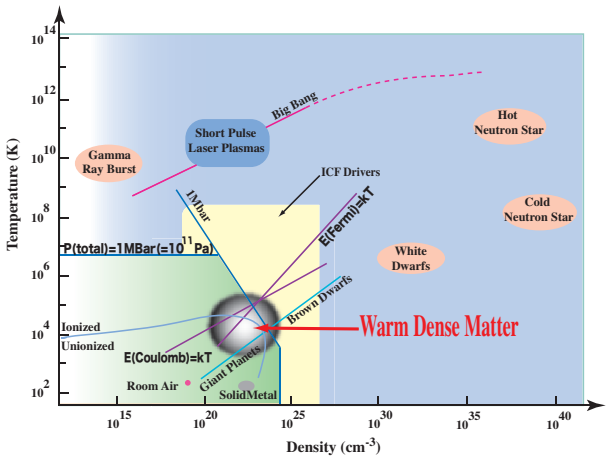

FIG. 1: State of matters in density-temperature plane

II. EXPERIMENTAL SETUP AND EVALUATION OF DISCHARGE CHARACTERISTICS

Figure 2 shows a schematic of the wire exploding process in semi-rigid vessel. A dense plasma made by explosion of thin wires rapidly lls the vessel with hydrodynamic time scale after the evaporation. Although the energy density of the plasma, i.e., the pressure, increases

*Electronic address: khorioka@es.titech.ac.jp

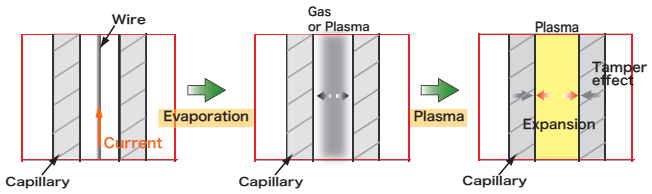

FIG. 2: Schematic diagram of wire explosion in semi-rigid capillary

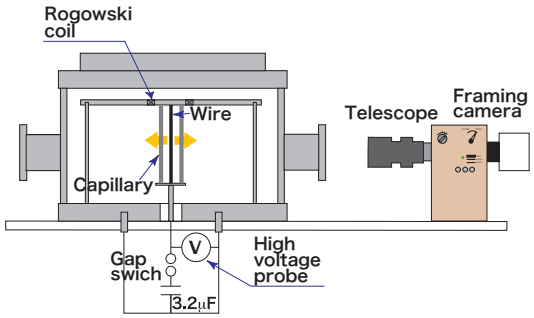

FIG. 3: Experimental arrangement for wire explosion in semi-rigid capillary discharge

with discharge time, the plasma is con ned in the vessel until the wall is destroyed by the shock wave re ection.

Figure 3 shows the experimental arrangement for WDM experiments. The experimental device consists of a cylindrically arranged condenser bank with C 3.2 F , a triggered spark gap switch, and a capillary discharge tube for the plasma generation. Typically we put 2 wires with 100 m in diameter and 20mm in length in the capillary. The quantity of wire corresponds to density of the interest; i.e., 1/30 ρ_s when the material lls the capillary. The discharge current was measured by a Rogowski coil and voltage was estimated by a high voltage prove together with inductive correction. The stray inductance(L) was estimated to be L $125nH$. We observed evolution of the wire plasma by a fast framing camera (IMACON 468).

Table I shows speci cations of the experimental device. Typically we operated the condenser bank with charging voltage of 10kV. We used Pyrex or Sapphire capillary to con ne the wire/plasma.

When the gap switch is closed, the pulsed current heats, evaporates and ionize the thin wire. During the evolution from solid wire to a high temperature plasma,

TABLE I: Specification of pulse power device for WDM study with semi-rigid capillary

Capacitance	Charge Voltage	Capillary ID	Capillary Length
3.2μF	8-10kV	0.8mm	20mm

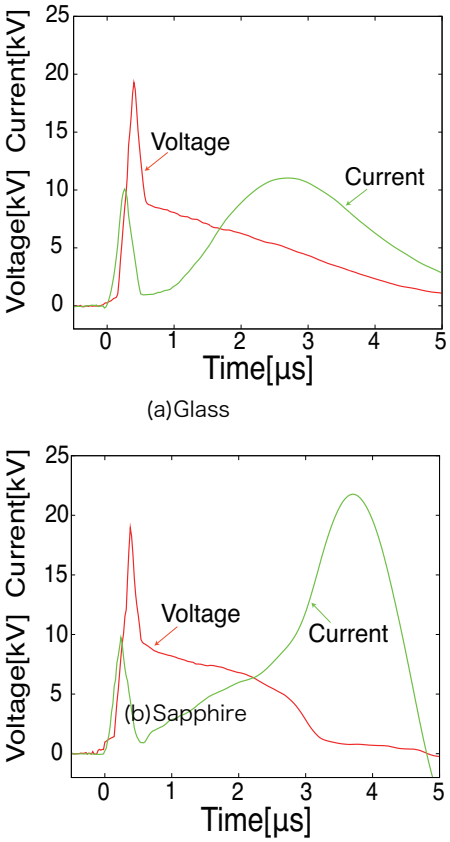

FIG. 4: Typical waveforms of voltage and current for Al wire in Pyrex Glass (a) and Sapphire (b) capillary

the state of material go through a warm dense matter region. We can estimate evolutions of the input energy and conductivity from the voltage-current waveforms.

Figure 4 shows typical waveforms of the voltage and current for Al wire explosion in Glass (a) and Sapphire (b) capillary. As shown, behaviors of the voltage and the current were very similar. The abrupt fall of the voltage signal corresponds to the vaporization of the wire. Reproducibility of the discharge process was very good and we could estimate the conductivity and the input energy for various wire materials.

III. EXPERIMENTAL RESULTS; CONDUCTIVITY OF WIRE PLASMA

We experimentally measured evolutions of the conductivity of Al, Cu, Ag, Au, W, and Mo wires as a function of input electric energy. The pulse power device drove a pulse current through the wire/plasma in the capillary with 10kA peak and a few second period.

Figure 5 shows fast frame-photo images of the capillary plasma. In the gure, T means time from start of the discharge. We can see that, at T=500nsec, the wire-exploded and the wire/plasma lled the capillary volume.

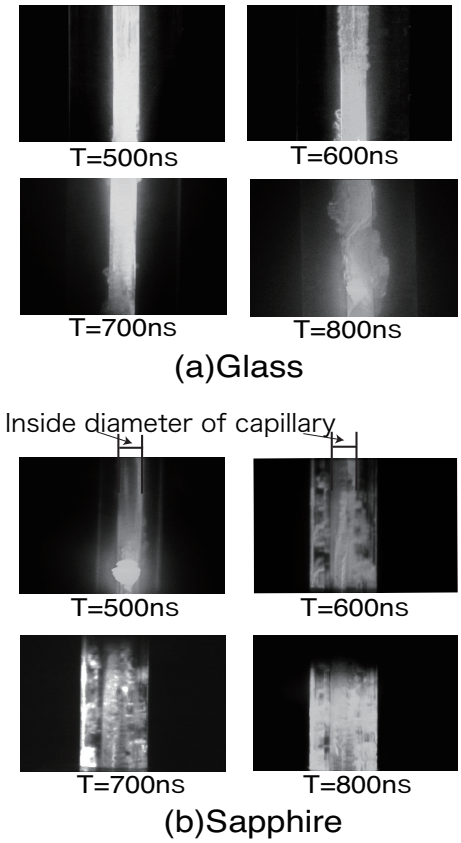

FIG. 5: Fast frame images of plasma evolutions in Pyrex Glass (a) and Sapphire (b) capillary

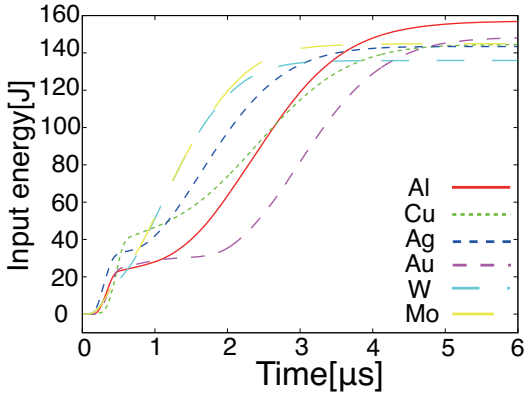

FIG. 6: History of input energy for Al, Cu, Ag, Au, W, and Mo wires

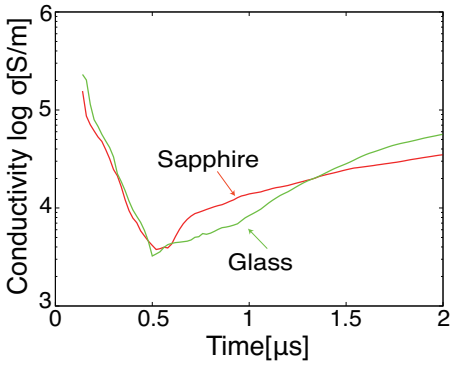

FIG. 7: Evolution of conductivity for Al-wire in Pyrex and Sapphire capillary

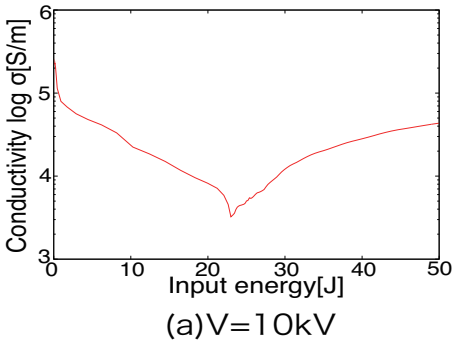

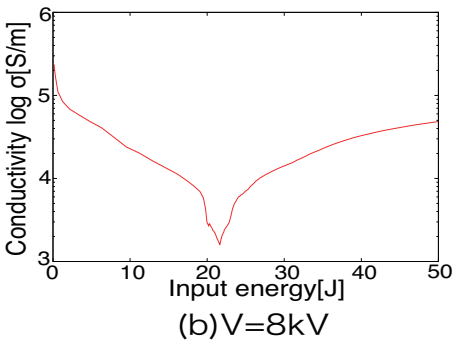

FIG. 8: Conductivity of Al versus input energy for charging voltage of 10kV (a) and 8kV (b)

The boundary between the plasma and capillary wall becomes unclear just after the plasma ll. As indicated by the photo images, a lot of micro-cracks should be induced in the inner side wall of capillary in early phase of the discharge process.

However, in spite of the irregular plasma image, reproducibility of the voltage-current waveforms were very good at least up-to a few sec from the current rise. This result seems to mean the apparent irregularity of the image does not a ect the conductivity of bulk plasma.

By integrating the voltage and current waveforms, we can estimate the history of input electric power to the wire/plasma. Figure 6 shows the input energy to the wires. The result shows the evolution of input energy depended on the material. As has been discussed, the re ection of the curves around T=500nsec corresponds to the vaporization of wire.

Figure 7 shows time evolutions of conductivity of Al in Pyrex Glass and Sapphire capillary. As can be seen,

the traces are very similar. A slight di erence between the traces after T=500nsec is considered to be due to deformation of the capillary diameter. Namely, as the rigidness of Sapphire is much larger than that of pyrex glass, the e ect of deformation should be less than that of Pyrex glass.

Figure 8 shows the evolution of conductivity of Al-wire explosion versus the input electric energy to the wire plasma for charging voltages of V=10kV (a) and V=8kV. As has been expected, the values of input energy corresponding to the minimum conductivity are almost the same, in spite of the di erent charge voltage. Also we can see that the conductivities have minimum value of less than $10^4 S/m$ just after the evaporation, and these are consistent with our previous results. The behavior was a little bit di erent in the case of W and Mo wire experiments. This maybe comes from a multi-phase state, i.e., inhomogeneous liquid-gas state, at the minimum conductivity region [6].

IV. CONCLUDING REMARKS

We measured evolutions of electrical conductivity of Al, Cu, Ag, Au, W, and Mo using fast pulse discharges in semi-rigid vessels; Pyrex glass and Sapphire capillary. Reproducibility of the discharge voltage and current was very good until the capillary was completely broken. This means the exploding plasma can be con ned in the capillary for more than sec. That enables us to estimate the evolution of electrical conductivity of them around WDM regime together with the e ect of rigidness of capillary on the conductivity data. Although the behavior of wire explosion in Pyrex glass was a little bit di erent form that in Sapphire capillary, the data was considered to be su cient to make the scaling of conductivity of WDM.

Experimental results showed that, regardless of materials, the minimum conductivity was less than $10^4 S/m$. This value is consistent with theoretical estimations [7] [8] and also supports our previous result obtained by wire explosion in water [3], i.e., the conductivity has a minimum less than $10^4 S/m$ around $\log(\rho/\rho_s)$=-1.5 at 5000K.

V. ACKNOWLEDGMENT

We appreciate Dr.Toru Sasaki, Nagaoka University of Technology, for his helpful comments on the experimental device. This work is partly supported by the Grant-in-Aid for Scienti c Research (A) from the Japan Society for the Promotion of Science (JSPS).

[1] K.Horioka, T.Kawamura, M.Nakajima, et.al., Nucl. Instrum. Mthods, A 606, 1 (2009)
[2] T.Sasaki, Y.Yano, M.Nakajima, T.Kawamura, K.Horioka, Laser and Particle Beams, 24, 371 (2006)
[3] T.Sasaki, M.Nakajima, T.Kawamura, K.Horioka, Phys. Plasmas, Vol.17, 084501 (2010)
[4] A.W.Desilbva, and H-J.Kunze, Phys. Rev. E 49, 4448 (1994)
[5] A.W.Desilva, and J.D.Kasouros, Phys. Rev. E57, 5945 (1998)
[6] I.V.Lomonosov, Laser Particle Beams, 25, 567 (2007)
[7] M.P.Desjarlais, Contrib. Plasma Phys., Vol41, 267 (2001)
[8] S.Kuhlbrodt and R.Redmer, Phys. Rev, E62, 7191 (2000)

PRODUCTION OF THE ACCELERATED IONS UP TO MeV -ORDER IN THE DIVERGENT Z-PINCH PLASMA

M. Nishio K. Takasugi * and H. Sakuma
College of Science and Technology, Nihon University, Tokyo 101-8308, Japan
** Institute of Quantum Science, Nihon University, Tokyo 101-8308, Japan*

Abstract

The measurements of velocities and energies of the accelerated ions in the divergent gas-puff z pinch were carried out by using the Thomson Parabola Ion analyzer in order to reveal indirectly the electron acceleration causing 250-keV hard x-ray. Energies of accelerated ions (Ar or C) were measured to be the MeV-order. Because two types of parabola curves on the line of constant velocity and on the line of constant energy per charge exist, two acceleration mechanisms may be required.

1 . Introduction

Plasma Focus (PF) is a kind of plasma formation technique by using the pulsed power. Some papers reported the axial acceleration of particles(ions[1−7], electrons[8−10] and neutrons[11,12]) in the PF experiments. Although the z pinch plasma is produced by the similar technique with plasma focus, the high energy particle acceleration in the z pinch may not occurred due to the good axial symmetry (Fig. 1a). It is considered that the divergent con guration of imploding plasmas could have an important role for the high energy particle acceleration. While the many theoretical models[13−19] were discussed, the experimental data for the determination of the acceleration mechanism is not enough.

The study that the focused plasma con guration is achieved by using pu ed gas was reported[20] (Fig. 1b). They indicated the possibility of the axial acceleration of electrons up to 250 keV in the divergent gas-pu z-pinch (DZP) experiments. The mechanism of generation of those high energy particles may be similar to the that in the PF experiments. Because the shapes of the initial media of DZP experiments were untipped circular cone by spreading the gas nozzle angle, the divergently imploding current sheets like the PF may have been produced in DZP experiments, despite the di erent initial media (ionized pu ed gas or the insulator materials). In order to discuss the acceleration mechanism of axial high energy particles produced in the divergent imploding plasmas, we measured the energies of the accelerated ions in the DZP experiments by using Thomson Parabola (TP) analyzer. Although the measurements of the energy-density plot (energy spectrum) are required for the acceleration mechanism (eq. cosmic-rays acceleration in the astrophysics), it was not carried out in this study. Some acceleration processes were analogized from obtained parabola tracks in this study.

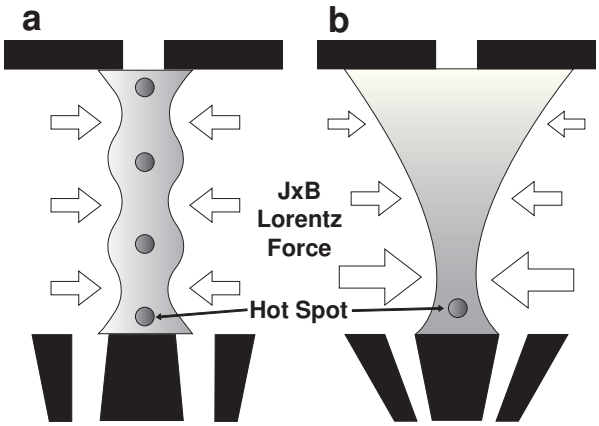

Figure 1: (a) Conventional gas-puff z pinch configuration. Neutral gas is injected between anode and cathode with 0-degree nozzle angle. Axially-uniform gas distribution is required for scattered hotspots on the electrode axis. (b) Divergent gas-puff z pinch configuration. Localization of hotspots is achieved by the dissymmetry of the puffed gas.

2 . Experiments

The SHOTGUN-I z-pinch device at Nihon University was used as the high-voltage pulse-power supply. The energy storage section of the device consists of 30 kV 24 μ F capacitor bank, and the maximum discharge current is 300 kA. The charged voltage of the bank was 25 kV (7.5 kJ) in this experiment. Details of experimental setups are similar to that of the previous work [20]. The isolated gas distribution can be formed between the electrodes with a high-speed gas valve and an annular Laval nozzle mounted on the anode. Figure 1a shows the arrangements of electrodes in the usual z-pinch and the divergent gas-pu experiment. In

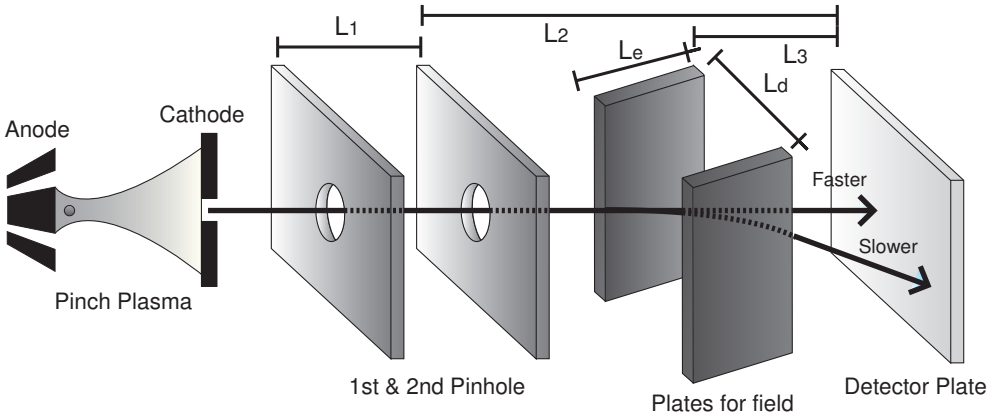

Figure 2: Resulting injected ions through the two pinholes and are deflected by the applied electric and magnetic fields. Accelerated particles hit to the detector surface on the analyzer axis corresponding to the magnitude of energy. After the experiments, the plates are etched by NaOH during a proper interval for a visualization of particle tracks.

the divergent gas-pu experiment (Fig. 1b), the hollow conical gas distribution was achieved by the divergent shaped Laval nozzle (ejection angle of 30-degree outward). The distance between the electrodes was 3 cm. Ar gas was used in this experiment, and the plenum pressure of the gas valve was 5 atm. Total discharge current was measured by the Rogowski coil located outside the chamber. Soft x-ray intensity was detected by x-ray diodes (XRDs) with Ni and Al photocathodes. The XRDs are more sensitive to high energy photons in this order. X-ray signal was detected by a scintillation probe (SCI) with a 10 m Be lter. In order to measure high energy x-ray distribution around the device, an x-ray lm cassette was prepared.

Accelerated ions generated by pinch escapes from inter-electrodes into outside of cathode. The energy of ions trapped with the detector is measured by using Thomson Parabola (TP) analyzer [21−24]. The TP analyzer was used for the axially accelerated ions in the many PF experiments, and they reported that the maximum kinetic energy was a few MeV order at highest. The parabola spatial distribution of the DZP experiments may be close to the one of the PF experiments. Although the initial object of this measurement was the accelerated electron, it is di cult for our experimental system to detect the electron directly because of the electrodes design. That is why we measured the ions that may be accelerated opposite to the electron using by TP analyzer.

When the ion species are determined, the velocity, the momentum and the kinetic energy of the ion were obtained by measuring the distance from origin point to the tracked point along the eld axis in each parabola. The detector without electrical system can reduce noises and eliminate the secondary-electron signal induced by electromagnet wave. TP analyzer was set up at the outer end on the discharge axis. Schematic arrangement of the analyzer is shown in Fig. 2. Resulting injected ions through the two pinholes, and hit to the detector surface after the de ection by the electric and magnetic elds. Applied intensity of static electirc and pulsed magnetic ux density are 8 kV /8 mm and 0.45 T, respectively. When the high energy ions impact the plastic plate "Baryotrak-P" (Nagase-Landauer Co., Ltd.), small invisible tracks would be generated on the surface. Those tracks become observable after etching with NaOH water solution. In order to estimate the ion energies, the de ection distances of ion tracks from the origin in the elds and were measured. Analyzer parameter is shown as follows: plate size; 30 30 [mm], distance between cathode and the plate; 800 [mm], rst pinhole diameter D_1; 1.0 [mm], second pinhole diameter D_2; 0.4 [mm], distance between pinholes L_1; 170 [mm], distance between second pinhole and plate L_2; 380 [mm], distance between the eld and plate L_3; 355 [mm], distance between electrodes L_d; 8 [mm], electrode width along the axis for both electric and magnetic elds L_e; 25 [mm].

De ected distance by electric eld; y and one by magnetic eld; z has related to be

$$y = \frac{E_l m_p}{{B_l}^2 eL} \left(\frac{Z}{A}\right)^2 \quad (1)$$

The parameters are shown as follows: E_l; the product of electric eld strength and operating distance, B_l; the product of magnetic ux density and operating distance, m_p; unit mass of nucleon, e; elementary charge, L; distance between the eld and

plate, Z; electrical charge, A: atomic mass number. Eq. 1 shows that y is the quadratic function of z. As higher energy particles remain una ected by the elds, the tracked points get close to the origin of the detecting plate. The velocity of particles is shown as follows.

$$v = \frac{yE_l}{zB_l} \tag{2}$$

As shown in eq. 2, velocity v is represented by the slope of line in the y-z coordinates because of the constant E_l and B_l. Track points on a slope of line from the origin point have same velocity.

The energy per unit mass of particles is shown as follows.

$$\frac{1}{2}Am_p v^2 \frac{1}{Z} = \frac{1}{2}E_l^2 e \frac{1}{z} \tag{3}$$

As shown in eq. 3, the kinetic energy per unit mass is the function of only z coordinates. Tracked points on a line parallel to the y axis have same energy per unit mass. The determination of ion species need the the ratio of charge/mass. Because the charge Z and atomic mass number A are not obtained from above theoretical analogy, the experimental selection of the species candidates are required. The ratio of charge/mass is shown as follows.

$$\frac{Z}{A} = \frac{E_l m_p y^2}{B_l^2 eLz} \tag{4}$$

In this study, ions possible to appear on the parabola tracks could be Ar as discharge gas and C as anode materials.

3 . Results

Hard x-ray radiation was observed in the DZP experiments with 30-degree gas nozzle in this study as in 10-degree gas nozzle experiment of the previous work. It was con rmed that the similar acceleration phenomena experiments could have occurred in the 30 degree nozzle as well as 10 degree one. Because x-ray adsorption measurements were not carried out in this study, the energy of the hard x-ray radiation was not apparent. According to the previous results, the energy was calculated to be almost ten times higher than the charged voltage of capacitor bank. Fig.3 shows the typical waveform of discharge current. Abrupt decrement of current from sinusoidal change indicates the restriction of the current due to the increment of the plasma impedance by the pinch phenomena. At same timing with the pinch, the x-ray signals of scintillation probe were detected.

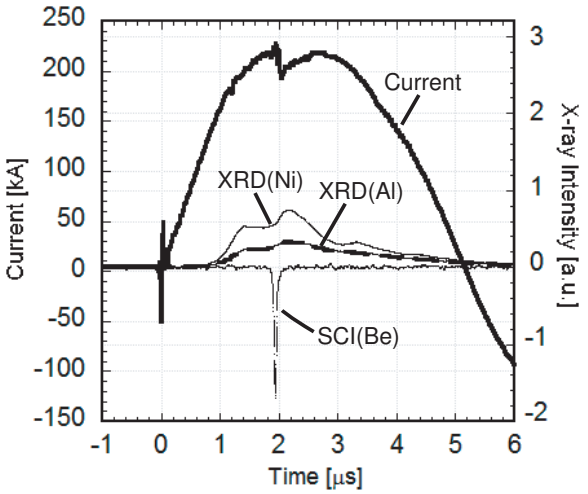

Figure 3: Typical current waveform and x-ray signals.

Obtained typical distribution from TP analyzer shows roughly three parabola curves. Because the optimization of spot size of each parabola was not enough to determine the ion species, the parameter for each parabola was calculated for both cases of Ar ions (discharge gas) and C ions (anode materials). Table 1 shows the maximum velocity of particles in each parabola. Maximum velocity of parabola 1 is close to parabola 2, and parabola 3 is higher than parabolas 1 and 2. Table 2 shows the maximum kinetic energy of particles in each parabola. Similarly, Table 3 shows the maximum kinetic energy per mass unit of particles in each parabola. Accelerated ions have the maximum energies up to 4.65 MeV in case of Ar and up to 1.40 MeV in case of C in the divergent gas-pu z pinch. In table 3, maximum energies per charge of parabolas 2 is close to that of parabola 3.

Ion	Parabola 1	Parabola 2	Parabola 3
Ar	3470 km/s	3680 km/s	4720 km/s
C	3470 km/s	3680 km/s	4720 km/s

Table 1: Calculation of the maximum velocity in the each parabola.

Ion	Parabola 1	Parabola 2	Parabola 3
Ar	2.50 MeV	2.83 MeV	4.65 MeV
C	0.75 MeV	0.83 MeV	1.40 MeV

Table 2: Calculation of the maximum energy in the each parabola.

Ion	Parabola 1	Parabola 2	Parabola 3
Ar	0.78 MeV	0.43 MeV	0.44 MeV
C	0.78 MeV	0.43 MeV	0.44 MeV

Table 3: Calculation of the maximum energy per charge in the each parabola.

4 . Discussions

Two types of parabola curves on the line of constant velocity line and on the line of constant energy per charge exist. The fact may shows another acceleration mechanism exists. However, the determination of ion species were not carried out in this study because of the incomplete of the optimization of the parabola spot size. The constant-velocity acceleration may be re ected to the existence of the transient phenomena with certain velocity. The constant-energy acceleration may be re ected to the existence of the transient phenomena with certain potential.

The range of the energy is likely to be similar to that of the plasma focus experiments. From this result, the divergent con guration of imploding plasmas like plasma focus experiments could have an important role for the high energy particle acceleration.

For the detailed discussion of the acceleration mechanism in the divergent z pinch experiments, the energy spectrum measurements are needed. For the determination of ion species, the optimization of the parabola spot size is required.

5 . Conclusion

Energies of accelerated ions (Ar or C) in the divergent gas pu z pinch were measured to be the MeV-order. Because two types of parabola curves on the line of constant velocity line and on the line of constant energy per charge exist, two acceleration mechanisms may be required.

References

[1] M. J. Rhee and R. F. Schneider,"Compact pulsed accelerator", IEEE Trans. Nucl. Sci., NS-30, 3192-3194. (1983).

[2] M. Sadowski, J. Zebrowski, E. Rydycier and J. Kucinski, "Ion emission from plasma focus facilities", Plasma Phys. Contol. Fusion, Vol. 30, No. 6, 763-769, (1988).

[3] H. Kelly and A. Marquez, "Ion-beam and neutron production in a low-energy plasma focus", Plasma Phys. Contol. Fusion, Vol. 38, 1931-1942. (1996).

[4] T. Yamamoto, K. Shimoda, K. Kobayashi and K. Hirano,. "Correlation between Plasma Dynamics and Emission of Deuteron Beam, X-rays and Neutrons in a Plasma Focus Discharge", Jpn. J. Appl. Phys., Vol. 23, No. 2, 242-246. (1984)

[5] X. M. Guo. and C. M. Luo, "Experimental study of Energy Spectrum of ion beams from gas-puff z-pinch plasma", J. Phys. D Appl. Phys., Vol. 29 388-391.(1996)

[6] H. Neo and D. K. Park "Measurement of Argon Ion Beam and X-ray Energies in a Plasma Discharge." Physica Scripta, Vol. 65, 350-355. (2002)

[7] G. Gerdin, W. Styger and F. Venneri, "Faraday Cup Analysis of Ion Beams Produced by a Dense Plasma Focus." J. Appl. Phys., Vol. 52 No. 5. 3269-3275. (1980)

[8] J. Pouzo, H. Acuna, M. Milanese and R. Moroso, "Relativistic electron beams detection in a dense plasma focus", Eur. Phys. J. D., Vol. 21, 97-100. (2002).

[9] D. R. Kania and L.A. Jones, "Observation of an Electron Beam in an Annular Gas-Puff Z-Pinch Plasma Device", Phys. Rev. Lett., Vol. 53 No. 2. 166-169. (1984)

[10] A. Patran, L. C. Tan, D. Stoenescu, M. S. Rafique, R. S. Rawat, S. V. Springham, T. L. Tan, P. Lee, M. Zakaullah and S. Lee, "Spectral study of the electron beam emitted from 3 kJ plasma focus", Plasma Sources Sci. Technol., Vol. 14, 549-560. (2005).

[11] O. A. Anderson, W. R. Bakers, S. A. Colgate, J. Ise Jr., and V. Pyle, "Neutron Production in Linear Deuterium Pinches", Phys. Rev., Vol. 110, No. 6, 1375-1387. (1958)

[12] M. Milanese, R. Moroso and J. Pouzo, "A study of the production of neutrons in a dense plasma focus source operated with a non-uniform density of deuterium neutral gas", J. Phys. D: Appl. Phys., Vol. 31, 85-92. (1998).

[13] Y. Kondo, "A Model of Charged Particle Accelerations in the Plasma Focus", J. Phys. Soc. Jpn., Vol. 53. No. 12. 4200-4209. (1984)

[14] B. A. Trubnikov and S. K. Zhadanov, "Particle acceleration by Breaking of the constrictions of a z-pinch and a plasma focus", Sov. J. Phys., Vol. 43, No. 1, 48-54. (1976)

[15] R. Deutsch. and W. Kies, "Ion Acceleration and Runaway in Dynamical Pinches", Plasma Phys. Control. Fusion, Vol.30 No.3 263-276. (1988)

[16] P. F. Browne, "Acceleration in the plasma focus and in astrophysics", Laser and Particle beams, Vol. 6, Part 3, 409-420. (1988).

[17] B. A. Trubnikov, "Particle acceleration and neutron production at the neck of plasma pinches", Sov. J. Plasma Phys., Vol. 12, No. 4, 271-283. (1986).

[18] J. Fukai and E. J. Clothiaux, "Mechanism for the Hard x-ray Emission in Vacuum Spark Discharges", Phys. Rev.Lett., Vol. 13, No. 14, 863-866. (1975)

[19] K. Hasegawa, H. Akiyama, S. Katsuki, S. Maeda, F. Kinoshita and H. Kuribayashi, "Development of Inductive Energy Strotage Pulsed Power Genrator with Output of MV class", NIFS-PROC-23, 101-107. (1905)

[20] K. Takasugi and E. Kiuchi, "Hard X-Ray Radiation from a Z-Pinch with a Divergent Gas-Puff", Plasma Fusion Res. Rapid Commun., Vol. 2, 036. (2007)

[21] J. J. Thomson, "The Corpuscular Theory of Matter", Archibald Constable Co., Ltd., London, (1907)

[22] M. J. Rhee, "Compact Thomson Spectrometer." Rev. Sci. Instru., Vol. 55. No. 8. 1229-1234. (1986)

[23] H. Herold, A. Moser, M. Sadowski and H. Schmidt, "Design and calibration of a Thomson ion analyzer for plasma focus studies", Rev. Sci. Instrum., Vol. 52, No. 1, 24-26. (1981).

[24] K. Hirano, I. Kaneko and K. Shimoda, "A method for measuring electron energy distribution in a plasma focus", J. J. Appl. Phys., Vol. 29, No. 6, 1182-1188. (1990).

TREATMENT OF SHIPS' BALLAST WATER BY IRRADIATION OF PULSED, INTENSE RELATIVISTIC ELECTRON BEAM

Hironobu Kondo[1], Hiroki Takehara[2], Takashi Kikuchi[2], Toru Sasaki[2], and Go Imada[1,3,*]

[1]*Department of Information and Electronics Engineering, Niigata Institute of Technology, 1719 Fujihashi, Kashiwazaki, Niigata 945-1195, Japan*

[2] *Department of Electrical Engineering, Nagaoka University of Technology, 1603-1 Kamitomioka, Nagaoka, Niigata 940-2188, Japan*

[3]*Extreme Energy-Density Research Institute, Nagaoka University of Technology, 1603-1 Kamitomioka, Nagaoka, Niigata 940-2188, Japan*

ABSTRACT

Zooplankton contained in ships' ballast water has been successfully treated by irradiation of pulsed, intense relativistic electron beam (PIREB). A treatment chamber is filled up with solution of 3-wt% salt in water containing a larva of artemia as the zooplankton, and is irradiated by the PIREB (2 MeV, 0.4 kA, 140 ns). We have found that electric conductivity and pH of the salt solution does not change significantly within 10 shots of the PIREB irradiation. We have obtained that the artemia of 24 % is inactivated by firing 10 shots of the PIREB irradiation.

1. Introduction

A ship, such as oil tanker and cargo ship, is navigated with ballast water to stabilize own hull. The ballast water is carried around the world and dumped at a port of call, and then an undesirable propagation of microbe, bacillus, egg and larva of marine organism, and marine plankton occur within ecosystem in the sea. To conserve environments of sea, therefore, International Convention for the Control and Management of Ships' Ballast Water and Sediments is adopted at International Maritime Organization in 2004.[1)] The ships must conduct the ballast water management including the ballast-water treatment device not later than 2016.[1)] Many treatment methods of the ballast water, such as chemical, heating, electric discharge, magnetic, and radioactive treatments, have been studied. At present, however, each and every method has technical, costly, and environmental problems.

In the present study, we propose a new treatment method of the ships' ballast water using an irradiation of pulsed, intense relativistic electron beam (PIREB). In this method, chemicals and/or additives are basically unnecessary for the treatment. The purpose of this paper is to investigate the properties of PIREB injection into the ballast water and the treatment characteristics on zooplankton by irradiation of the PIREB.

*E-mail: imada@iee.niit.ac.jp
Phone: +81-257-22-8142

2. Principle on Treatment of Zooplankton by Irradiation of PIREB in Ballast Water[2)]

Water molecule (H_2O) in the ballast water is ionized by collision with fast electron (e_{fast}) in the PIREB.

$$H_2O + e_{fast} \rightarrow H_2O^+ + e_{aq} + e_{slow}. \quad (1)$$

Here, H_2O^+ is the water ion, e_{aq} is the hydrated electron, and e_{slow} is the slow electron. In the above reaction, e_{fast} changes to e_{slow} with losing the kinetic energy. After that, H_2O^+ resolves into hydrogen ion (H^+) and OH radical.

$$H_2O^+ \rightarrow H^+ + OH. \quad (2)$$

Furthermore, OH ion and H radical are generated with reaction between e_{aq} and H_2O.

$$H_2O + e_{aq} \rightarrow OH^- + H. \quad (3)$$

In addition to the above mentioned processes, H and OH radicals are also generated by dissociation of excited water molecule (H_2O^*) generated by collision with e_{fast}.

$$H_2O + e_{fast} \rightarrow H_2O^*. \quad (4)$$

$$H_2O^* \rightarrow H + OH. \quad (5)$$

Since a cell membrane of the zooplankton is broken with reaction between the H radical and oxygen in the cell, the zooplankton will be inactivated and is killed as a result of that wound. Moreover, the OH radical also reacts with hydrogen in the cell. After the serial processes, the H and OH radicals may revert to H_2O.

A deoxyribonucleic acid (DNA) of the zooplankton is directly damaged by irradiation of the PIREB. It induces the inactivation and death of zooplankton. A bremsstrahlung generated with the interaction between the PIREB and a matter also damages the DNA.

3. Experimental Apparatus

A. PIREB Generator

Figure 1 shows the schematic diagram of PIREB generator, "ETIGO-III" installed in Extreme Energy-Density Research Institute, Nagaoka University of Technology.[3)] It consists of a Marx generator, a pulse forming line, transmission lines, and induction acceleration cells of four stages. The Marx generator generates the output voltage of 670 kV. The pulse forming line converts the stored energy of the Marx generator to an output pulse having the voltage of 670 kV, current of 60 kA, and pulse duration of 150 ns. Since the output pulse of the pulse forming line is fed to the four acceleration cells through the oil-insulated coaxial transmission lines in parallel, the feed current to each cell becomes 15 kA. In each cell, three amorphous-metallic magnetic cores are installed as a 1:1 one-turn transformer producing approximately 2 MV (670 kV × 3) and 5 kA (15 kA/3) per cell. The PIREB with the kinetic energy up to 2 MeV is generated with a field-emission foilless electron-beam diode where a hollow cathode and a ring anode set at the first acceleration cell. An axial magnetic field of 0.23 T is applied in the anode-cathode gap having the gap distance of 73 mm. The inner and outer diameters of the hollow cathode are 59.5 mm and 60 mm, respectively. The inner diameter of the anode ring is 160 mm. Here, the diode gap is vacuumed to 0.02 Pa (1.5×10^{-4} torr) with an oil-diffusion pump and an oil-rotary pump. The PIREB is guided by an external magnetic field of 0.5 T through the other acceleration cells, so that it is inductively postaccelerated with the three accelerating gaps giving the final kinetic energy up to 8 MeV. The minimum time interval of the PIREB generation is estimated to be 5 minutes that depends on a charging period of capacitor bank for the axial magnetic field.

B. Treatment Chamber

Figure 2 shows the cross-sectional view of treatment chamber by the irradiation of PIREB. It consists of the electron-beam diode, air bulkhead, treatment vessel, and Rogowski coils. The treatment vessel is made of a polypropylene cylinder with the inner diameter of 80 mm, the length of 86 mm, and the capacity of 0.8 L, where an end flange of the vessel is floated from a ground. The treatment vessel is separated from a vacuum part of the electron-beam diode by the air bulkhead, and is filled with a 3-wt% salt solution as ballast water. The salt solution is made from distilled water and common salt. A larva

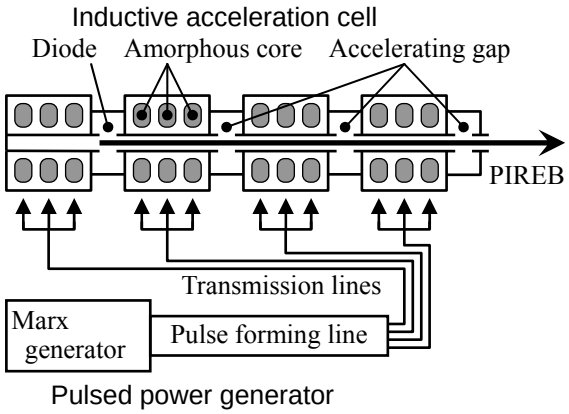

Fig. 1. Schematic diagram of pulsed, intense relativistic electron beam (PIREB) generator, "ETIGO-Ⅲ".

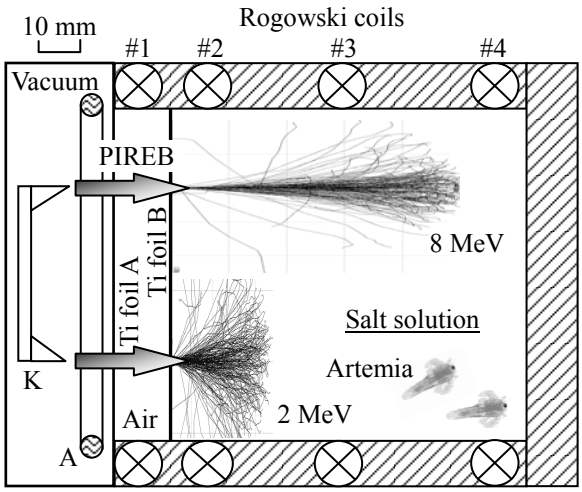

Fig. 2. Cross-sectional view of treatment chamber. Simulated trajectories of electron are also indicated.

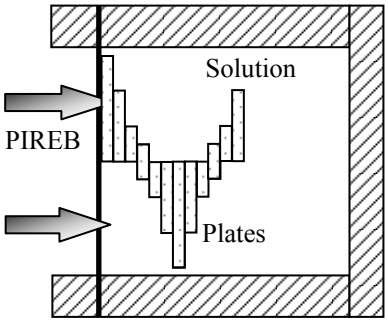

(a) Cross-sectional view

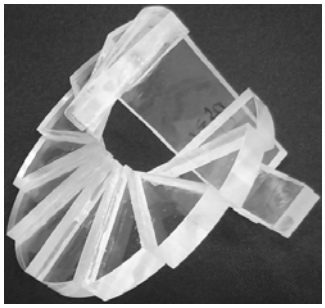

(b) Acrylic-resin plates

Fig. 3. Measurement setup for PIREB penetration.

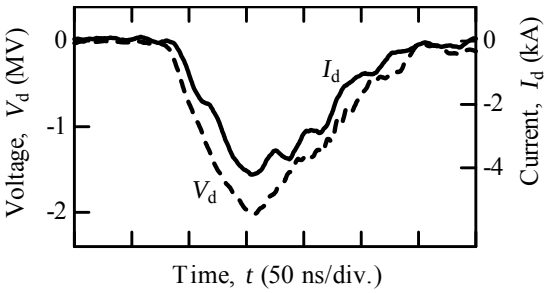

Fig. 4. Time evolution of voltage (V_d) and current (I_d) of electron-beam diode.

Fig. 5. Electron damage recorded on acrylic-resin plates.

of artemia is contained in the salt solution as a zooplankton. The air bulkhead consists of a couple of titanium foil at the thickness of 40 μm with a stainless-steel punching plate at the optical transparency of 55 %. The air-gap distance between the titanium foils is 10 mm. Since the pulse duration of the PIREB used in this study is observed to be of the order of 100 ns, the titanium foil and punching plate are not cooled with water or coolant. In this study, a pulsed voltage of –2 MV produced with ETIGO-III is applied to the cathode-anode gap. At the PIREB energy of 2 MeV, the minimum kinetic-energy loss of the electron through the titanium foil is calculated to be 26 keV,[4] which is negligible in comparison with the PIREB kinetic energy of 2 MeV. No axial magnetic field is applied to the chamber.

C. Measurement of PIREB and Observation of Zooplankton

Figure 2 also shows the measurement setup for the PIREB. The electron-beam diode voltage and current are measured with a copper-sulfate-solution voltage divider and an external-time-integration Rogowski coil, respectively. The irradiated and the injected PIREB current for the salt solution are measured with the Rogowski coils placed at the inlet (#1), front (#2), middle (#3), and end (#4) of the treatment chamber, respectively. The exact positions of Rogowski coils #1, #2, #3, and #4 are the front of, 5 mm, 35 mm, and 77 mm behind the titanium foil B, respectively. The signals from the voltage divider and the Rogowski coils are simultaneously recorded on a multi-channel digital storage scope.

Figure 3 shows the measurement setup for the PIREB penetration into the salt solution. The electron damage is recorded on acrylic-resin plates assembled as spiral stairs. In this setup, the PIREB penetration can be measured with 4-mm resolution.

The zooplankton, larva of artemia, is observed by using a stereoscopic microscope. We consider that the artemia which stops his motion in a minute is inactive.

4. Results and Discussion

A. PIREB Penetration into Solution

Figure 4 shows the typical time evolution of the electron-beam diode voltage (V_d) and current (I_d). It is found that V_d which corresponds to acceleration voltage of the PIREB reaches −2 MV within 70 ns after rising in the voltage, and the pulse width of V_d is estimated to be 150 ns (FWHM). We also found that the peak current of I_d is estimated to be −4 kA. It is well known that conversion efficiency from electron-beam diode current to the PIREB current is

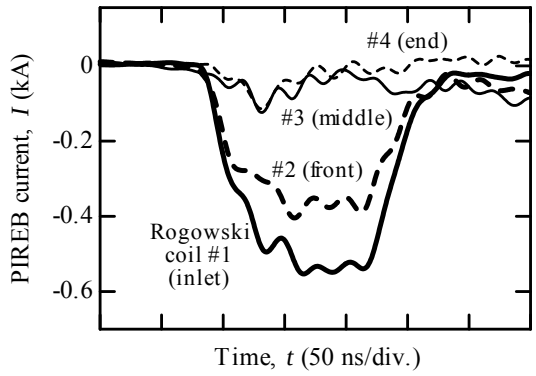

Fig. 6. Time evolution of PIREB current in treatment chamber.

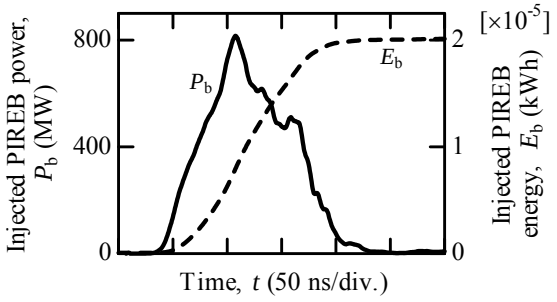

Fig. 7. Time evolution of PIREB power and energy injected into solution.

reasonable high, for example, it reaches above 90 % in ETIGO-III.[3)]

Simulated trajectories of electron into the salt solution are shown in Fig. 2. The trajectories are calculated with CASINO program.[5,6)] It is found that the maximum penetration depth d_p of 8-MeV electron reaches 70 mm. Although d_p is reduced to be 17 mm in 2-MeV electron, the electron spreads over 30 mm. It suggests that the 2-MeV PIREB is suitable for the treatment in large volume.

Figure 5 shows the electron damage on the acrylic-resin plates. It is found that the tree-like damage is recorded on the tail end of the first plate. Since the injection pore of the electron is confirmed at the side of the first plate close to the surface of second one, the PIREB penetrates the salt solution more than enough 4 mm.

Figure 6 shows the typical time evolution of the PIREB currents in the treatment chamber. It is found that the PIREB with the current of I = −550 A is irradiated onto the chamber. The loss of current between I_d and I occurs at the air bulkhead. We also found that the injected current of PIREB into the solution is estimated to be above −400 A. The pulse width of injected current is estimated to be 140 ns (FWHM). Since the PIREB is quenched within the solution, the current decreases dramatically at the middle and end of the chamber. We have confirmed that the reproducibility of the PIREB current is good within each and every shot.

Figure 7 shows the typical time evolution of the PIREB power (P_b) and the energy (E_b) injected into the salt solution. Here, the P_b is calculated as the product of V_d and I at the front of chamber, and the E_b is estimated from the time integral of P_b, where the P_b and the E_b are somewhat overestimated because we neglect the kinetic-energy loss of the PIREB within the air bulkhead. Although the peak power of P_b reaches 800 MW, E_b is estimated to be 2×10^{-5} kWh which is represented as only 72 J because the pulse width of PIREB is short.

TABLE I
Inactivation rate of larva of artemia as a function of time without PIREB irradiation.

Time, T (min)	Inactivation rate, η (%)
10	0 ~ 2
65	0 ~ 4

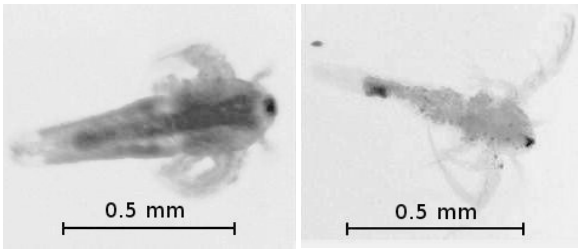

(a) Before irradiation (b) After irradiation

Fig. 8. State of larva of artemia.

B. Inactivation of Zooplankton without PIREB Irradiation

To confirm accurately characteristics of inactivation of the zooplankton in the treatment chamber, the inactivation rate of the larva of artemia (η) is observed without the PIREB irradiation. Here, η is defined as

$$\eta = \frac{n}{n_T}, \tag{6}$$

Here, n is the number of inactivated artemia and n_T is the total number of artemia.

Table I shows the η as a function of time. Here, 50 larvae of artemia are contained in the salt solution, and then left the specific time T. Here, T of 10 and 65 minutes correspond to the necessary and shortest

TABLE II
Inactivation rate of artemia and electrical conductivity and pH of solution at one shot of PIREB irradiation.

Total number of artemia, n_T	Number of inactivated artemia, n	Inactivation rate, η (%)	Conductivity (mS/cm)		pH	
			Before irradiation	After irradiation	Before irradiation	After irradiation
41	1	2	19.5	–	5.4	–
45	1	2	19.5	–	5.8	–
42	2	5	19.4	–	5.8	–
48	2	4	19.4	–	5.6	–
42	1	2	19.3	–	5.7	–

TABLE III
Inactivation rate of artemia and electrical conductivity and pH of solution at 10 shots of PIREB irradiation.

Total number of artemia, n_T	Number of inactivated artemia, n	Inactivation rate, η (%)	Conductivity (mS/cm)		pH	
			Before irradiation	After irradiation	Before irradiation	After irradiation
46	11	24	19.4	19.4	5.6	6.0
44	5	11	19.5	19.3	5.7	6.0
43	6	14	19.1	19.1	5.6	5.8
43	8	19	19.1	19.1	5.6	5.7
40	9	23	19.1	19.1	5.5	5.7

time for the PIREB irradiation of one and ten shots, respectively. It is found that few larvae of artemia are inactivated without the PIREB irradiation. At T = 65 min, η increases slightly.

C. Inactivation of Zooplankton with PIREB Irradiation

Tables II and III show the inactivation rate of the larva of artemia (η) and the electrical conductivity and pH of the salt solution at one and 10 shots of PIREB irradiation, respectively, where the time interval of the PIREB irradiation is around 7 minutes. Although approximately 50 larvae of artemia are contained in the solution before the PIREB irradiation, a few larvae are missing at the observation by microscope. It is found from Table II that there is no advantage in η at the one shot of PIREB irradiation compared to that without the PIREB irradiation at T = 10 min (cf. Table I). In the 10 shots of PIREB irradiation, on the other hand, η increases to 11-24 % (see Table III). We have succeeded in the treatment of zooplankton in the salt solution by irradiating the PIREB. It seems that the PIREB irradiation, including the bremsstrahlung, is main factor of the inactivation of zooplankton, because the significant change of the electrical conductivity and pH in the salt solution cannot be seen after the irradiation.

Figure 8 shows the state of larva of artemia before and after the PIREB irradiation. The artemia moves his legs actively and swims in the salt solution before the irradiation (see Fig. 8(a)), while the inactivated

artemia is decolorized and stops his motion after the irradiation (see Fig. 8(b)).

5. Conclusion

Conclusions obtained from the studies of the treatment of ships' ballast water by the irradiation of pulsed, intense relativistic electron beam can be summarized as follows.

(1) The PIREB (2 MeV, 0.4 kA, 140 ns) penetrates the 3-wt% salt solution more than enough 4 mm.

(2) The electric conductivity and pH of the 3-wt% salt solution does not change significantly within 10 shots of the PIREB irradiation.

(3) The inactivation rate of the zooplankton, larva of artemia, reaches 24 % at the firing 10 shots of the PIREB irradiation.

The increase in inactivation rate is the subject for a future study.

References

1) IMO: GloBallast Partnerships, http://globallast.imo.org/.
2) Seimei Free-radical Kankyo Kenkyukai ed.: *Mizutokasseisanso*, 35, Ohmsha (2002) [in Japanese].
3) A. Tokuchi, N. Ninomiya, K. Yatsui, G. Imada, Q. Zhu, W. Jiang, and K. Masugata, "Development of High Energy Induction Accelerator, □ETIGO-III□", Proc. 12th Int'l Conf. on High-Power Particle Beams, Haifa, Israel, 175 (1998).
4) ESTAR: Computer program for calculating stopping-power and range tables for electrons (Ver. 1.2), M. Berger, S. Couresy, and A. Zucker, http://phisics.nist.gov/Star (1999).
5) CASINO: Monte Carlo simulation of electron trajectory (Ver. 2.42), D. Drouin, A. Couture, R. Gauvin, P. Hovington, P. Horny, and H. Demers, http://www.gel.usherbrooke.ca/casino/index.html (2002).
6) D. Drouin, A. R. Couture, D. Joly, X. Tastet, V. Aimez, and R. Gauvin: "CASINO V2.42 - A Fast and Easy-to-use Modeling Tool for Scanning Electron Microscopy and Microanalysis Users", Scanning, **29**, 92 (2007).

DEVELOPMENT OF BIPOLAR PULSE ACCELERATOR FOR HIGH-PURITY INTENSE PULSED ION BEAM

H. Ito J. Takabe and K. Masugata

Dep. of Electrical and Electronic Engineering, University of Toyama, 3190 Gofuku, Toyama 930-8555, Japan

Abstract

In order to improve the purity of the intense pulsed ion beam, a new type of a pulsed ion beam accelerator named "bipolar pulse accelerator"has been proposed. A double coaxial type bipolar pulse generator was developed as the power supply of the bipolar pulse accelerator. By applying the bipolar pulse with voltage of about ± 100 kV and pulse duration of about 70 ns to the drift tube of the bipolar pulse accelerator, the ion beam was successfully accelerated from the grounded anode to the drift tube in the 1st gap by the negative pulse of the bipolar pulse and the pulsed ion beam with current density of 40 A/cm^2 and pulse duration of 30 ns was obtained at 50 mm downstream from the anode surface. In addition, part of the ion beam was again accelerated toward the grounded cathode in the 2nd gap by the positive pulse of the bipolar pulse. The pulsed ion beam with the peak ion current density of 2 A/cm^2 and the beam pulse duration of 30 ns was obtained at 25 mm downstream from the cathode surface, which suggests the bipolar pulse acceleration.

1 Introduction

Intense pulsed ion beam (IPIB) technology has been developed primarily for nuclear fusion and high energy density physics research [1,2]. Recently, however, these IPIBs with an ion energy of several 100 keV, a high ion current density of several 100 A/cm^2, and a short pulse duration of < 1 s, has been widely used for materials surface properties modi cation by the methods of ion implantation, ion plasma coatings deposition, and high energy ion beam energetic impact [3-5]. Compared with the traditional ion implantation method, the IPIB irradiation into materials enables the accumulation of energy in very short time into the near surface region while it maintains a low substrate temperature. The annealing by IPIB is expected to be novel annealing techniques for the next generation semiconductor materials such as silicon carbide (SiC). In the case of SiC, a high temperature annealing is normally done by using a traditional thermal method, which requires temperatures as high as 1500-1700 °C to recover the crystal damage and activate the dopants after the implantation. The conventional method at such a high temperature causes several disadvantages such as the redistribution of implanted dopants and increasing of surface roughness. Therefore, IPIB has received extensive attention as a tool for a new ion implantation technology named "pulsed ion beam implantation "to semiconductor materials, since the ion implantation and the annealing can be completed simultaneously.

To meet the requirements of research and industrial application, a number of IPIB sources have been developed so far for di erent applications of IPIBs [6-8]. The producible ion species, however, is limited to the material of electrode (anode), since the anode plasma is produced by a high-voltage ashover and an electron bombardment to the anode surface. In addition, the purity of the IPIB is usually deteriorated by ab-

sorbed matter on the anode surface and residual gas molecules in the diode chamber. Therefore, the conventional pulsed ion diode is not suitable for the application to the ion implantation.

For the application of IPIBs to the semiconductor implantation, it is very important to develop the IPIB technology of generating high-purity ion beams from various species, such as nitrogen, phosphorous, boron and aluminum being useful donor and acceptor in SiC. We have developed a new type of the magnetically insulated ion diode (MID) with an ion source of a gas pu plasma gun and were successful in generating the high-purity pulsed nitrogen ion beam with an ion current density of 54 A/cm^2, a pulse duration of 90 ns and purity of the nitrogen beam of 94 % [9]. In order to improve the purity of the intense pulsed ion beam, we have proposed a new type of pulsed ion beam accelerator named "bipolar pulse accelerator (BPA)"and developed a prototype of the accelerator and a bipolar pulse generator as the power supply of the BPA [10,11]. The bipolar pulse generator consists of a Marx generator and a pulse forming line (PFL) with a rail gap switch on its end. The BPA utilizes a magnetically insulated ion diode with an ion source of a coaxial gas pu plasma gun. In this paper, we present the experimental results of the bipolar pulse generator and preliminary results of the ion beam acceleration by the BPA.

2 Principle of bipolar pulse accelerator

Figure 1 shows the conceptual diagram of the bipolar pulse accelerator. The BPA consists of an ion source, a drift tube and a grounded cathode. As seen in Fig.1, the BPA is an electrostatic two-stage accelerator. In the system, a bipolar pulse of voltage $\pm V_0$, duration τ_p each is applied to the drift tube. At rst the negative voltage pulse of duration τ_p is applied and ions produced in the ion source are accelerated in the 1st gap toward the drift tube. The polarity of the pulse is reversed at $t = t_1$ and the positive voltage pulse of duration τ_p is applied to the drift tube. As a result, the ions are again accelerated in the 2nd gap toward the grounded cathode. The condition for the most e ective acceleration is that the pulse duration τ_p is adjusted to the time of ight delay of the ion to pass through the drift tube, i.e., $\tau_p = L/v_i$, where v_i is the ion velocity in the drift tube and L is the length of the drift tube. This condition can be satis ed by adjusting the parameter of the bipolar pulse and the length of the drift tube. In addition, the merit of the BPA is that the ion source can be installed on the grounded anode, which extremely enhances the accessibility to the anode, while in the conventional PIB diode, the ion source is placed on the anode where the high voltage pulse is applied. This seems to be favorable for an active ion source which is powered by an external power supply.

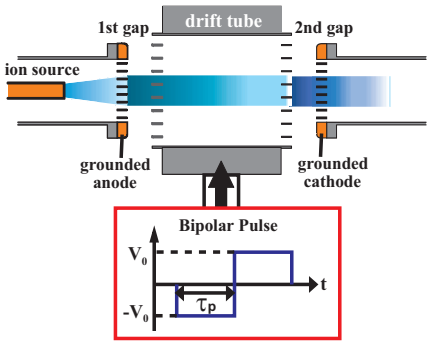

Figure 1 Schematic view of bipolar pulse accelerator.

Figure 2 illustrates the principle of the improvement of the purity of the ion beam. Let us now consider the acceleration of ions in the case that the ion beam produced in the ion source consists of N^+ ion and impurity of H^+ ion. Each ion of N^+ and H^+ is accelerated in the 1st gap toward the drift tube when the negative voltage is applied, where N^+ and H^+ ion beams are schematically described in Fig. 2. As seen in Fig. 2, the length of H^+ beam is much longer than that of N^+ beam due to the di erence of the velocity. We assume that the length of the drift tube is designed to be same as the beam length of N^+ beam with a beam pulse duration τ_p at an acceleration voltage V_0. It is, for example, calculated to be 11.6 cm when $V_0 = 200$ kV and $\tau_p = 70$ ns. On the other hand, the length of H^+ beam at $V_0 = 200$ kV and $\tau_p = 70$ ns is 43.3 cm. When the voltage is reversed and the positive voltage is applied to the

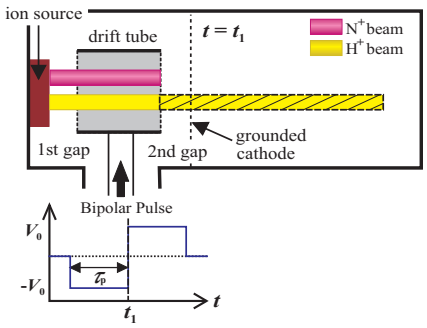

Figure 2 Principle of the improvement of the purity of the ion beam.

drift tube ($t = t_1$), N^+ beam with the length of 11.6 cm in the drift tube is accelerated in the 2nd gap. In contrast, 73 % of the beam is out of the drift tube and decelerated in the 2nd gap by the rst pulse (negative voltage pulse). Hence 73 % of H^+ beam is not accelerated in the 2nd gap by the positive voltage pulse of the bipolar pulse and is removed in the bipolar pulse accelerator. As a result, the purity of the ion beam is improved.

Figure 3 shows in detail the acceleration gap design of the BPA. It is composed of a grounded anode, drift tube and a grounded cathode. In order to produce insulating magnetic elds in both acceleration gaps for suppression of the electron ow, a magnetic eld coil of grating structure is used, which produces a uniform magnetic eld in direction transverse to the acceleration gap.

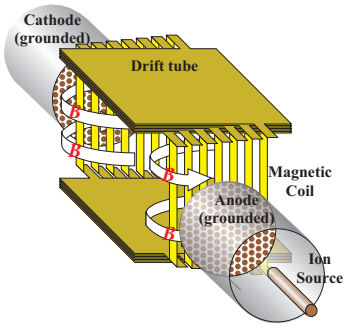

Figure 3 Conceptual drawing of magnetically insulated gap of bipolar pulse accelerator.

3 Experimental Setup

Figure 4 shows the system of the bipolar pulse accelerator. The system consists of a grounded anode, a drift tube, a grounded cathode and a magnetically insulated acceleration gap (MIG). The anode and the cathode are the copper electrodes of diameter 78 mm, thickness 5 mm. The electrodes are uniformly drilled with apertures of diameter 4 mm, giving beam transmission e - ciency of 58 %. The magnetic coil of the MIG is installed on the rectangular drift tube. The uniform magnetic eld with strength of 0.3-0.4 T is produced in the acceleration gap of gap length $d_{\mathrm{A-K}} = 10$ mm by a capacitor bank with capacitance of 500 F and charging voltage of 5 kV. At peak of the magnetic eld, the bipolar pulse voltage supplied from bipolar pulse generator is applied to the drift tube. To obtain higher transmission e ciency of the ion beam, right and left sides of the coil consist of 8 blades each and have a grating structure. Each of the blades (10 mm^W 118 mm^L 1 mm^T) is connected in series and works as an 8-turn coil. Since the drift tube is connected to a high voltage terminal of a bipolar pulse generator, the pulsed current produced by the capacitor bank is applied to the coil through an inductively isolated current feeder (IC). The IC is a helically winded coaxial cable and the outer conductor of the IC is connecting the grounded vacuum chamber and the drift tube with inductance of 12.4 H.

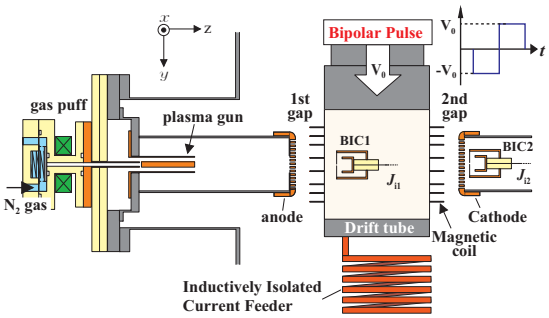

Figure 4 Experimental setup of bipolar pulse accelerator.

A gas pu plasma gun was used as the ion source in order to produce the pulsed ion beam with high purity and is installed inside the anode. It consists of a coaxial plasma gun and a high-speed gas pu valve. The plasma gun has a pair of coaxial electrodes, i.e. an inner electrode of 80 mm length by 6 mm outer diameter and an outer electrode of 18 mm inner diameter. The inner electrode has six gas nozzles of 1 mm diameter. The gas pu valve consists of a nylon vessel,

an aluminum valve and a driver coil. The vessel is pre- lled with N_2 gas up to 2 atm. By applying a pulse current to the driver coil, a pulsed strong magnetic eld is produced and the magnetic pressure pushes the aluminum valve open in the time order of 100 s. As a result, the gas expands with a supersonic velocity and is injected into the plasma gun via the nozzles on the inner electrode of the plasma gun. After the injection of the gas, the ion source plasma is produced by discharging the capacitor bank of the plasma gun with the optimal delay time of τ_{PG} around 270-310 s, since it takes about a hundred s to open the valve and several tens s for N_2 gas to reach the gas nozzle on the inner electrode of the plasma gun. Capacitor banks of 5 F and 1.5 F are used for the driver coil of the gas pu and the plasma gun, respectively. Each capacitor bank is usually charged up to 6.5 kV and 20 kV, respectively.

The ion current density of the source plasma produced by the plasma gun was evaluated by a biased ion collector (BIC) placed at 130 mm downstream from the top of the plasma gun where the anode is placed in the acceleration experiment. The collector of BIC was biased at a voltage of -200 V to remove accompanying electrons. Figure 5(a) shows the waveforms of the discharge current of the plasma gun (I_{PG}) and the ion current density (J_{ip}) of the plasma gun at the condition of τ_{PG}=292 s. As seen in Fig. 5(a), the discharge current I_p has a sinusoidal waveform of peak current 6.5 kA and quarter cycle 2.6 s. The ion beam with a peak current density J_{ip}=20 A/cm^2 and a pulse duration of 2 s is observed at about $\tau_p = 7.5$ s after the rise of I_p. The result suggests that it takes 7.5 s after the rise of the discharge current of the plasma gun (I_{PG}) for the ion beam produced in the plasma gun to reach the acceleration gap. Figure 5(b) shows the dependence of J_{ip} on the delay time of the discharge current rise from the rise of the gas pu current (τ_{PG}). As seen in Fig. 5(b), J_{ip} rises at $\tau_{PG} \approx 270$ s and has a peak around 290 s, and after that decreased. The result suggests that it takes 270 s after the rise of the gas pu coil for the gas to reach the nozzles.

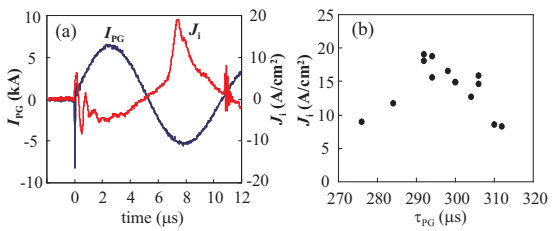

Figure 5 (a) Typical waveforms of I_{PG} and J_{ip} and (b) Dependence of J_i on τ_{PG}.

Figure 6 shows the experimental setup of the bipolar pulse generator, which consists of basically a Marx generator, a PFL, a transmission line (TL) and a dummy load ($CuSO_4$ water solution). The designed output of the bipolar pulse generator is the negative and positive pulses of voltage ± 200 kV with pulse duration of 70 ns each. The line consists of three coaxial cylinders with a rail gap switch on the end of the line, which is connected between the intermediate and outer conductors. The PFL is lled with the deionized water as a dielectric and charged positively by the low inductance Marx generator with maximum output voltage of 300 kV through the intermediate conductor. The waveform of the bipolar pulse is very sensitive to the performance of the rail gap switch, that is, the rise time and the time to reverse the polarity are dependent on the system's inductance including the inductance of the output switch. In order to realize the bipolar pulse with the fast rising and reversing time, the multichannel rail gap switch is used as the output switch of low inductance. The rail gap switch is lled with pure SF_6 gas and the pressure can be adjusted to control the optimum trigger timing for each experimental condition.

The bipolar pulse voltage (V_0) and charging

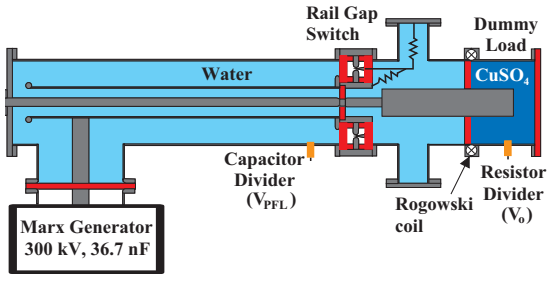

Figure 6 Cross-sectional view of bipolar pulse generator.

voltage of the PFL ($V_{\rm PFL}$) are measured by the resistive voltage divider and capacitive voltage divider placed near the rail gap switch, respectively. The values of $V_{\rm PFL}$ and V_0 are calculated by the ratio factor of the two voltage dividers (K=48500 and 1840, respectively). The Rogowski coil with the coe cient of 7 kA/V is used for the measurement of the bipolar pulse current

Figure 7 shows the typical waveforms of the charging voltage of the PFL ($V_{\rm PFL}$) and bipolar pulse output (V_0) at the charging voltage of 40 kV for the Marx generator. Here the lling pressure of the rail gap switch is 4.0 atm and the impedance of the dummy load is set at Z_L=7.5 Ω, which is almost same as the characteristic impedance of the line between the inner and intermediate conductors. As seen in Fig. 7, when the charging voltage of the PFL reaches the peak of 280 kV, the rail gap switch is self-broken at $t \approx 225$ ns and the square bipolar pulse, which consists of the rst pulse with a voltage of -138 kV and a pulse duration of 72 ns (FWHM) and the second pulse with a voltage of +130 kV and a pulse duration of 70 ns (FWHM), is successfully obtained. The peak voltage of the rst pulse is almost equal to the half of the maximum charging voltage of the PFL. In contrast the voltage of the second pulse is smaller. The reduction of the voltage in the second pulse seems to be due to the resistance of the rail gap switch.

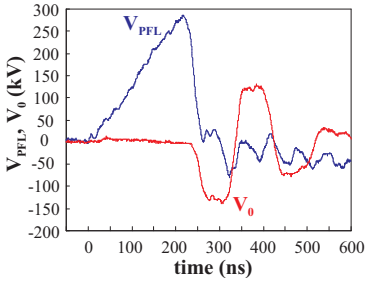

Figure 7 Typical waveforms of $V_{\rm PFL}$ and V_0.

4 Experimental Results

In order to con rm the principle of the BPA, the bipolar pulse was applied to the drift tube. First, BIC was installed inside the drift tube to observe the ion beam accelerated in the 1st gap by the rst pulse of the bipolar pulse, as seen in Fig. 4 The bipolar pulse generator was operated at 80 % of the full charge condition of the Marx generator. The plasma gun was operated at the condition of $\tau_{\rm PG} \approx 290$ s and the PFL was red at 5-10 s after the rise of the $I_{\rm PG}$. Figure 8(a) shows the typical waveforms of the output voltage (V_0), the output current (I_0) and the ion current density ($J_{\rm i}$) accelerated in the 1st gap, where $J_{\rm i}$ was measured at 50 mm downstream from the anode surface. As seen in the Fig. 8(a), the rst pulse of V_0 reaches the peak of 130 kV in 40 ns and the pulse duration is ≈ 65 ns. I_0 rises in 25 ns after V_0 is initiated, and reaches its peak of 9.5 kA within about 65 ns, whereas the ion beam with a current density of $J_{\rm i}$ = 40 A/cm^2 and a pulse duration of 30 ns(FWHM) is obtained at 45 ns after the peak of the rst voltage pulse. Considering the time of ight delay, the peak current density of 40 A/cm^2 corresponds to nitrogen ion (N^+, N^{2+}) and the ion beam corresponding the peak of $J_{\rm i}$ seems to be accelerated around the peak of the rst pulse.

Next, BIC was placed at 25 mm downstream from the grounded cathode to measure the ion beam accelerated by the bipolar pulse. The experimental result is shown in Fig. 8(b). The peak value of the second pulse is 90 kV with a pulse width of about 60 ns, and the current I_0 rises about 35 ns after the second voltage pulse starts, to a maximum value of 3 kA. It can be seen from Fig. 8(b) that the ion beam with a current density of $J_{\rm i} \approx 2$ A/cm^2 and a pulse duration of 30 ns is obtained at about 12 ns after the peak of the

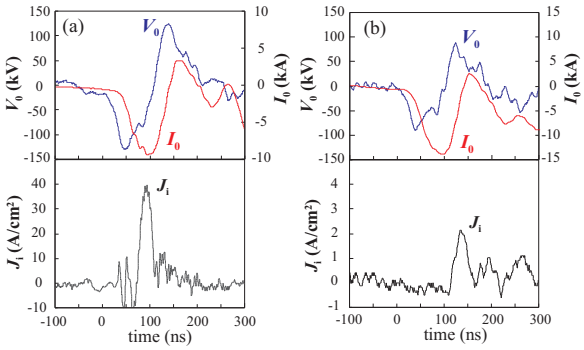

Figure 8 Typical waveforms of output voltage (V_0), output current (I_0) and current density ($J_{\rm i}$) observed in (a) 1-stage acceleration and (b) 2-stage acceleration.

2nd pulse voltage. In the system, the length of the drift tube is designed to be same as the beam length of N^+ beam of duration 70 ns at acceleration voltage 200 kV. On the other hand, in the experiments the peak value of the accelerating pulse is ≈ 90 kV as seen in Fig. 8(b). When the polarity of the bipolar pulse is reversed, singly ionized nitrogen ions do not reach the 2nd gap. Thus, N^+ are not accelerated by the 2nd pulse of the bipolar pulse. Considering the time of ight delay, doubly ionized nitrogen ions and/or charge-exchange singly ionized nitrogen ions seem to be again accelerated in the 2nd gap.

5 Summary

We have developed a bipolar pulse generator and a prototype of the accelerator to perform proof of principle experiments on the BPA. The bipolar pulse with fast rise time and sharp reversing time was con rmed experimentally. When the bipolar pulse was applied to the drift tube, the ions were successfully accelerated in each 1st and 2nd acceleration gap by the bipolar pulse. To con rm the principle of the BPA, we are planning to evaluate the ion species and the energy spectrum of the ion beam in detail.

Acknowledgement

This work was supported in part by the Grant-in-Aid for Scienti c Research from the Ministry of Education, Science, Sports and Culture, Japan.

References

[1] S. Humphries, Jr, Nucl. Fusion, **20**, pp.1549-1612, (1980).

[2] J. P. VanDevender and D.L. Cook, Science, **232**, pp.831-836, (1986).

[3] K. Yatsui *et al.*, Phys. Plasma, **1**, pp.1730-1737, (1994).

[4] D. J. Rej *et al.*, J. Vac. Sci. Technol. **15**, pp.1089-1097, (1997).

[5] H. Akamatsu, T. Ikeda, K. Azuma, E. Fujiwara and M. Yatsuzuka, Suf. Coat. Technol. **136**, p.269 (2001).

[6] Y. Hashimoto, M. Sato, M. Yatsuzuka, and S. Nobuhara, Jpn. J. Appl. Phys. **31**, 1922 (1992).

[7] D. J. Rej, R. R. Bartsch, H. A. Davis, R. J. Faehl, J. B. Greenly, and W. J. Waganaar, Rev. Sci. Instrum. **64**, 2753 (1993).

[8] X. P. Zhu, M. K. Lei, and T. C. Ma, Rev. Sci. Instrum. **73**, 1728 (2002).

[9] H. Ito, H. Miyake and K. Masugata, Rev. Sci. Instrum. **79**, 103502 (2008).

[10] K. Masugata, Y. Shimizu, Y. Fujioka, I. Kitamura, H. Tanoue and K. Arai, Nucl. Instrum. & Methods in Phys. Res. A **535**, 614 (2004).

[11] H. Ito, K. Igawa, I. Kitamura and K. Masugata, Rev. Sci. Instrum. **78**, 013502 (2007).